Spinel Oxide Hybrid Structures: Designing Battery-like Materials for High-Performance Energy Storage

by

Ali Rashti

A dissertation submitted to the Graduate Faculty of
Auburn University
in partial fulfillment of the
requirements for the degree of
Doctor of Philosophy

Auburn, Alabama
May 1, 2021

Keywords: Energy storage, electrochemistry, metal oxide hybrid structures, battery-like material

Approved by:

Dr. Tae-Sik Oh, Chair, Assistant professor, Department of Chemical Engineering
Dr. Xinyu Zhang, Associate professor, Department of Chemical Engineering
Dr. Andrew Adamczyk, Assistant professor, Department of Chemical Engineering
Dr. Majid Beidaghi, Assistant professor, Department of Mechanical Engineering
Dr. Dong-Joo Kim, Alumni Professor, Department of Mechanical Engineering

Abstract

The electrochemical capacitors, also known as supercapacitors, are the next-generation energy storage devices that can store the energy by a surface or near-surface redox reaction that enables achieving high energy density at high charge-discharge rates. Since the discovery of the "pseudocapacitive" behavior of hydrous RuO_2 by Conway, there has been growing research on pseudocapacitance in other materials including metal oxides. Spinel oxides are a subcategory of transition metal oxides (TMOs) that exhibit high redox activity, however, they exhibit the electrochemical characteristics of battery-like material that does not meet the criteria for high-performance energy storage, which are potential independent charge storage and limited rate-capability. It has been suggested that the electrochemical behavior of spinel oxides, for this thesis in particular $NiCo_2O_4$, could be shifted from battery-like to pseudocapacitive by employing appropriate methods to produce nanomaterials with high surface areas and using high surface conductive structures such as graphene, CNTs, and polymers to form hybrid structures with enhanced electrochemical properties.

Through my Ph.D. work, we have tried to focus on addressing solutions to charge-transport limitations and sluggish kinetics, as two key factors that hinder the practical application of spinel oxides for high-performance energy storage devices. We have developed a universal fabrication technique for hybrid structure formation as well as a novel approach to tune the spinel oxides microstructure by controlled crystallization of sacrificial templates to tackle the above-mentioned obstacles and provide perspective and possible opportunities for spinel oxide hybrid structures for practical applications in energy storage.

Dedications

To my mother Maryam and my father Khosro

For their unconditional love and support

No matter how far, you're always in my heart

Nothing was harder than not being able to see you during these years

To Elnaz

For trying to be supportive, being there for mom and dad when I was gone all these years

To Bani

Tu as fait de moi une meilleure personne avec m'aimer pour qui je suis

Acknowledgment

My Ph.D. journey would not be possible without the help and support of many individuals throughout the past five years for which I would like to express my dearest gratitude.

First, I would like to thank my Ph.D. advisor Dr. Tae-Sik Oh for his support, guidance, and for letting me follow my curiosity and find my interests in the electrochemistry field. Thank you for your patience and for making me feel like a part of a team that I will always have good memories of. I am also grateful and lucky to have the support and guidance of Dr. Eden. It would not be possible to finish this journey without his continuous care for graduate students.

I would also like to express my gratitude to Ehsan, Farshad, and Simon, my research group members, for always assisting me whenever it was needed. I also appreciate the help of my colleagues and collaborators, Dr. Jorge Moncada, Dr. Armin Vahidmohammadi, Nima Alizadeh, Marjan Azadi, Dr. Rohit Kanungo, Mingyang Chi, and Dr. Buhua Wang for their help during these years.

I would also express my appreciation to the committee members Dr. Xinyu Zhang, Dr. Andrew Adamczyk, and Dr. Majid Beidaghi for their time to review this work and their insightful comments. I would also thank Elaine and Brian who were always there when help was needed.

Last, I would like to express my most sincere gratitude to my family and friends, whose steady support made this journey joyful and Auburn will forever be my second home.

Table of Contents:

List of Figures

List of Tables

List of Abbreviations

2D	2-dimensional
3D	Three-dimensional
EES	Electrochemical Energy Storage
EC	Electrochemical Capacitors
EDLC	Electric-Double Layer Capacitor
UPD	Under-Potential Deposition
LDH	Layered double hydroxides
TMOs	Transition metal oxides
TMDs	Transition metal dichalcogenides
CNTs	Carbon nanotubes
GO	Graphene oxide
rGO	Reduced graphene oxide
CTAB	Cetrimonium bromide
APTES	(3-Aminopropyl)triethoxysilane
PANI	Polyaniline
PPy	Polypyrrole

EPD	Electrophoretic Deposition
DLS	Dynamic Light Scaterring
ζ	Zeta Potential
CV	Cyclic voltammetry
EIS	Electrochemical impedance spectroscopy
GCD	Galvanostatic charge-discharge
XRD	X-ray diffraction
XPS	X-ray photoelectron spectroscopy
FTIR	Fourier-transform infrared spectroscopy
AFM	Atomic Force Microscope
TEM	Transmission Electron Microscopy
HRTEM	High-Resolution TEM
STEM	Scanning Transmission Electron Microscopy
EDS	Energy Dispersive X-ray Spectroscopy

Chapter 1: Electrochemical Energy Storage Principals

1.1 Introduction:

Environmental concerns, as well as technological advances, have brought attention to develop renewable and sustainable energy sources as today's main energy resources are nonrenewable and suffer from the complexity of distribution systems. Yet, one of the biggest concerns regarding renewable energy sources is their non-continues power generation. Therefore, developing advanced devices with the ability to deliver energy on demand is a growing field.[1,2] Energy storage systems are mainly classified into mechanical, chemical, electrical, and electrochemical. The goal is to develop energy storage systems with high energy density, high power density, long life, low cost, and being environmentally friendly. Electrochemical energy storage (EES) systems have shown to be very promising to be used as energy delivery systems for portable electronic devices and electric vehicles. It has been anticipated that with vast technological advancements in EES technologies, the industry's revenue will grow from $1.5 billion in 2010 to $25.3 billion within the next decade.[3]

Batteries and electrochemical capacitors (ECs) are the two most widely used EES systems while batteries provide a high-energy density but suffer from low power density while ECs show low energy density but provide high power density. Ragone plot in Figure 1.1 demonstrates a comparison between the power and energy relationship of different EES systems. Although the EES technologies show a promising potential for different applications, their performance still needs fundamental improvements due to the harsh requirements of the industry. There have been numerous research efforts to identify desirable electrode materials that would satisfy the

requirements of high energy and high power densities as well as durability and long cycle life.[4] The research in the battery field is more mature and ECs have attracted more attention recently. Introducing new materials reduce the gap in electrochemical characteristics of ECs and batteries, combining the high energy density of batteries with the high-power density of ECs. Detailed comparison of EES devices with appropriate measurements and analyses would clarify the line separating battery type or pseudocapacitive materials to distinguish and classify them. The preliminary study and research proposed here will be discussing developing the design and fabrication of spinel metal oxide hybrid electrodes and study their electrochemical behavior with a focus on enhancing their performance as electrochemical supercapacitors by either exploiting new techniques for hybrid materials assembly or complex metal oxide structures.[5]

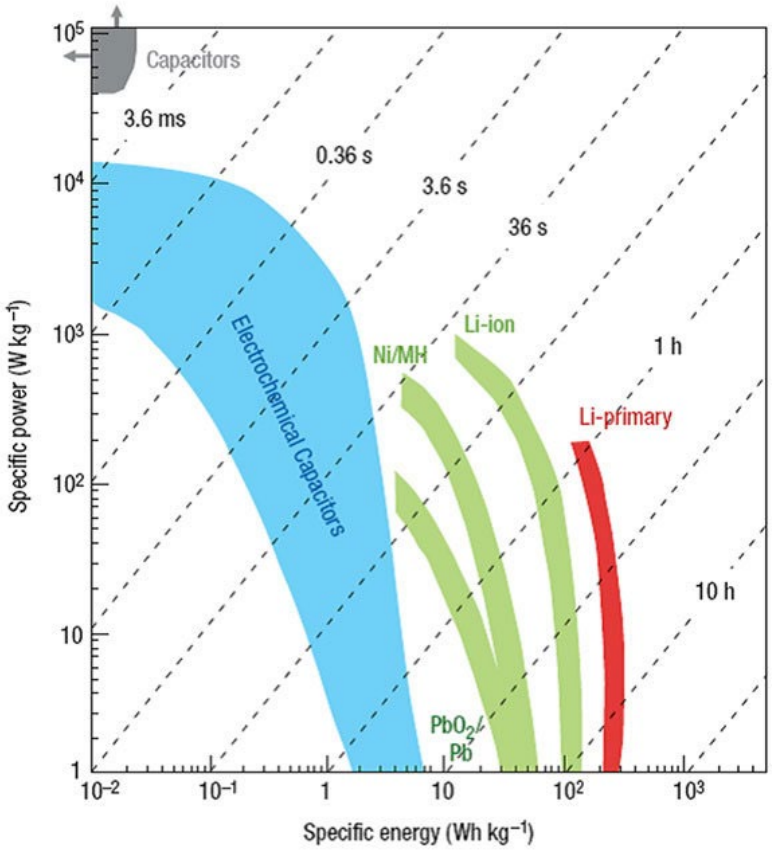

Figure 1.1. Ragone plot comparing the power-energy characteristics and charge/discharge times of different energy storage devices [6]

1.2 Principle of energy storage in ECs:

EC devices have gained a lot of interest in the past years due to their rapid charge-discharge rate and long cycle life compared to other energy storage devices. ECs have diverse applications in different fields like power capture, supply, and backup power. ECs are generally divided into EDLCs and pseudocapacitors categories based on their energy storage mechanism. In EDLCs, the energy storage is via electrostatic accumulation of charge on the electrode-electrolyte interface.[7] On the other hand, for pseudocapacitors, reversible redox reactions at the surface of an electroactive material or near its surface are the main energy storage

mechanism. In practice, both mechanisms could be employed in a supercapacitor device.

The energy storage mechanism in EDLCs involves absorption of charge at the surface of the electrodes.[8] The adsorption of electrolyte ions onto the electrified material and charge arrangement in the Helmholtz double-layer during charging/discharging of the electrodes results in a displacement current in the system. The fast nature of these physical phenomena provides rapid energy delivery and provides high power density as is indicated in the Ragone plot. While EDLCs rapid energy delivery is ideal, because of their limitation of the electrode surface, the energy density of these types of capacitors is much lower comparing to other energy storage devices. The EDL capacitor could be described using the following equation: [9]

$$C_{dl} = \frac{Q}{V} = \frac{\varepsilon_\tau \varepsilon_0 A}{d} \quad (1)$$

Where C_{dl} is the capacitance of one electrode, Q is the total charge transfer at potential V, ε_τ and ε_0 are respectively the dielectric constants of the electrolyte and vacuum, d is the distance of charge separation and A indicates the surface area of the electrode. By assuming constant C_{dl} for EDLCs, the response current flow of the electrode could be calculated using equation (2):

$$I = \frac{dQ}{dt} = C_{dl} \frac{dV}{dt} \quad (2)$$

Where t stands for the charging time. Using a linear sweep rate for potential, the potential could be formulated as $V = V_0 + vt$ (V_0 stands for initial potential and v is the sweep rate), then the relationship could be described as:

$$I = C_{dl} v \quad (3)$$

Equation (3) shows that current, I, changes linearly with the sweep rate. This equation

could be plotted as a current (I)-voltage (V) plot or a cyclic voltammogram (CV). An ideal EDLC capacitor presents a rectangular shape cyclic voltammogram, which would expand by increasing the scan rate as is illustrated in Figure 1.2b. Alternatively, charging and discharging the capacitors by exploiting a constant current would result in a potential increase or decrease with a constant rate. An ideal EDLC capacitor shows a triangular shape charge/discharge diagram as is shown in figure 2.1c.

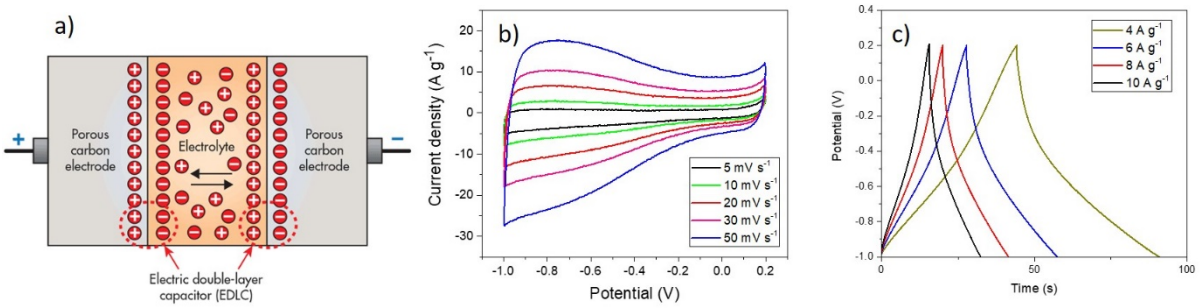

Figure 1.2. a) Schematic diagram showing the energy storage mechanism in double-layer capacitors b) CV and c) galvanostatic charge/discharge responses of carbon-based double-layer capacitors

The performance of pseudocapacitors is usually determined by the maximum energy ($E_{max} = 1/2(CV^2)$) and maximum power ($p = V^2/4 * R$) that can be generated by them. Voltage window (V), capacitance (C), and Resistance (R) are the variables that affect the performance of the capacitors. Voltage window is mainly limited by the electrolyte voltage stability window, corrosion of the current collectors, and oxidation of electrode materials. Capacitance depends on the electrode materials and electrode/electrolyte interface and the resistance which is usually known as equivalent series resistance (ESR) in electrical energy storage devices and consists of the electrolyte resistance and electrode/current collector interfacial resistance. The rational

design of an ideal capacitor would be to maximize the potential window and capacitance while lowering the series resistance.

Carbon-based materials such as carbon nanotubes (CNTs). Graphene and activated carbons have been introduced as promising materials for EDLCs.[10–12] Parameters such as surface area, pore structure, and pore size distribution, and the number of carbon layers are variables that play a role in their performance.[13,14]

1.3 Pseudocapacitive storage:

Pseudocapacitance charge storage arises from a faradic charge-transfer reaction happening on the surface or near the surface of the electrode. The state of charge (q) is a function of potential with the extent of faradic charge/discharge (Q) passed.[8] Here, pseudocapacitance ($C_{\emptyset}$) could be attributed to the change of in Q with the potential or, $^{dQ}/_{dV}$. Pseudocapacitance is faradic in nature and unlike electric double layer capacitance; it is not a function of potential-dependent charge accumulation. Pseudocapacitance is also battery behavior are also different in the ideal Nernstian process that is involved in a battery, in which the faradic reaction occurs at a constant potential range.

Pseudocapacitance could be categorized into three types, which are underpotential deposition, surface redox pseudocapacitance, and intercalation pseudocapacitance. Figure 1.3 shows schematic diagrams of different pseudocapacitive processes.

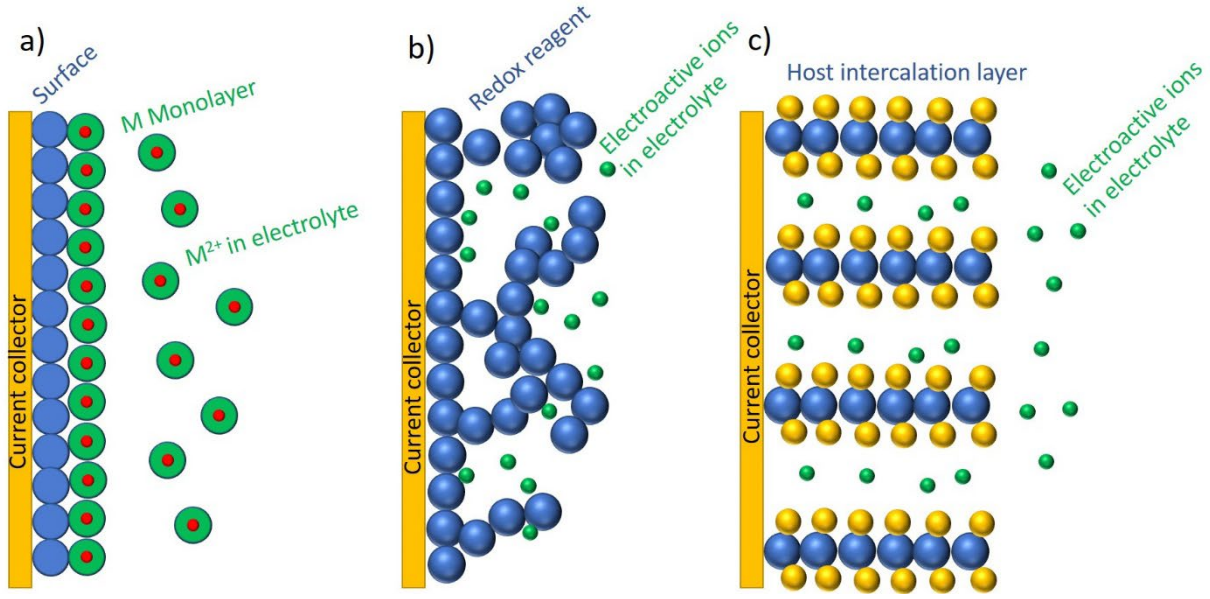

Figure 1.3. Schematic diagrams of pseudocapacitance processes a) UPD, b) Pseudocapacitance and c) Intercalation

In a few words, underpotential deposition (UPD) is the electrodeposition of a cation onto another metal in a potential less negative than their Nernst equilibrium potential. This phenomenon happens especially when there the Surface-metal interaction is favored than metal-metal interaction in the crystalline structure of the pure metal. UPD happens for both metal deposition or gas adsorbed layers.[15]

Surface redox pseudocapacitance is the common type of pseudocapacitance being studied. The first step in the mechanism involves the adsorption of electroactive ions onto the surface which is followed by a faradic reaction with the surface-active materials resulting in a charge transfer. Transition metal oxides, conductive polymers, and transition metal carbides. For transition metal oxides, pseudocapacitance comes from a fast-redox reaction due to the intercalation of protons (H^+), or alkali metal cations as it is illustrated below:

$$MO_2 + H^+ + e^- \leftrightarrow MOOH \quad (4)$$

Or

$$MO_2 + C^+ + e^- \leftrightarrow MOOC \quad (5)$$

During these redox reactions, a molecular layer forms on the surface of the electrode. No phase transformation happens and the potential of the electrode changes linearly with the total charge and it is proportional to the area of the electrode. Electrically conductive polymers (ECPs) show redox pseudocapacitance through electrochemical doping-undoping as described below:

$$[ECP] + nX^- \leftrightarrow [(ECP)^{n+}nX^-] + ne^- \quad (6)$$

In which, X^- is an anionic species from the electrolyte which is inserted into the electron backbone during oxidation and is released upon reduction.

Another faradic energy storage process, which is more recent, comparing the other two, is a faradic process that, unlike battery-like materials, the electrode materials do not undergo any crystallographic phase change during the charge transfer process. Intercalation of Li^+ ions into TiS_2 [16], MOS_2 [17], and V_6O_{13} [18]or the intercalation of H^+ into Pd and Pd-Ag alloys[16] are among this type of faradic energy storage process. Transition metal carbides (MXenes) are newly discovered 2D materials with the general chemical formula of $M_{n+1}X_nT_n$ in which M stands for a transition metal, X is either carbon or nitrogen atom and T is a functional group with great potential to be used as intercalation pseudocapacitors.[19] $Ti_3C_2T_n$ is a well-known Mxene material in which changing the oxidation states of Ti during intercalation/de-intercalation results in a high volumetric capacitance as it is shown in eq. (7):

$$Ti_3C_2O_x(OH)_yF_{2-x-y} + \delta e^- + \delta H^+ \leftrightarrow Ti_3C_2O_{x-\delta}(OH)_{y+\delta}F_{2-x-y} \quad (7)$$

Although they are different faradic processes involved in pseudocapacitors, all the pseudocapacitance mechanisms follow similar thermodynamic principles. A logarithmic equation defines the relationship between the potential and extent of the charge storage process:

$$E = E^0 + \frac{RT}{nF}\ln\frac{X}{1-x} \quad (8)$$

As E is the potential of the electrode, R is the ideal gas constant, T is the temperature, n is the number of electrons involved in the reaction, F is the Faraday constant and X indicates the fraction of active sites occupied.[9]

By assuming the adsorption of the electroactive ions as a Langmuir system as shown in eq. (9):

$$\frac{X}{1-X} = k.\exp\left(\frac{VF}{RT}\right) \quad (9)$$

Then the pseudocapacitance could be defined as:

$$C_{\emptyset} = q^*.\frac{dX}{dV} \quad (10)$$

Using equations (9) and (10), it could be deducted that $C_{\emptyset}$ changes with regards to X and reaches a maximum at X=0.5. For pseudocapacitors, the electrode potential is a function of the occupancy fraction of the active sites ($\Delta G = \Delta G^{\theta} + RT\ln\left(\frac{X}{1-X}\right)$) while for the batteries, the potential is usually calculated using the Gibbs free energy for pure 3D phases of the structures and the concentration of the electrolytes. ($\Delta G = -nFE^{\theta}$).[9,20]

1.4 Kinetic electrochemical features of pseudocapacitors:

To understand the charge storage mechanism, different characterization methods are used. Generally, two types of characterization must be conducted to confirm the charge storage mechanism and study the kinetics of the phenomena. Structural characterization to determine

materials structural properties and changes and electrochemical characterization to study the kinetics and performance of the electrode materials. Structural characterization methods such as Brunauer–Emmett–Teller (BET) method[21], FTIR, Raman spectroscopy, in situ XPS[22], in situ NMR[23], and in situ XRD[24] are usually conducted. As for the electrochemical characterization, cyclic voltammetry, galvanostatic charge-discharge, and electrochemical impedance spectroscopy are the main tests that are performed to study the electrochemical behavior of the system.

Cyclic voltammetry is a very informative method to study the behavior of capacitive systems. An ideal capacitive system shows a rectangular shape diagram with no potential shift between anodic and cathodic peaks at different potential scan rates. All of the ECs (except air and vacuum dielectric capacitors) suffer from an effective equivalent resistant series (ESR), causing polarization effect and limiting kinetic limitations. One of the main features of pseudocapacitors is redox reversibility[8]. If the surface redox reaction is changed by an increasing potential sweep rate, v, the kinetic reversibility is gradually lost. This is usually studied by peak potential, E_p that remains independent of scan rate up to a critical sweep rate, v_0. After reaching this critical point, the peak potential increases with log v as well as the difference between the cathodic and anodic peak voltage ($\Delta E_{a,c}$)[25]. The kinetic studies using v_0 determination determines the charge/discharge rates for ECs performance. Hydrous RuO_2[26], MnO_2[27], Polyaniline[28], and $Ti_3C_2T_x$ [29] are some of the materials showing pseudocapacitive properties.

The CV diagrams of electroactive materials demonstrate that pseudocapacitors and EDLs show similar electrochemical behavior, which makes it hard to differentiate these two mechanisms. Bruce Dunn and co-workers developed a method based on which it is possible to estimate the contribution of EDL mechanism and pseudocapacitance mechanism through experimental design using cyclic voltammetry as a convenient and yet delicate method.[30]

An empirical method is used to describe the total current measured under a potential sweep rate as the sum of the diffusion-controlled process (i_{diff}) and required current to charge the double layer at the interface or surface-controlled fast faradic reaction (i_{cap}):

$$i(v) = i_{cap} + i_{diff} = av^b \quad (11)$$

$$\log(i(v)) = \log a + b\log v \quad (12)$$

b value could be calculated using the slope of the linear plot of equation (12), it is possible to provide information about the kinetics of the reaction. Two general values are usually considered for b, which are b=0.5 and b=1. A value of 1 for b implies that the charge storage comes majorly from the fast near-surface process while b=0.5 indicates the slow semi-finite diffusion-controlled faradaic process. From this, b value ranging between 0.5 to 1 indicates a transitional area that both processes contribute to charge storage and as we go from 0.5 to 1, near-surface activities have a greater contribution than diffusion controlled processes[30,31]. Figure 1.4 shows a schematic description of how the b value defines the general behavior of an electroactive material.[32]

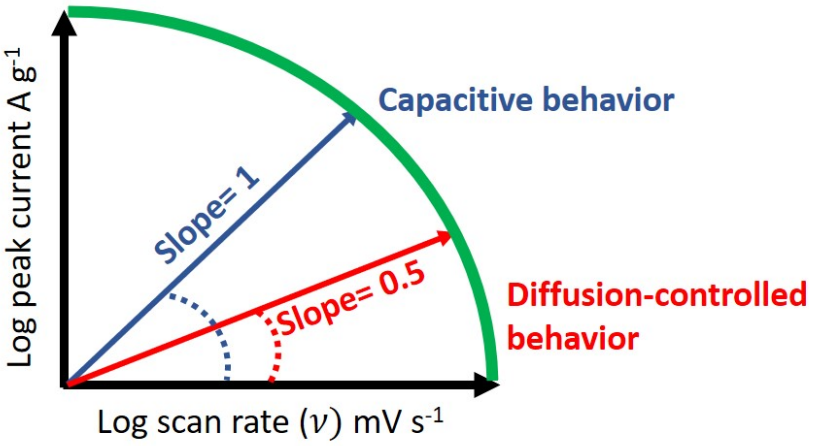

Figure 1.4. The dependence of peak current for electroactive materials from battery-type materials (b=0.5) to capacitive material (b=1)

The b value provides helpful data for designing electrode materials like distinguishing battery type behavior from pseudocapacitive behavior and providing information about charge storage mechanisms at different potential/scan rates.

To quantify the capacitive properties and calculate the relative contribution of capacitive and diffusion-controlled energy storage processes, two methods are usually used. In the first method, by considering the fact that surface-dominant processes change linearly with v and diffusion-controlled processes vary linearly with $v^{1/2}$, so the total current could be expressed as the sum of both processes: [33,34]

$$i(v) = i_{cap} + i_{diff} = k_1 v + k_2 v^{1/2} \quad (13)$$

Which can be reformulated as

$$i(v)/v^{1/2} = k_1 v^{1/2} + k_2 \quad (14)$$

As it is shown in eq.14, by plotting i (v)/$v^{1/2}$ against $v^{1/2}$, it is possible to determine the capacitive charge storage contribution (k_1 v) and diffusion-controlled processes contribution (k_2 v) using the slope and intercept of the diagram.

The other method, which is introduced by Ardizzone et al.,[35] tries to relate total stored charge and sweep rate. As it is shown in eq.15, the total charge q^* is the sum of capacitive charge, q_s^* ($\propto$v) and diffusion-controlled charge, q_d^* ($\propto v^{1/2}$):

$$q^*(v) = q_s^* + q_d^* \quad (15)$$

q_s^* represents the charge for surface dominant processes, so by increasing the potential scan rate to infinite values ($v \rightarrow \infty$) then:

$$q^* \rightarrow q_s^* \ (16)$$

Moreover, the maximum charge will be gained when the scan rate reaches 0, so when $v \rightarrow 0$ then:

$$q^* \rightarrow q_m^* \ (17)$$

q^* is estimated to be limited by $v^{-1/2}$ if we assume it is limited by semi-infinite diffusion[35], hence, the capacitive contribution is not a function of v and the total charge could be 3formulated as:

$$q^*(v) = q_{v\rightarrow\infty}^* + q_d^* = q_{v\rightarrow\infty}^* + \alpha(v^{-\frac{1}{2}}) \ (18)$$

Where α is a constant value. The minimum value for the total charge could be determined by extrapolating data for the intercept point from the linear plot of $q^*(v)$ vs $v^{-1/2}$. Eq. 17 could be reformulated if we rewrite it as a function of $v^{1/2}$, then we will have:

$$1/_{q^*(v)} = 1/_{q_m^*} + \beta(v^{\frac{1}{2}}) \ (19)$$

From which, it is possible to extrapolate the maximum value of the total charge for $1/q^*(v)$ vs $v^{1/2}$ by extrapolating the data for $v^{1/2} = 0$ at the intercept.

The difference between total charge, q_m^* , and the surface charge, $q_{v\to\infty}^*$,is the diffusion-controlled charge.

$$q_d^* = q_m^* - q_{v\to\infty}^* \quad (20)$$

Based on this procedure, capacitive contribution and diffusion contribution could be calculated for each potential. These methods have been discussed in different literature[36,37] for calculating the contributions of capacitive effect and diffusion process.

Another electrochemical technique to characterize the electrochemical features of pseudocapacitors is exposing the electrodes to a constant current for charge and then for discharge. This process is known as 'Galvanostatic Voltammetry' or 'Galvanostatic Charge-Discharge'. During the process, when a constant current is applied to the system, the concentration of electroactive ions near the electrode surface starts to decrease if we consider a simple electron transfer takes place on the surface of the electrode which could be described as $O + ne \rightarrow R$. Because of this depletion, the electroactive ions start to diffuse from the bulk phase of the solution and a concertation gradient starts to form from the surface of the electrode and grows out. The process continues until the concentration profile extends into the bulk phase of the solution as is shown in Figure 1.5.[9,38]

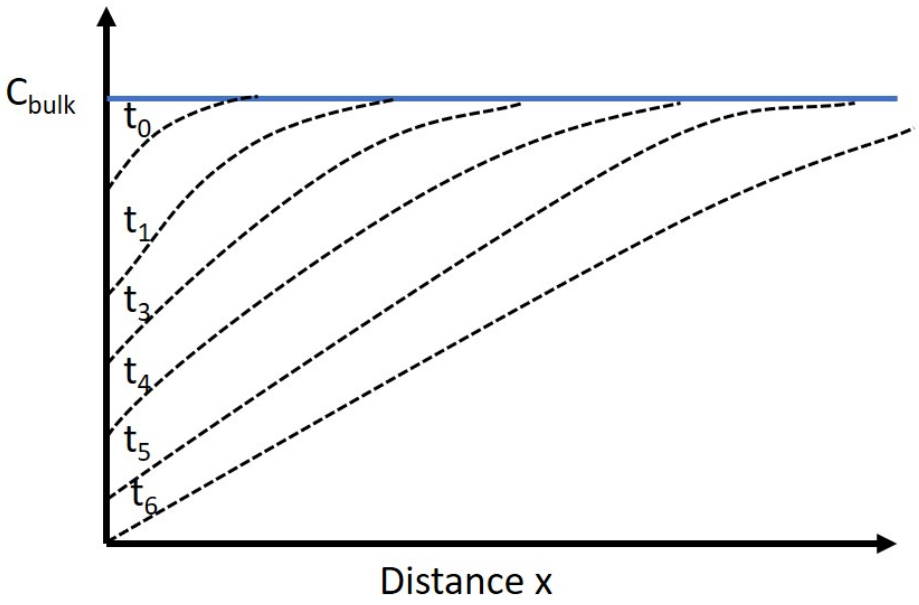

Figure 1.5. Concentration profile extending into the bulk phase of the solution as a function of time ($t_6 > t_0$)

The electroreduction of electroactive species continues until the concentration of the electroactive species on the surface of the electrode reaches zero, after reaching this point, the potential starts to change instantaneously. The period between initiation of electroreduction and the sudden change of potential is referred to as the 'transition time'.[9,38]

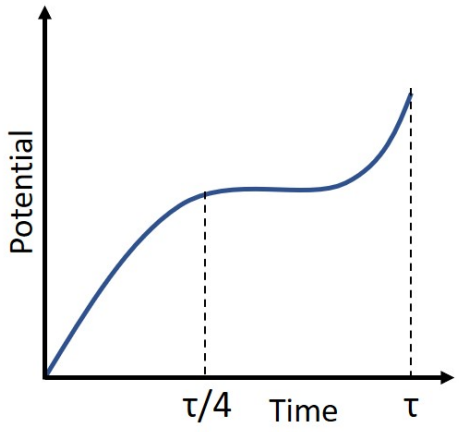

Figure 1.6. Potential change with respect to time in a galvanostatic voltammetry process

Galvanostatic voltammetry is an advantageous and common technique to characterize electrical energy storage systems since it shows different phenomena happening during the charge/discharge phenomena including the IR component, charging of the double layer, and the onset of the faradic process during the transition time.

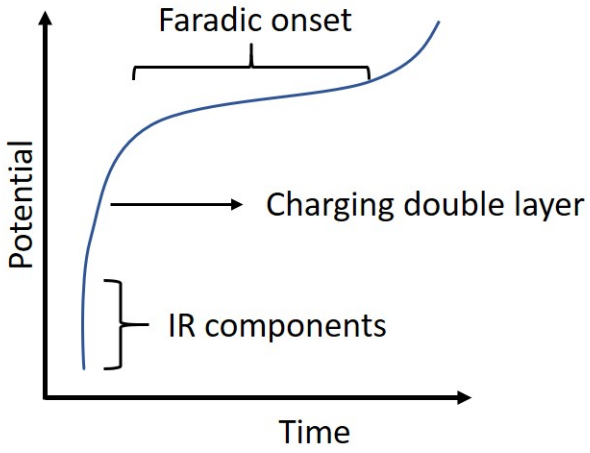

Figure 1.7. A schematic chronopotentiogram of a system with significant series resistance.

Galvanostatic discharge curve is commonly used to calculate the capacitance for capacitors using the calculations below:

$$C = {I}/{\frac{dV}{dt}}\ (A.s.V^{-1} \text{ or } F)\ (21)$$

$$\left(\frac{dV}{dt}\right) = \frac{V_{max} - 1/2V_{max}}{T_2 - T_1}\ (22)$$

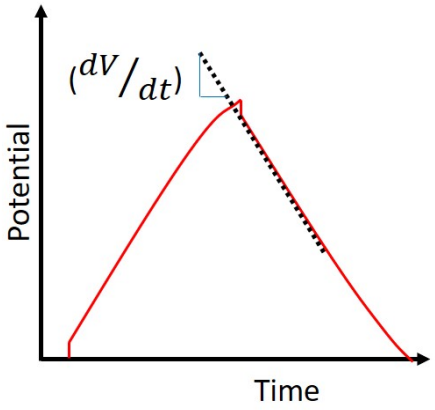

Figure 28. A GCD curve distortion due to Faradaic reactions and graphical illustration of calculating $(\frac{dV}{dt})$

The equivalent series resistances that shows the sum of internal resistances of a capacitor could also be calculated easily using the galvanostatic charge/discharge curves as is shown in Figure 1.9:

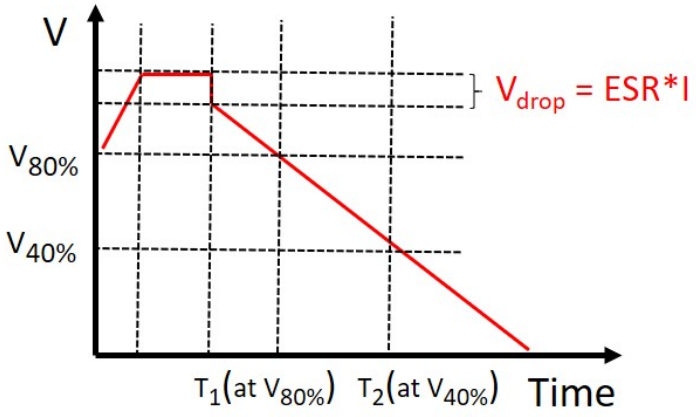

Figure 1.9. ESR in discharge curve and its mathematical calculation using V_{drop}

As it can be deduced from equation (23), to have a capacitor with the highest power, the ESR should be minimized:

$$P = \frac{V^2}{4*ESR} \quad (23)$$

During the galvanostatic charge/discharge process, pseudocapacitors show a small voltage plateau since they do not experience any phase transformation during the charge/discharge process and charge/discharge curves will be almost linear and comparable to EDLCs. In general, pseudocapacitors exhibit linear or near-linear charge/discharge curves with a semi-rectangular CV with redox peaks that are overlapped.

Besides, CV and galvanostatic charge/discharge, electrochemical impedance spectroscopy (EIS) is another method to discuss the pseudocapacitance phenomena. Using EIS, it is possible to model electrochemical cell series of passive electrical circuit elements, known as 'equivalent circuits'. This network usually consists of common electrical elements such as resistors, capacitors, and sometimes inductors. During EIS measurements, the potential or current is set to a V_s or I_s and a small sinusoidal signal is applied to the system from a high frequency to a low frequency and the response is measured for each frequency, and impedance is calculated. The interpretation of the EIS results highly depends on the equivalent circuit that fits the EIS spectra. The Nyquist representation for pseudocapacitors consists of three regions: ohmic resistance (R_Ω), which indicates the resistance of the entire cell including materials, interfaces, and electrolyte, a high-frequency region associated with the kinetic control and indicates charge transfer resistance (R_{CT}), which is usually present as a semi-circle, and a low-frequency region associated with the mass transfer control as it is shown in Figure 1.10.

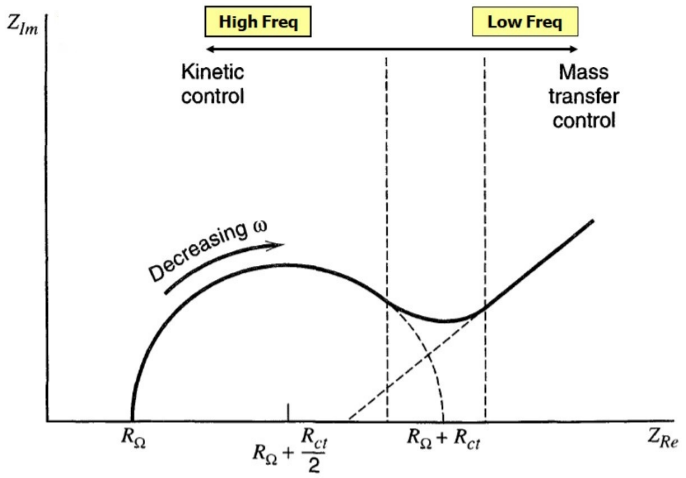

Figure 1.10. A typical Impedance (Nyquist) plot for an electrochemical system[38]

The impedance plot for an ideal capacitor indicates a 90° phase angle. Phase angles lower than 90° often indicates a pseudocapacitive behavior, which could be shown by a constant phase element in the equivalent circuit: [39]

$$Z = \frac{1}{B(i\omega)^p} \quad (24)$$

In equation (24), B is a constant, ω stands for frequency and p is an adjustable parameter ranging from 1 to 0.5. While p=1 corresponds to an ideal supercapacitor and p=0.5 shows a semi-infinite diffusion.

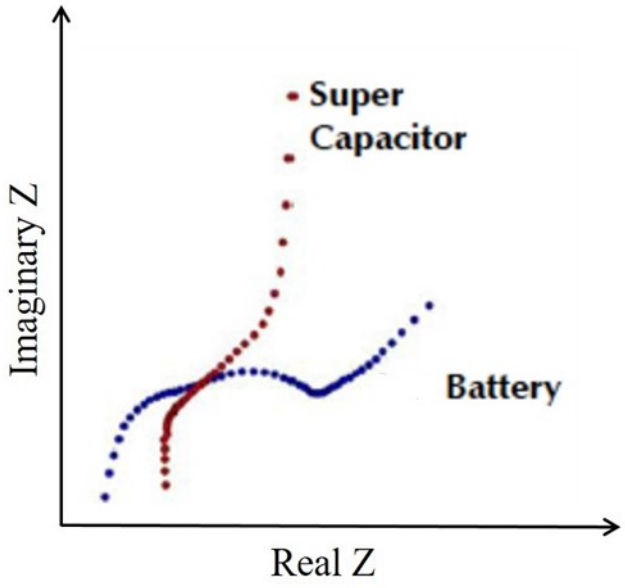

Figure 1.11. Impedance plot of a supercapacitor in comparison with a battery. The phase angle changes from an almost vertical line to an almost $\mathbf{45}^{\circ}$ phase angle (Source: ***https://www.gamry.com/application-notes/EIS/low-impedance-limits-with-the-gamry-reference-30k-booster/***)

Chapter 2: Materials for Energy Storage

2.1 Carbon materials:

Due to the unique features that carbon-based materials have, including their abundancy, good conductivity, chemical stability, and usual high surface area[40], they are considered promising electrode materials in EDLCs fabrication. Recently, different carbon nanostructures such as porous activated carbons (ACs) carbon nanotubes (CNTs), carbon nanofibers (CNFs), and graphene have been investigated as electrode materials for EDLCs. The recent developments in EDLCs fabrication are focusing on designing porous structure optimization, morphology control, and surface modification.

Porous activated carbon materials are the most common porous carbon structures with a very high surface area that show capacitance as high as 200 F g^{-1} and 100 F g^{-1} in aqueous electrolytes and organic electrolytes.[41] However, because of the wide pore size distribution of these materials, and the presence of micropores with a pore size of less than 0.5 nm. These micropores are too small to be accessible by electrolyte ions. There have been various efforts to tune the porosity of carbon porous structures. Ordered mesoporous carbons (OMCs) with a narrow distribution of pore size in mesoporous range (From 2 -50 nm), provide channels with enhanced transportation and accessibility of the electrolyte ions, especially in organic solvents[42]. Carbide-derived carbons (CDCs) have also been reported to show an unusual increase in capacitance when they have a microporous structure (< 1nm) suggesting a higher capacitance would be achieved from charge storage in pores smaller than electrolyte ions[13]. Based on these findings, Liu et al., [43] developed an ordered hierarchical mesoporous/microporous structure (OHMMC) that can deliver capacitance as high as 146 F g^{-1} in organic solvents.

Aside from ACs, graphene has also been utilized vastly as a building block for fabricating porous structures. Its outstanding physical properties such as high surface area (around 2600 $m^2 g^{-1}$), high electron mobility, and theoretical gravimetric capacitance of 550 F g^{-1}.[44,45] Graphene sheets suffer from sticking to each other due to van der Wall's attractions causing dramatic surface area loss, and hence lowering their capacitance properties.[46] This has led to multiple types of research regarding developing different graphene morphologies such as mesoporous graphene or 3-D architectures.[47,48]

As reported by Conway, carbons used in EDLCs must have a high surface area, good intraparticle and interparticle conductivity, and efficient accessibility of the ions to the intra-pore space of the structures.[9] A hierarchal porous structure is promising in the advanced performance of supercapacitors since it will provide a high surface area and therefore higher capacitance and power density, and at the same time, the interconnected micropores and macropores would improve the ion accessibility to the intra-pore space of the electrode, causing a high rate capability.

2.2 Pseudocapacitive materials:

The pseudocapacitance phenomena were discovered in 1971 for the first time when fast faradic charge-discharge was seen in RuO_2 for the first time[49]. Despite the charge storage mechanism was due to a redox process, the CV showed a rectangular shape which is a characteristic of capacitor behavior. Since then, other materials have been discovered to exhibit pseudocapacitive behavior. Ru-based materials, Mn-based materials, and Ni/Co-based materials are among the structures that have been studied for their pseudocapacitive behavior[41].

Pseudocapacitive electrodes are generally categorized as materials with intrinsic pseudocapacitive behavior and materials with extrinsic pseudocapacitive behavior. Intrinsic

pseudocapacitive materials show approximately linear charge/discharge curves without exhibiting a wide voltage plateau. They have high reversibility and their redox peaks potential difference is small. Besides, their EIS shows a vertical line with an angle close to 90°. These materials show pseudocapacitive behavior regardless of their morphology, particle size, and crystalline structure. MnO_2[50], RuO_2[51], Oxides with spinel structure[52], MXenes[29], and conducting polymers[53] are considered as this type of pseudocapacitors**.**

Extrinsic pseudocapacitive materials are traditionally used for battery design. These materials offer the possibility of tailoring the power density and energy density. Tuning the traditional battery-like materials on the nanoscale enables them to increase the power density because of short ion and electron paths. However, the traditional battery-type electrochemical response is very dependent on the morphology of the electroactive materials and hence the electrochemical energy storage mechanism. By decreasing the particle size of these materials from bulk to small nanoscale, the voltage plateau region in the charge/discharge region fades. $LiCoO_2$ is a famous example since it is a commercial cathode for Li-ion batteries. However, as is shown in Figure 2.1 as the crystalline size of the electroactive materials decreases, the discharge plateau is gradually decreased showing a capacitor behavior. Lithium/Sodium metal oxide-based materials such as Li_xTiO_2[13] exhibit such behavior as well. V_2O_5[54] and CeO_2[55] have also been reported to show pseudocapacitive behavior.

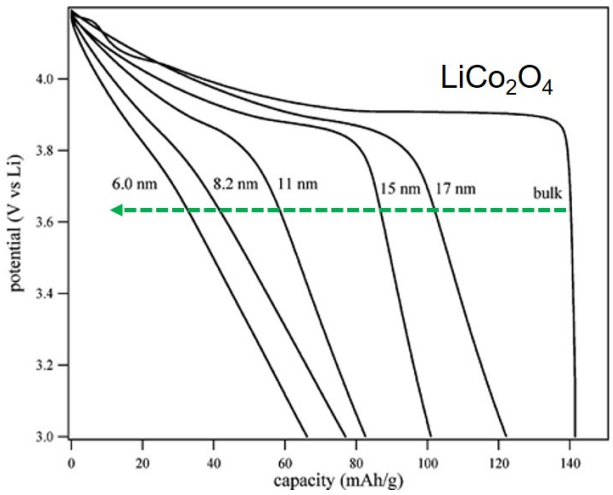

Figure 2.1. Size-dependent charge storage behavior of $LiCo_2O_4$ showing an extrinsic pseudocapacitance behavior[56]

2.2.1 Oxides with spinel structure as pseudocapacitive electrodes:

Hydrous RuO_2 was the first material discovered showing pseudocapacitance behavior, but Ruthenium is a high price, a rare element that prevents its large-scale application. Since then, there have been several studies on other metal oxide structures and compositions to look for prospective candidates with suitable characteristics for industrial-scale applications. Transition metal oxides (TMOs) are promising materials in terms of superior redox activity and theoretical energy capacity. Although TMOs share many similar characteristics, they are different in their crystal structure and redox behavior. Transition metal oxides with spinel crystalline structure are among the transition metal oxides that show promising electrochemical capacitor behavior. The spinel structure with a general formula of AB_2O_4 has a robust crystalline structure with three-dimensional diffusion pathways. In a spinel structure, oxygen atoms form a closed-pack structure, while cations of A and B occupy octahedral and tetrahedral sites. There have been studies on different spinel

oxides including Mn_3O_4 [57], Fe_3O_4[58], and Co_3O_4[59], and mixed transition metal spinels such as $MnFe_2O_4$[60] and $NiCo_2O_4$.[61]

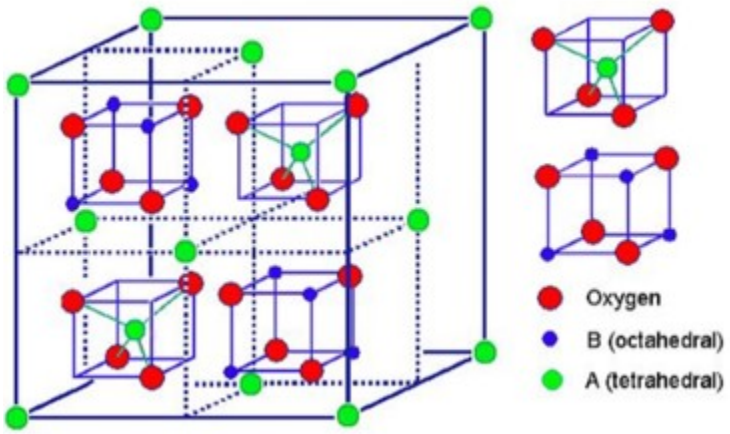

Figure 2.2. The crystalline structure of spinel oxides unit cell (Source: LibreTexts project)

Among the mentioned structures, Mn_3O_4 exhibits poor electronic conductivity leading to a capacitance much lower than theoretical values for and the mechanism is not fully established, but it is known that it involves the reversible redox reaction of Mn^{3+} to Mn^{2+}.[62] Furthermore, the pseudocapacitance behavior of Fe_3O_4 and $MnFe_2O_4$ is deficient.[52]

Spinel cobaltites with a general formula of MCo_2O_4 where M= Co, Ni, Cu, Mn, Cu, etc. Co_3O_4, $NiCo_2O_4$, and $MnCo_2O_4$ show different behavior comparing to other spinels due to their energy storage mechanism. They show a significantly higher capacitance due to the formation of oxyhydroxides during the charge storage process. In alkaline electrolytes, the redox reaction involves the formation of transition metal oxyhydroxides, which are usually formed in battery-type metal oxide-based electrodes. Equation (25) demonstrates the redox reaction for these materials:

$$MCo_2O_4 + OH^- + H_2O \leftrightarrow MOOH + 2CoOOH + 2e^- \quad (25)$$

However, $CoOOH$ undergoes a second redox process as described below:

$$CoOOH + OH^- \leftrightarrow CoO_2 + H_2O + e^- \quad (26)$$

These materials, exhibit pseudocapacitive (eq. (25)) and battery ((26)) behavior for energy storage.

Among the spinel cobaltites, Nickle cobaltite shows particularly high capacitance even at high charge/discharge rates. This comes from both good conductivity of $NiCo_2O_4$ (and utilizing both Ni and Co as electroactive materials.[63] The oxidation state distributions in nickel cobaltite has been reported to be uncertain and it can be generally formulated as $Co^{2+}_{1-x}Co^{3+}_x[Co^{3+}Ni^{2+}_xNi^{3+}_{1-x}]O_4$ with x ranging from 0 to 1 (the cations outside the brackets represent the tetrahedral sites and the ones within the brackets occupy the octahedral sites). $NiCo_2O_4$ shows at least two orders of magnitude higher conductivity comparing to monometallic nickel oxide (NiO) and cobalt oxide (Co_3O_4) because of the electron transfer between the cations with low activation energy.[64] In general, ternary metal oxides, show a much higher electrical conductivity, which enhances their charge storage performances, especially at high rates.[65]

As it is discussed above, the spinel cobaltite materials show both capacitive and battery-type behavior as is shown in eq. (25) and eq. (26). Thus, it is expected by tailoring these materials in nanoscale, the pseudocapacitance contribution would be emphasized.

To design nickel cobaltite electrodes with ideal pseudocapacitive performance, it is necessary to consider the main variables that play roles in the electrochemical performance of the system, which are the activity of electroactive materials of the electrode, electron transport, and electrolyte and active ions involved in the redox reactions.

The microstructure and morphology of the electroactive materials on the electrode play a crucial role in the enhancement of the electrochemical performance of the system. With that being

said, the fabrication of structures with tunable size and desirable macro/mesopores is of great interest to achieve the most desirable performance of the electrode materials. Generally, metal oxides have been studied with various morphologies, each presenting different advantages and features. A summary of these morphologies and their features has been presented in table 2.1.[66] The recent studies have been focused on synthesizing materials with desirable morphology and defect chemistry but overall 3D nanostructures show superior performance in energy storage.3D nanostructures provide continuous electron transport channels since their large volume 3D channels act as an electrolyte ion reservoir and they present higher mechanical stability moderating volume expansion during the charge/discharge process.

Nanosheets or nanoflakes	(i) The porous nanosheets/ nanoflake with a large specific surface area and porous configuration can greatly improve the electrode/electrolyte contact area and shorten the diffusion paths. (ii) The porous feature of the nanosheets/nanoflakes largely increases the number of electroactive sites. (iii) The nanosheet/nanoflake morphology is advantageous for efficient ion and electron transport and better accommodating the
Nanowire (NWs) @nanoflakes core-shell structure	(i) Ultrathin nanoflakes enable a fast, reversible Faradaic reaction, and provide a short ion diffusion path and maintain the structural integrity of the core during the charge-discharge process.

	(ii) Slim and mesoporous NWs with good electrical conductivity serve both as the backbone and electron "superhighway" for charge storage and delivery and the mesoporous feature leads to a large electrode-electrolyte contact interface.
Nanoflake@nanowire hetero-structure	(i) The large opened channels in both nanoflake and nanowire enhance ion and electron diffusion, easier electrolyte penetration which enhances the utilization of the active materials. (ii) The unique heterostructure offers richer active sites for electrochemical reactions, including contributions from both the nanoflakes and nanowires. (iii) The hetero-structure array, consists of the interconnected flake network while the nanowires supported at the edge of the nanoflakes with a cross configuration both make a stable structure which helps to alleviate the structural damage caused by volume expansion during the cycling process, resulting in enhanced stability.
Mesoporous nanoparticles	(i) The mesopores nanoparticles provide the short ion-transport pathways and favor the direct contact of electrolytes to the interfacial electrochemically active species. (ii) Facilitate mass diffusion/transport (e.g., electrolyte penetration and ions transport) and ensure high electro-active surface area.
Nanoneedles	(i) The small diameter of the nanoneedles leads to a high surface area, which surely contributes to the high capacitance.

	(ii) The well-defined and distinct structure of nanoneedles provides most of the surface easily accessible for electrolytes, which will give high capacitance and enhanced electrochemical kinetics. (iii) The single-crystalline nature of nanoneedles contributes to the cycling stability during the extended charge/discharge process, by facilitating the electron transfer and providing strong mechanical robustness.
3D Aerogels	3D networks of nanoparticles with an average pore size of several nanometers provide a mesoporous structure with high specific surface areas and porosities, which reduce the mass-transfer resistances, involved in electrolyte penetration and ion diffusion, and ease the electron hopping between neighboring nanoparticles.

Table 2.1. Different nanostructures developed for high-performance supercapacitors [66]

Although size-controlled production of electroactive materials could increase their pseudocapacitive performance but increasing short ion pathways and their surface area, these materials still suffer from poor conductivity when they are compared with highly conductive materials used for EDLCs. Therefore, electrodes with enhanced charge carriers and better conductivity are desirable. Another approach is to produce hybrids with highly conductive materials to enhance electrochemical performance.

2.2.2 Metal oxide hybrid components:

The incorporation of materials with high conductivity into faradic electrodes, results in faster charge-transfer kinetics, hence improving charge-storage capability, especially at higher

rates. This approach focuses on maximizing the coupling effects of individual components that compose the electrode. Carbon-based nanomaterials that exhibit high conductivity, high surface area, and good mechanical stability such as graphene, carbon nanotubes (CNTs), and carbon nanofibers (CNFs) are of great interest to be incorporated with faradic electrodes. In this regard, graphene-based electrodes are great candidates for improving the performance of metal oxides. The resultant composite should not be considered just the sum of each component, but a new material with new properties.[67] Graphene is ideal support for anchoring and uniform dispersion of electroactive metal oxides. Graphene also provides a 2D conductive building block to assemble 3D conductive structures, which would improve the slow charge transfer associated with poor conductivity of metal oxides as well as providing accessible ion pathways. The oxygen-containing groups on the graphene structure result in good binding and interfacial interactions. On the other hand, metal oxides also prevent the graphene sheets from stacking and losing their surface area.[67]

One of the unfavorable phenomena that happen during the metal oxide preparation is the agglomeration and hence losing active surface area. Thus, GO and rGO are good 2D support for nucleation and growth of metal oxides. Generally, in this approach, GO or rGO is dispersed in a solvent by electrostatic stabilization or chemical functionalization. GO or rGO is a good template for chemical reactions with metal cations as the chemical functional groups on the surface of GO or rGO serve as binding sites for metal cations. By undergoing hydrolysis or in situ redox reactions of the metal salts, the metal oxide precursors are anchored on the surface of the 2D support, forming metal oxide particles by further annealing. As it is shown in Figure 2.3, hydrous Co_3O_4 particles that are formed without the presence of graphene support, tend to agglomerate and form particles much bigger than the Co_3O_4 particles formed on graphene.

Moreover, Dai and co-workers found that the size, crystallinity, and morphology of metal oxides is strongly dependent on the oxygen-containing functional groups of the graphene substrate.[68]

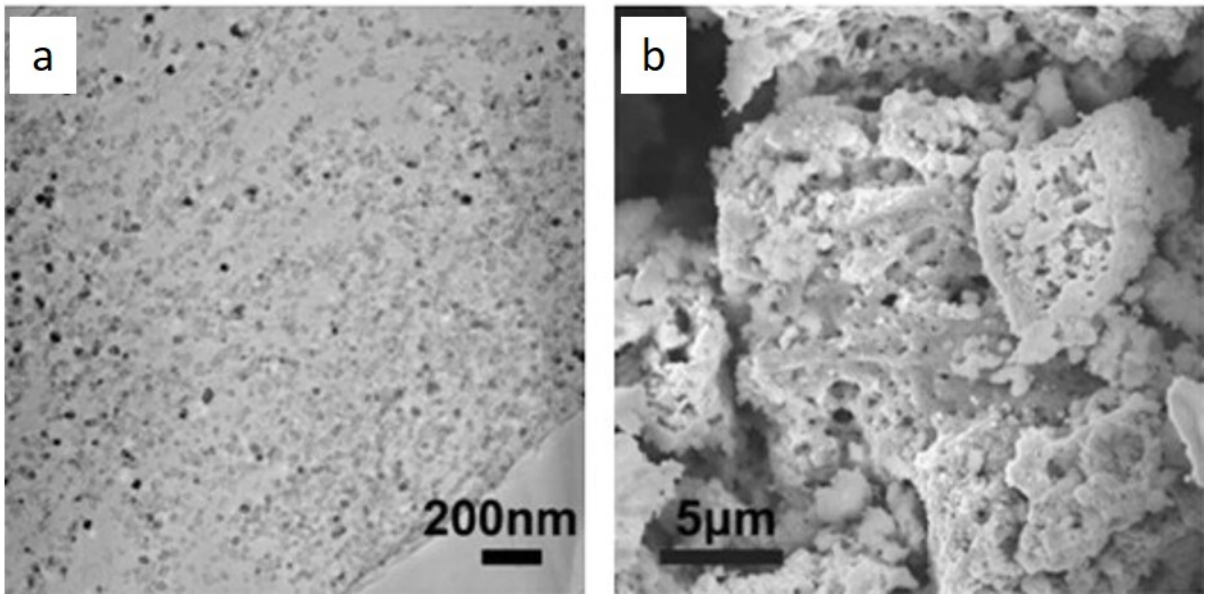

Figure 2.3. a) TEM image of graphene/Co3O4 composite and b) SEM image of Co3O4 without graphene support[69]

Another advantage of using hybrid metal oxides is to improve the cycling rate stability of the electrodes. Metal oxides usually present poor cycling stability due to the volume change that they undergo during the charge/discharge process. Anchoring metal oxides uniformly onto the surface of conductive support, wrapping it with conductive 2D layers, or capsulation of metal oxide by scaffold results in a better bearing of mechanical stress and preventing the pulverization of active materials. 2D ultrathin structures such as graphene with high mechanical flexibility and electrical conductivity are favorable candidates.[70,71]

Overall, designing hybrid metal oxide structures is a promising method for optimal electrode design for energy storage devices. Using carbon-based metal oxide composites is indeed

a promising class of advanced materials for energy storage. Graphene/metal oxide composites are special materials of interest due to the synergetic effects of enhanced available surface area, developed conductive network, and shortened ion transport paths in the composite in comparison to each one of the materials separately[68]. A good understanding of the surface chemistry of carbon-based materials and how it is possible to increase the charge transfer between the electroactive material and the conductive network by using covalent or noncovalent techniques is also necessary to further improve the performance of the hybrid metal oxide devices.[67]

2.3 State of the art

There have been different strategies proposed to develop high-performance pseudocapacitive electrodes. The advanced approaches mainly focus on introducing more electrochemically active sites, shortening ionic pathways, faster charge transfer kinetics. This will be only achieved by careful selection of appropriate pseudocapacitive material as well as rational design of hybrid electrode architecture. There are different aspects to consider when it comes to optimizing the favorable characteristics of a pseudocapacitive electrode. Nickel cobaltite is a promising material to be used as a pseudocapacitor. While tuning the structural morphology, particle size and guest ion can drastically change its behavior from pseudocapacitive to battery-like behavior, the rational design of hybrid structure also plays a key role to take advantage of the different merits of each component. Although there has been a lot of studies regarding metal oxide composites and their performance in energy storage devices, yet there are still a lot of fundamental studies needed. In this study, we tend to focus more on exploiting methods to improve the electrochemical performance of nickel cobaltite composites in different aspects. Firstly, by trying to understand better the metal oxide composite formation and structural dependency on conductive scaffolds and how the surface functional groups change the morphology of the metal oxide.

Secondly, by trying to fabricate metal oxides with a large number of electroactive sites and high surface area and tuned porosity to gain higher transport rates for both electrons and ions.

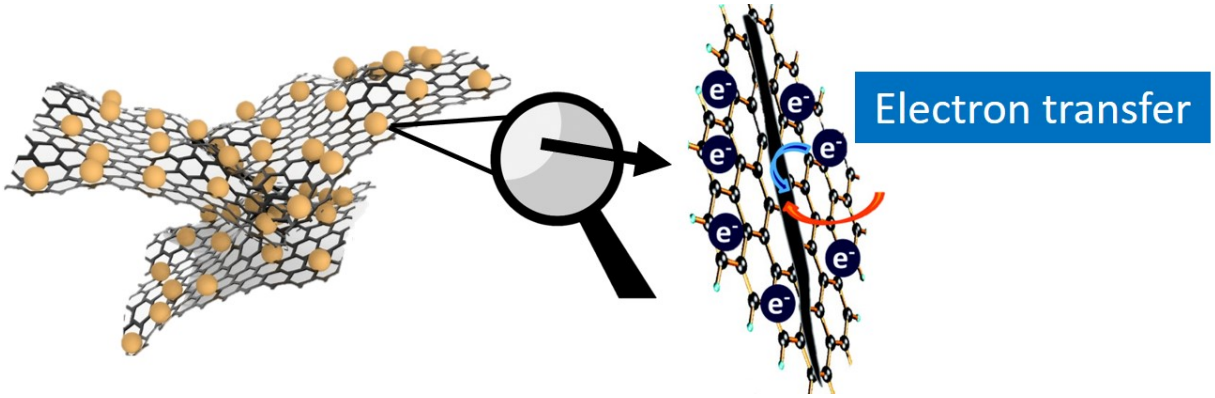

Figure 2.4. Schematic illustration showing how a conductive background such as graphene could enhance the charge transfer properties of metal oxides with low conductivity

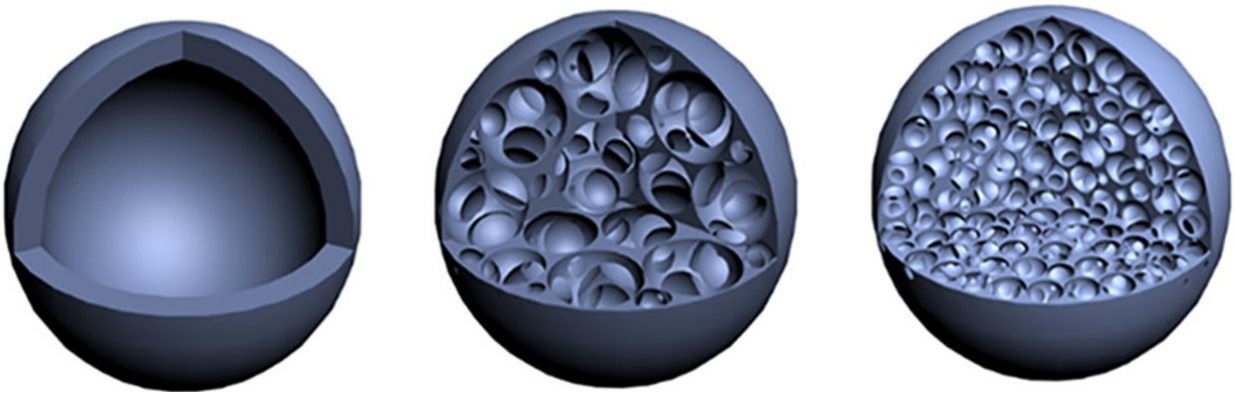

Figure 2.5. Conceptual demonstration of nanoparticles with different structural properties that could greatly affect diffusion rate active ions and ion-accessibility of active sites

Chapter 3: Electrophoretic Deposition of Nickel cobaltite Composite Electrode for All-solid-state Asymmetric Supercapacitor Application

3.1 Abstract

Nickel cobaltite composite electrodes were fabricated by a fast, scalable, and cost-effective electrophoretic deposition for supercapacitor applications. $NiCo_2O_4$/PANI/rGO composite electrode went through heat treatment under nitrogen to carbonize PANI after electrophoretic deposition. $NiCo_2O_4$ platelets, distributed on carbonized polyaniline-rGO network, were active in charge storage with high capacitance, excellent rate capability (1235 F g^{-1} at 60 A g^{-1}), and acceptable cycling stability (3000 cycles at 10 A g^{-1}) in a three-electrode assembly. The practical application of the composite electrode was investigated by an all-solid-state asymmetric supercapacitor cell using $NiCo_2O_4$/C-PANI/rGO as the cathode and activated carbon as the anode with a specific capacitance of 262.5 F g^{-1} at 1 A g^{-1} and good capacitance retention of 78% after 3500 cycles at an expanded working potential of 1.5 V. This work shows the importance of composite assembly process that governs the microstructure of the composite.

3.2 Introduction

Batteries and capacitors have been introduced as promising candidates for sustainable energy storage devices such as hybrid electric vehicles and consumer electronic devices. Durable cycle life, high power/energy density, low material cost, and environmental benignity are the properties that researchers are working on for the next generation of electrical and electrochemical energy storage devices.[5,72] The research in the battery field is more mature and ECs have attracted more attention recently. Introducing new materials has reduced the gap in electrochemical

characteristics of ECs and batteries, combining the high energy density of batteries with the high power density of ECs.[9,52] Transition metal oxides (TMOs) are promising materials in terms of superior redox activity and theoretical energy capacity.[73–75]

Spinel cobaltites with a general formula of MCo_2O_4 where M = Co, Ni, Cu, Mn, Cu, etc. show promising electrochemical capacitor behavior, combining properties of both metal ions.[70,76–78] Co_3O_4[79], $NiCo_2O_4$[63], and $MnCo_2O_4$[80] show different behavior comparing to other spinels due to their energy storage mechanism. They show a significantly high capacitance due to the formation of oxyhydroxides during the charge storage process.[52] Among the spinel cobaltites, nickel cobaltite shows particularly high capacitance even at high charge/discharge rates. This comes from better conductivity of nickel cobaltite and utilization of both Ni and Co surface sites for charge storage.[63] $NiCo_2O_4$ shows at least two orders of magnitude higher conductivity comparing to monometallic nickel oxide (NiO) and cobalt oxide (Co_3O_4) because of the electron transfer between the cations with low activation energy.[64,65] However, the intrinsic conductivity of $NiCo_2O_4$ is still poor and $NiCo_2O_4$ electrode materials even prepared in nanoscale seriously agglomerate, reducing the rate capability and cycle stability of supercapacitors.[81,82]

The incorporation of materials with high conductivity into faradic electrodes, results in faster charge-transfer kinetics, hence improving charge-storage capability, especially at high rates. This approach focuses on maximizing the coupling effects of individual components that compose the electrode. Carbon-based nanomaterials that exhibit high conductivity, high surface area, and good mechanical stability such as graphene, carbon nanotubes (CNTs), and carbon nanofibers (CNFs) are of great interest to be incorporated with faradic electrodes.[83–86] In this regard, graphene-based electrodes are great candidates for improving the performance of metal oxides through high electrical conductivity, mechanical strength, and inherent flexibility. Graphene also provides a 2D

conductive building block toward porous 3D conductive structures that would provide accessible ion pathways and facilitate charge transfer overcoming poor conductivity of metal oxides.[67,87,88] When composites are considered for electrode application, it is desired to have a simple yet scalable fabrication scheme. Many efforts are focused on materials synthesis only; however, if there is no scalable fabrication route for carefully designed electroactive materials, it is hard to expect that the newly designed material will make an impact in a real application.

An unfavorable phenomenon that happens during the preparation of electrodes is the agglomeration that causes the loss of active surface area. The conventional method to fabricate electrodes is the slurry-coating method, which contains electroactive materials, conductive agents, and binders to the current collector. If binders that do not participate in the energy storage process are used, they will block/take up a portion of the electrode surface. This would be a "dead surface" as described in the literature.[89,90] Electrophoretic deposition (EPD) has been introduced as a promising technique for the deposition of nanomaterials on conductive substrates. In this process, the properties of deposits can be controlled by parameters related to the electric field and suspension. EPD provides a fast fabrication process that is cost-effective, suitable for mass production, and flexible to be used for the substrate with different shapes, while preparing a stable suspension with sufficient particle surface charge and controlling possible side reactions are factors that might limit its abundant use. [91–93] Although there have been researches regarding exploiting EPD for electrode fabrication in energy storage, they mostly have been only focusing on the deposition of a single component rather than multi-components [94–97] or using surfactant binders to tune the surface charge of the particles.[98]

In this research, we utilize 15-second electrophoretic deposition as a convenient, cost-effective, and scalable method to fabricate nickel cobaltite composite electrodes for high-

performance supercapacitor application. Nickel cobaltite platelets, polyaniline, and reduced graphene oxide (rGO) are synthesized separately yet deposited simultaneously to form a $NiCo_2O_4$/PANI/rGO ternary composite electrode. Later, heat treatment of as-prepared $NiCo_2O_4$/PANI/rGO composite causes carbonization of PANI and removal of I_2 additive. In this particular structure, the metal oxide platelets and rGO forms a conductive network with shortened ion transport paths[68] while the carbonized polyaniline gives mechanical integrity and prevents aggregation of rGO sheets and oxide platelets leading to the high surface area. The porosity formed in this hybrid film provides buffer space for volume change during cycling and easy access of electrolytes to active sites.

3.3 Experimental procedure

3.3.1 Nickel cobaltite synthesis: nickel cobaltite was synthesized using a simple hydrothermal method. 0.6667 g $Co(NO_3)_2.6H_2O$ and 0.3333 g $Ni(NO_3)_2.6H_2O$ were dissolved in 20 mL of DI water at room temperature. The solution was then mixed with 22 mL of NaOH solution under magnetic stirring until it changes its color to green. Then, the resulting solution was transferred into a Teflon-lined stainless-steel autoclave and heated for 140 °C for 12 h. The resultant precursor was centrifuged and washed. It was grounded finely after drying and calcinated at 400 °C for 3 h using a 1 °C min^{-1} heating ramp to obtain the final $NiCo_2O_4$.

3.3.2 GO/rGO synthesis: GO was synthesized using a modified Hummers method. Two grams of graphite powder was sonicated and stirred in an ice bath in 92 mL of concentrated H_2SO_4 with 2 g of $NaNO_3$ for 30 min, after which 12 g of $KMnO_4$ was very slowly added. Sonication continued for 30 min following the addition of $KMnO_4$, after which the flask was removed and allowed to stir slowly overnight at 30 °C. Next, 100 mL of deionized water was added dropwise followed by

1 h of stirring. Finally, 600 mL of 3% H_2O_2 was added into the flask, yielding a yellowish-brown GO suspension. The suspension was washed three times with concentrated 1 M HCl (BDH) via centrifuge, and finally five times with DI water. To reduce GO into rGO, 3 mL of 1 M L-ascorbic acid and 4.5 mL of ammonium hydroxide were added to 1.5 L water-based GO dispersion (0.1 mg/mL). The solution was kept at 90 °C for 90 minutes until the reaction was complete. The solution was cooled down to room temperature to be filtered and washed several times with DI water and ethanol. The washed solid was dried in the oven at 60 °C overnight.

3.3.3 Polyaniline preparation: 15 mL aniline monomer was added to 300 mL of aqueous 1 M HCl., which was then placed on the high stir. To the solution, 17.35 g ammonium persulfate in 200 mL of 1 M HCl (0.38 M) was added then stirred vigorously for 1 min. After 1 minute, the stirring speed was reduced. The polymerization took place for 3 h and the product was vacuum filtered to yield a dark green solid, which was washed with excess 1 M HCl and acetone. The resulting poly(aniline) emeraldine salt (PANI ES) was dried under vacuum overnight. To obtain the emeraldine base (PANI EB), PANI ES was ground with mortar and pestle then washed with 1M NH_4OH and water. The resulting dark blue powder was dried under a vacuum overnight.

3.3.4 Fabrication of the electrodes: To perform electrophoretic deposition (EPD), solid particles were dispersed in 20 mL of acetone followed by adding 20 mg of I_2. In the EPD process, charged particles in a suspension are deposited onto an electrode under an electric field. This method is convenient and easily scalable, making it suitable for mass production and allows flexibility in the electrode shapes. I_2 is used herein acetone to charge up particles with the protons generated by the reaction between acetone and I_2. By controlling the mass input ratio in the EPD suspension, three different versions of composites were deposited: two binary composites and one ternary composite. $NiCo_2O_4$/rGO and $NiCo_2O_4$/PANI composites were deposited with EPD suspension

that has a 5:1 mass ratio of nickel cobaltite to the other component (rGO or PANI). For the ternary composite, we introduced a 1:1 mass ratio between PANI and rGO such that we have a 10:1:1 mass ratio between nickel cobaltite, PANI, and rGO. To have homogeneous EPD suspension, all components were sonicated for 2 h in acetone. The EPD deposition was carried out under potentiostatic conditions, using a DC power supply (Agilent 6645A). The deposition substrate (working electrode) was a 1 cm × 0.8 cm nickel foam and the counter electrode was a 1 cm × 1 cm stainless steel electrode. The two electrodes were placed 1 cm apart with 30 volts applied between them. After deposition, electrodes were dried overnight in a vacuum oven and then annealed under N_2 flow at 400 °C for 2 h with a heating rate of 5 °C min^{-1} to remove I_2 from the electrodes as well as partially carbonizing PANI (indicated as C-PANI).

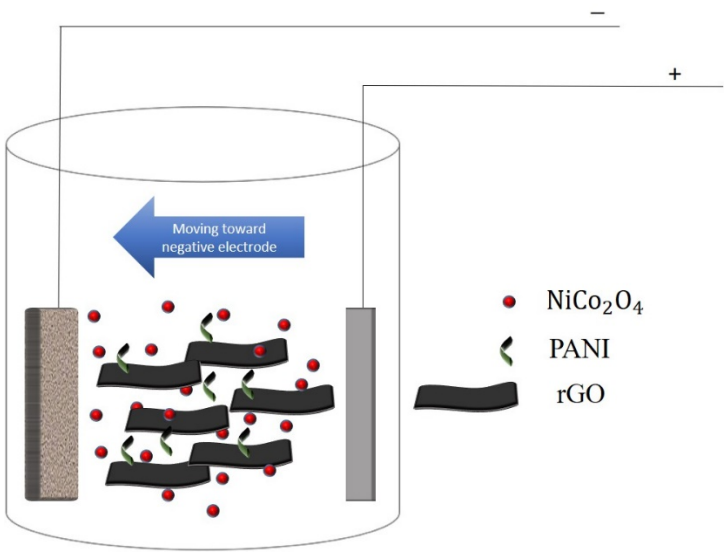

Figure 3.1. Schematic of multicomponent EPD process

3.3.5 Characterization: The crystallographic structure of the materials was studied using a PROTO AXRD theta-theta X-ray diffractometer operated using a Cu Kα radiation (40 kV, 30 mA). JEOL JSM-7000F scanning electron microscope (SEM) was used to observe the morphology of the as-prepared materials. Nitrogen adsorption-desorption provided surface area and pore size

distribution via Brunauer–Emmett–Teller (BET) method and Barrett–Joyner–Halendar (BJH) method. Raman scattering was excited by a 514 nm line air-cooled 20 mW argon ion laser using a Renishaw inVia Raman microscope system. FTIR spectra of the samples were analyzed using a ThermoScientific iS-50 FTIR analyzer. XPS scans were acquired using an AXIS Ultra DLD (delay lines detector) X-ray photoelectron spectrometer (XPS, Kratos Analytical). A monochromatic Al Kα X-ray source was used as the photon source.

3.3.6 Electrochemical measurements: The electrochemical properties of the as-prepared electrodes were investigated using a three-electrode setup or a two-electrode all-solid-state asymmetric cell at room temperature using a PARSTAT 4000 potentiostat (Princeton Applied Research).

The three-electrode cell had a Pt coil counter electrode, an Ag/AgCl reference electrode, and a 6 M KOH electrolyte. Composites deposited on Ni foam (0.8 cm × 1.0 cm) with a mass loading of 0.5~0.7 mg were used as working electrodes. Cyclic voltammetry (CV) was carried in a potential window ranging from 0 to 0.6 volts, and potentiostatic charge/discharge was carried from 0 to 0.5 volts. Potentiostatic EIS studies were performed using 10 mV amplitude with frequencies ranging from 0.01 Hz to 100 kHz. The specific capacitance (C_s) of a single electrode is calculated from the galvanostatic discharge curves using the equation below:

$$C_s = \frac{I \times \Delta t}{(\Delta V) \times m} \quad (27)$$

Where C_s (F g^{-1}) is the specific capacitance of the electrode, I (A) is the current, Δt (s) is the discharge time, m (g) is the deposited mass on the nickel foam, and ΔV (V) is the working potential window.

3.3.7 All-solid-state asymmetric cell assembly: The asymmetric supercapacitor in this work was assembled with the solid-state polymer gel electrolyte (PVA/KOH) as the separator and electrolyte between positive and negative electrodes in a coin cell assembly. The alkaline PVA/KOH polymer electrolyte was prepared by a solution casting method reported in the literature.[99] 6 g of PVA was dissolved in 50 mL of DI water with stirring at 80 °C until a clear solution was formed then a solution containing 6 g of KOH dissolved in 10 mL of DI water was added. The final solution was stirred for another 3 h at 70 °C. Finally, the viscous solution was dried slowly in a petri dish at room temperature to get a homogenous white thin film. For all-solid-state cell assembly, the as-prepared nickel cobaltite/C-PANI/rGO on nickel foam was used as the cathode, punched in a circular shape. To prepare the anode, activated carbon (TF-B520, MTI) was mixed with carbon black and PVDF at an 85:7.5:7.5 weight ratio in NMP organic vehicle. The resulting slurry was coated over Ni foam and dried at 80 °C overnight. For optimal performance of asymmetric supercapacitors, the positive and negative electrode mass ratio should be determined based on charge balance; therefore, the following equation is used:

$$\frac{m_+}{m_-} = \frac{C_- \times \Delta V_-}{C_+ \times \Delta V_+} \quad (28)$$

where m, C and ΔV, represent the mass loading of active materials, the specific capacitance, and the voltage window of the cell. The $NiCo_2O_4$/C-PANI/rGO to anode mass ratio, 1:3.7, was calculated and used for the cell assembly. The energy density (E, J kg^{-1}) and power density (P, W kg^{-1}) of asymmetric supercapacitors are calculated by:

$$E = \frac{1}{2} CV^2, \; P = \frac{E}{\Delta t} \quad (29)$$

where C (F g^{-1}) is the specific capacitance of the asymmetric supercapacitor cell, V (V) is the working potential, and Δt (s) is the discharge time.

3.4 Results and discussion

3.4.1 Materials characterization studies and analysis

The structural characterization and properties of each of the individual materials were investigated separately. As it is shown in Figure 3.2a, the crystallinity and crystal phase of the nickel cobaltite nanoparticles were studied using X-ray diffraction. The XRD patterns agree well with the spinel phase of $NiCo_2O_4$ (JCPDS No. 20-0781). Nitrogen adsorption measurements were further carried out to study the surface structure of the $NiCo_2O_4$ platelets. The nitrogen adsorption/desorption isotherm reveals a type IV isotherm which shows a minor hysteresis loop in the range above around 0.9 relative pressure, a characteristic of mesoporous materials. The specific surface area (SSA) and average pore diameter are found to be 67.17 $m^2 g^{-1}$ and 7.6 nm, and pore size ranges from 1.8 nm to 8.9 nm (Figure 3.2b and inset). Raman spectroscopy was also exploited to characterize the chemical structure of as-prepared $NiCo_2O_4$ nanoparticles. As it can be seen in Figure 3.2c, the peaks at 348, 468, 500, and 660 cm^{-1} in the Raman spectrum of $NiCo_2O_4$ could be assigned to E_{2g}, E_g, F_{2g}, and A_{1g} modes respectively.[100,101]

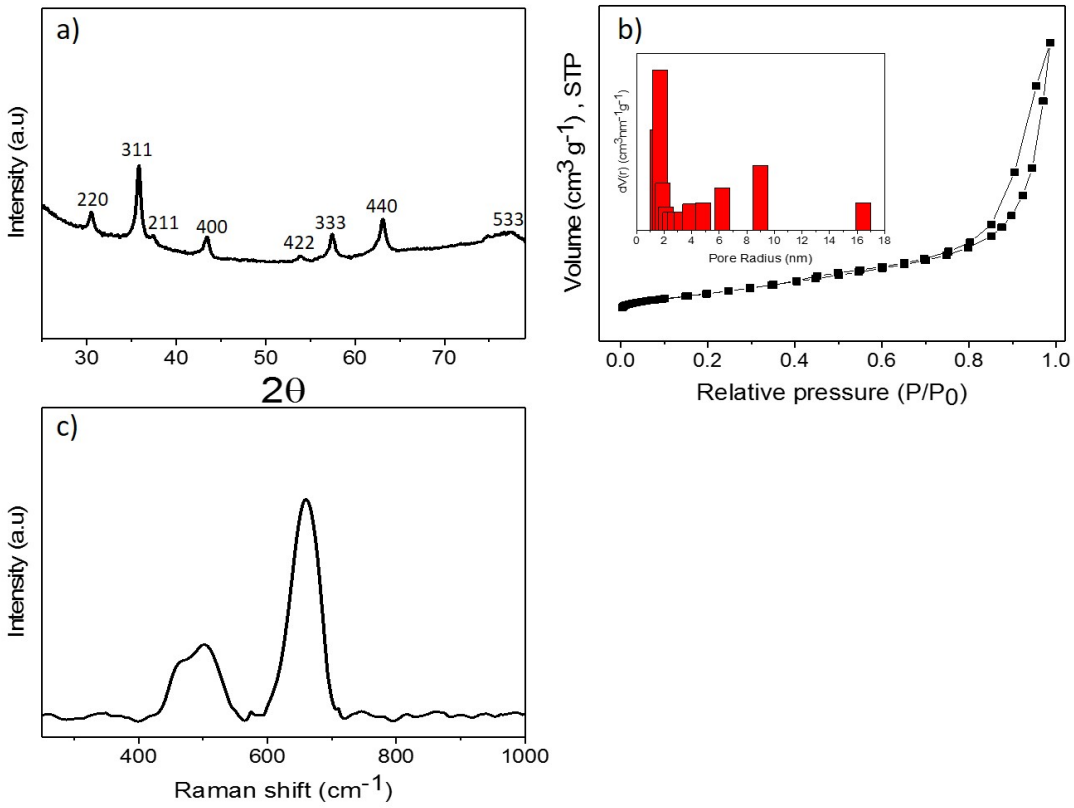

Figure 3.2. a) XRD pattern of as-synthesized $NiCo_2O_4$. b) Nitrogen adsorption/desorption isotherm exhibiting mesoporous structure of $NiCo_2O_4$ materials. The inset shows pore radius distribution. c) Raman spectrum of $NiCo_2O_4$.

As-synthesized $NiCo_2O_4$ powder was characterized by XPS to evaluate their surface chemical compositions and chemical bonding states. The signals of O 1s, Co 2p, and Ni 2p core levels are detected on the full spectra as expected (Figure 3.3a). O 1s consists of four distinguishable oxygen contributions which are marked as O1, O2, O3, and O4 (Figure 3.3b). Respectively, these correspond to the metal-oxygen bond,[102] the oxygen in hydroxyl groups,[103] the high number of defect sites with low oxygen coordination in the material with small particle size,[104] and the multiplicity of physi-/chemisorbed water at and within the surface.[102] The Co 2p spectra in Figure 3.3c show two spin-orbit doublets which contribute to Co^{2+} and Co^{3+} and shakeup satellites (marked as "sat"). In addition, the Ni_{2p} spectra in Figure 3.3d also shows two spin-orbit

doublets arising from Ni^{2+} and Ni^{3+} and two shakeup satellites. It has been suggested that mixed valences of cobalt and nickel cause higher electrical conductivity than monometallic nickel and cobalt oxides because of lower activation energy of electron hopping between the cations leading to an efficient electrochemical performance at high rates for the oxide.[64,81]

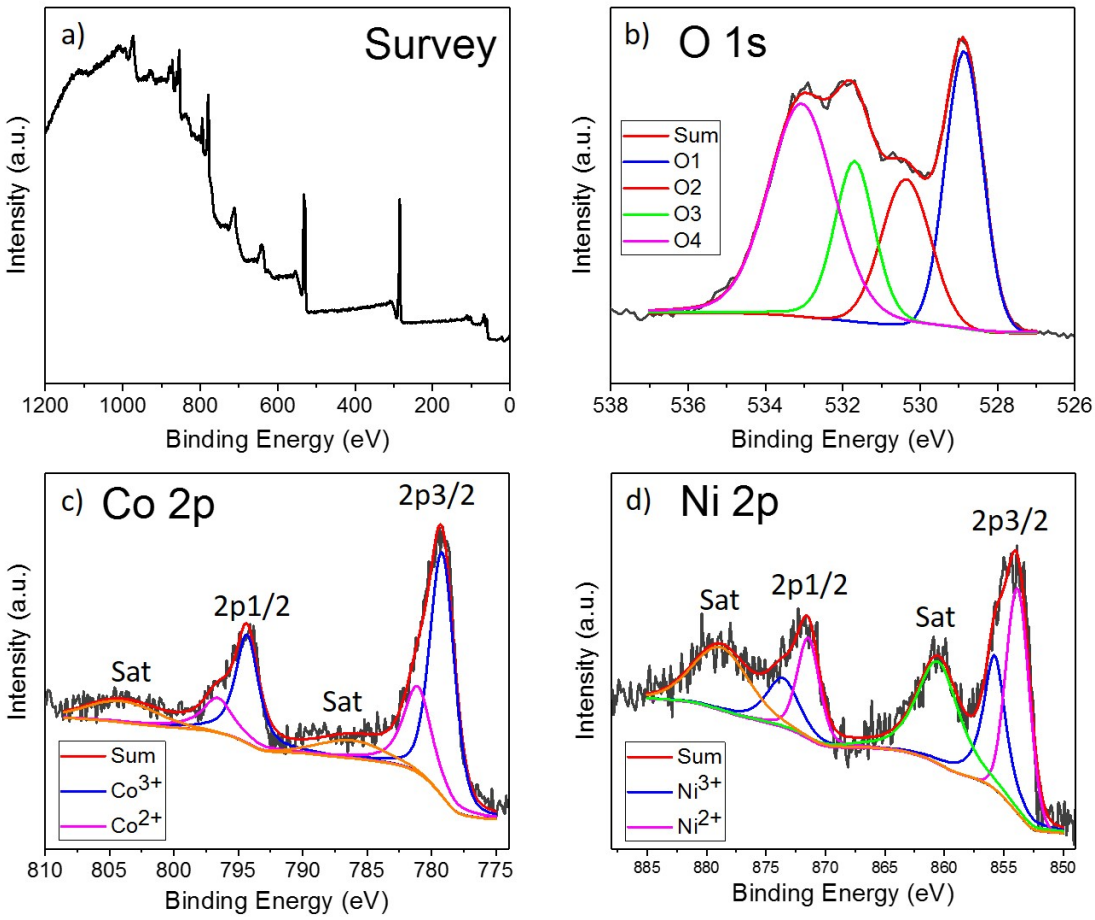

Figure 3.3. XPS patterns of as-synthesized $NiCo_2O_4$ materials. a) Full scan, b) O 1s core levels, c) Co 2p core levels, and d) Ni 2p core levels.

To characterize rGO, XRD, Raman spectroscopy, and FTIR were employed. As it is indicated in Figure 3.4a, the XRD pattern recorded for GO and rGO confirms the successful production of rGO. The peak at $2\theta = 9.5°$ corresponds to the (001) reflections of GO. The various

functional groups like hydroxyl, epoxy, and carboxyl groups attached to the basal planes and edges of crystal planes caused an increase in d spacing to around 0.84 nm. While for the rGO the appearance of a peak at $2\theta = 24.2°$ corresponds to (002) reflections and indicates a decrease in lattice spacing to around 0.37 nm. This is due to the removal of oxygen-containing functional groups and contraction of d spacing. It is also worth mentioning that the peaks appearing at $2\theta = 42.3°$ for GO and $2\theta = 42.9°$ for rGO corresponds to short-range two dimensional (100) reflections which are caused by stacked sheets.[105,106]

Raman spectra of GO and rGO are shown in Figure 3.4b. The two distinct peaks arising at 1358 cm^{-1} and 1578 cm^{-1} are respectively the D and G bands that are commonly observed for all graphitic structures. While the G band originates from the E_{2g} vibrational mode of the sp^2 bonded carbon atoms and the D band is attributed to a breathing mode of k point phonon with A_{1g} symmetry. G band is a result of C-C bond stretching in graphitic materials and is common to all sp^2 carbon systems. The D band is caused by the presence of disordered sp^2 hybridized carbon systems and is associated with local defects and disorder in the rGO. It should be also noted that a 2D band was also located at 2629 cm^{-1} that comes from the second-order overtone, which is due to the secondary inelastic scattering from a second phonon.[107] The increase in D/G intensity ratio for rGO, compared to that in GO suggests a decrease in the average size of the sp^2 domains upon reduction of the GO.[108]

FTIR technique was also used to determine the functional groups present in the carbon structures. The FTIR spectra of GO and rGO show (Figure 3.4c) characteristic vibrations at 1041, 1322, and 1725 cm^{-1}, which are assigned to the C=O, C-OH, and C-O-C groups. The peak arising at 1614 cm^{-1} indicates the water absorption of GO and rGO sheets, and the broad peak at 3400 cm^{-1} corresponds to O-H groups.[109] The intensity of characteristic peaks to oxygen-containing

functional groups were decreased in the rGO spectrum, confirming the successful reduction of GO into rGO.

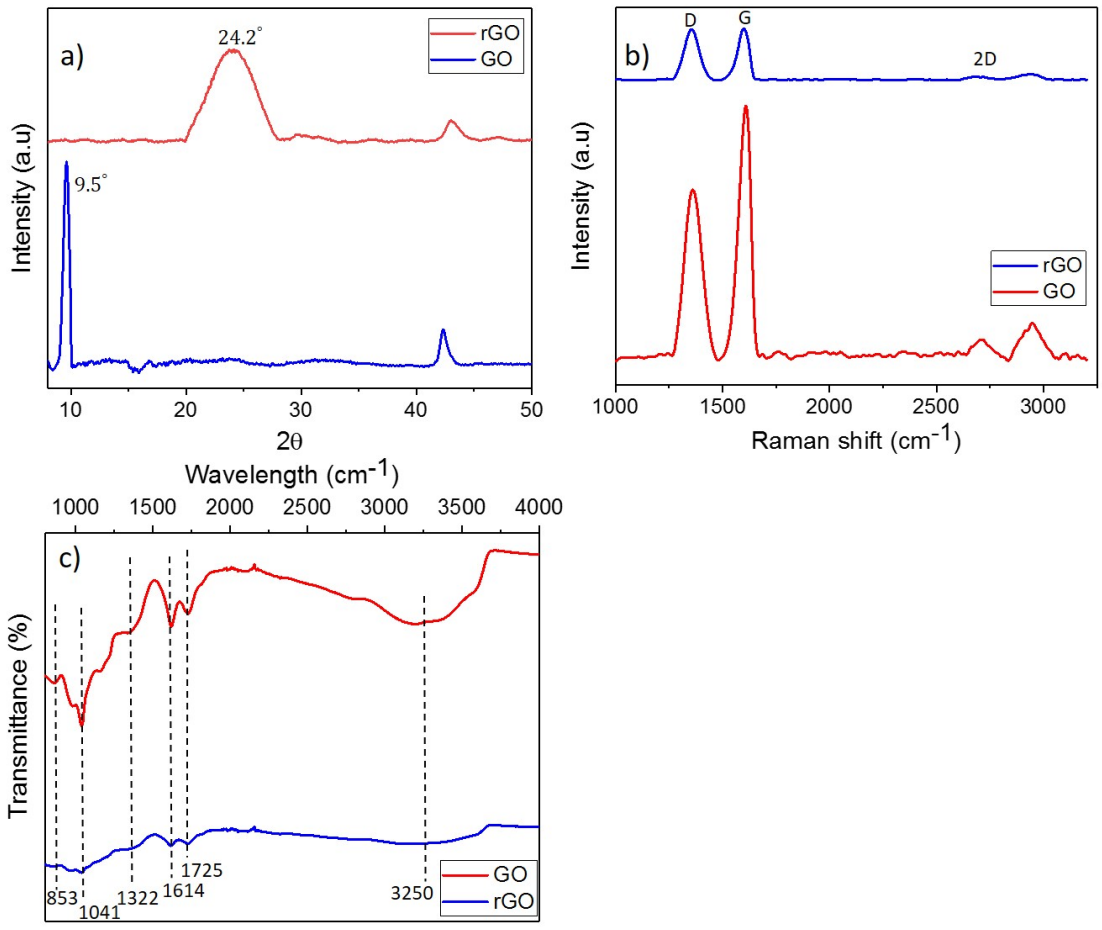

Figure 3.4. a) X-ray diffraction patterns. b) Raman spectra. c) FTIR spectra of GO and rGO

Polyaniline structure was also studied and analyzed using Raman spectroscopy and FTIR as convenient probes for organic compounds. Figure 3.5a shows the FTIR spectral of PANI. The peak arising at 821 cm^{-1} corresponds to bending of aromatic C-H in 1,4-disubstituted aniline units indicating the head-to-tail coupling in PANI.[110] The broad intense band of aromatic C-H deformation which is observed at around 1140 cm^{-1} is described as an "electronic-like band"[111] and is considered to be a measure of the degree of delocalization of the electrons. The peak at 1296

cm^{-1} is a characteristic of C≡N stretching. Respectively, vibrations occurring at 1488 cm^{-1} and 1580 cm^{-1} that are due to benzenoid and quinonoid rings are characteristics of the PANI backbone.[110]

In addition to FTIR, Raman spectroscopy of polyaniline confirmed the successful synthesis of granular PANI (Figure 3.5b). These data agree with other literature regarding the emeraldine base form of polyaniline. The peaks arising at 422, 525, and 845 cm^{-1} belong to the out-of-plane deformation of the benzene ring.[112,113] The peak at 782 cm^{-1} corresponds to quinine plane deformation.[113,114] The peak at 1163 cm^{-1} is for C-H bending vibrations of quinonoid rings. The peak at 1224 cm^{-1} in the spectrum is due to the C-N stretching vibrations.[112–114] The band arising at around 1325 cm^{-1} is associated with C∼$N^{+\bullet}$ stretching vibrations. The peaks at 1418 and 1630 cm^{-1} are connected to the phenazine-like or cross-linked structures.[112] The band at 1494 cm^{-1} belongs to the C=N vibration in quinonoid rings. The shoulder at 1560 cm^{-1} is for C-C stretching vibrations which are partially mixed with C-H bending vibrations in benzenoid rings. The peak at 1595 cm^{-1} can be assigned to C=C stretching vibrations of quinonoid rings.[112–114]

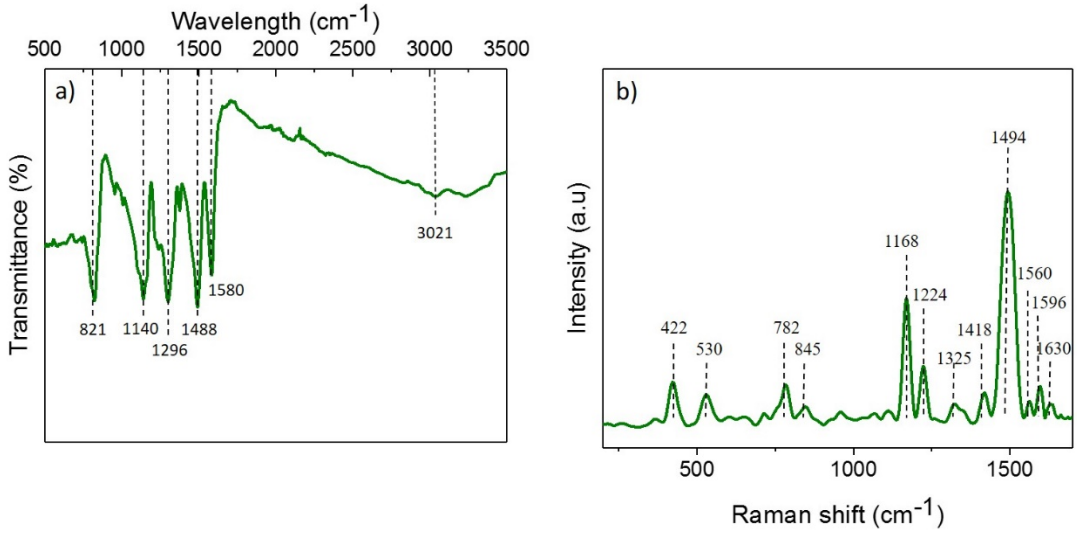

Figure 3.5. PANI emeraldine base a) FTIR and b) Raman spectra.

3.4.2 Electrode fabrication and EPD optimization

In the EPD process, applying a voltage between two electrodes generates a dc electric field, which acts as the driving force to move charged solid particles. Hamaker's law (Equation 30) is often used to model EPD processes. It predicts deposited mass as a function of deposition time:[92]

$$w(t) = \int_{t_0}^{t} f\mu EAC dt \quad (30)$$

where μ is the electrophoretic mobility, E is the electrical field strength, A is the electrodes surface area, ƒ stands for the efficiency coefficient of deposition ($f \leq 1$ since only a fraction of the particles contacting the electrode surface will be deposited), and C is the particle concentration in the suspension. It should be noted that the electric field needs to be strong enough to overcome the interparticle repulsion.[92,115] The electrophoretic mobility could be described as below:

$$\mu = \frac{\varepsilon_0 \varepsilon_r \zeta}{\eta} \quad (31)$$

where ε_0 is the permittivity of vacuum, ε_r is the dielectric constant of the dispersion medium, ζ, is the zeta potential and η is the viscosity of the liquid.

Considering the equations above, in a certain dispersion medium, while keeping the electric field and surface constant to perform a multicomponent EPD deposition, it is crucial to tune the electrophoretic mobility of each component to the same level.[90] According to Smoluchowski's theory, mobility is independent of particle size.[92] Then, a similar ionic charge on each component particle would cause similar zeta potential, ζ, thus resulting in similar electrophoretic mobility.

Nickel cobaltite, PANI, and rGO exhibit different zeta potentials in acetone, therefore, the addition of suitable dispersant to tune the zeta potential of all components is essential. I_2 is a good candidate. When introduced to acetone, I_2 generates protons. These protons are subsequently adsorbed onto the surface of particles in the suspension, making the particles charged with the same sign. The increased electrostatic repulsion force consequently makes the suspension more stable. The iodination of acetone is described below.

$$CH_3COCH_3 + 2I_2 \leftrightarrow ICH_2COCH_2I + 2I^- + 2H^+$$

The zeta potential of each component after iodination is listed in Table 3.1. We can see that the proton adsorption successfully tunes the surface charge of the components so that they have almost similar zeta potentials.

Sample	**ζ (mV)**
Nickle cobaltite	+13.5
rGO	+15.1
PANI	+16.1

Table 3.1. Zeta potential of each component in EPD solution after iodination of acetone.

Figure 3.6 shows the measured deposition mass at different applied potentials as a function of time. Before this deposition, the suspension was sonicated for 2 h since it is known that the quality of the EPD coating is very sensitive to the suspension conditions.[89,93] With this EPD bath preparation, we could successfully make deposition on different substrates and different morphologies confirming the versatility and flexibility of the EPD process (Figure 3.7).

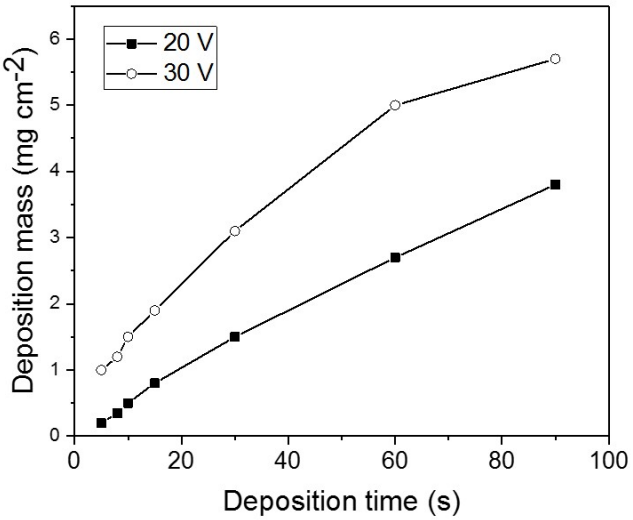

Figure 3.6. Deposition mass on nickel foam against time at different potentials for $NiCo_2O_4$/PANI/rGO suspension with a mass ratio of 10:1:1.

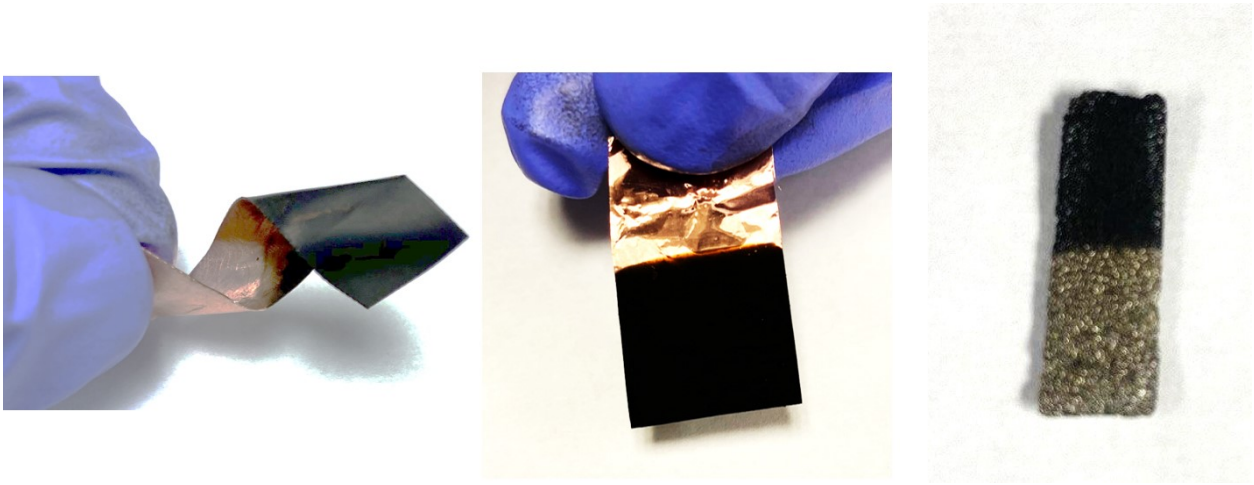

Figure 3.7. Optical images of NCO composite electrodes prepared using different morphologies and substrates showing EPD versatility

For the nickel foam substrate, with the same concentration and mass ratio of components in the suspension, higher voltage leads to faster deposition, as expected. At high EPD voltage and

longer deposition time, we see deviations from the linearity predicted by Hamaker's law. Increased thickness of deposited materials changes substrate condition, and suspension condition may change over time.[92,93] It is also worth mentioning that depositions at potentials higher than 30 V resulted in weak adhesion to the substrate so that we could not assemble the full cell. As long as we stay within the voltage window that is used in the electrode fabrication, the deposited component mass ratio is close to the mass ratio in the EPD bath (Figure 3.8). For the samples that were electrochemically characterized, electrophoretic deposition lasted only for 15 seconds, resulting in a homogenous coating.

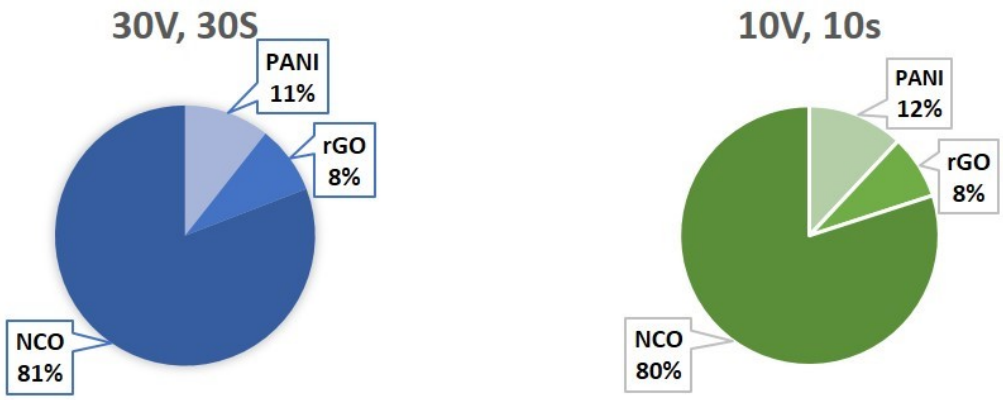

Figure 3.8. Mass ratio determination of $NiCo_2O_4$ (NCO), PANI, and rGO deposited on Ni foam at different EPD conditions

After EPD, the as-prepared composite electrodes were dried and subsequently annealed at 400 °C with a heating ramp of 5 °C min^{-1} for 2 h under nitrogen flow at 30 sccm. During the annealing process, the iodine from the EPD process was removed. PANI was partially carbonized at the same time, hence, improving the conductivity of the polymer. Adhesion of the composite to the underlying substrate was also improved after annealing, showing remarkable flexibility after bending even at 45° where no cracks seemed to appear on the deposited layer (Figure 3.9).

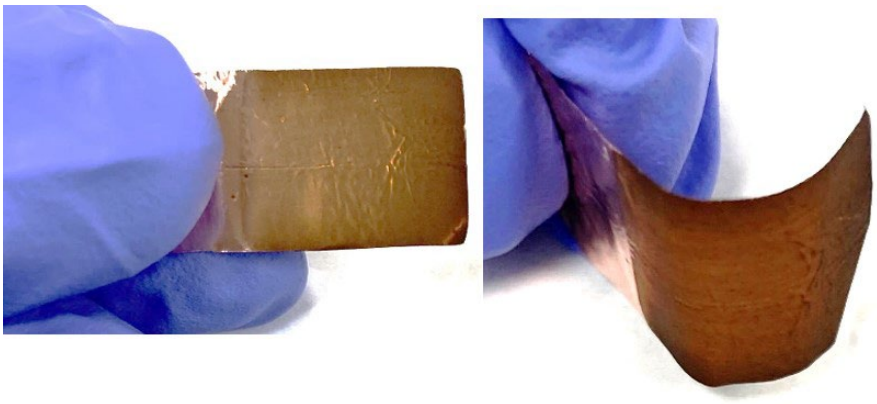

Figure 3.9. As-prepared $NiCo_2O_4$ composite on Cu foil, showing the flexibility of final electrode even after bending 45°

The partial carbonization of PANI was investigated by thermogravimetry (TGA), Raman spectroscopy, and XPS. TGA thermogram in nitrogen environment reveals two stages of weight loss (Figure 3.10a). The initial weight loss below 100 °C can be attributed to the removal of chemisorbed and occluded water. The major weight loss starting at 300 °C is due to the carbonization of PANI. As it is shown in Figure 3.10b, C-PANI, carbonized polyaniline, has around 15% less mass than the original due to carbonization during the annealing process.

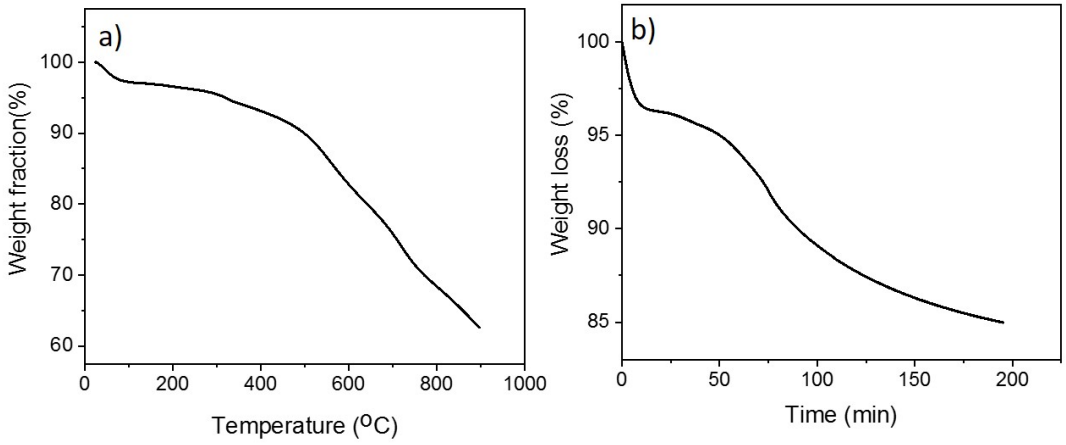

Figure 3.10. Weight change of PANI in N_2. a) Weight change from 25 °C up to 900 °C with a heating ramp of 10 °C min^{-1}. b) Weight change during heating plus holding at 400 °C for 2 h.

Furthermore, Raman spectroscopy was performed to study the structural evolution of PANI after heat treatment. As Figure 3.11 illustrates, the intensity of the peaks at 1630, 1416, 1335, and 530 cm^{-1} which are associated with phenazine or crosslinked units are increased and shifted from 1596 to 1586 cm^{-1} and 1416 to 1408 cm^{-1} which is in agreement with literature.[112]

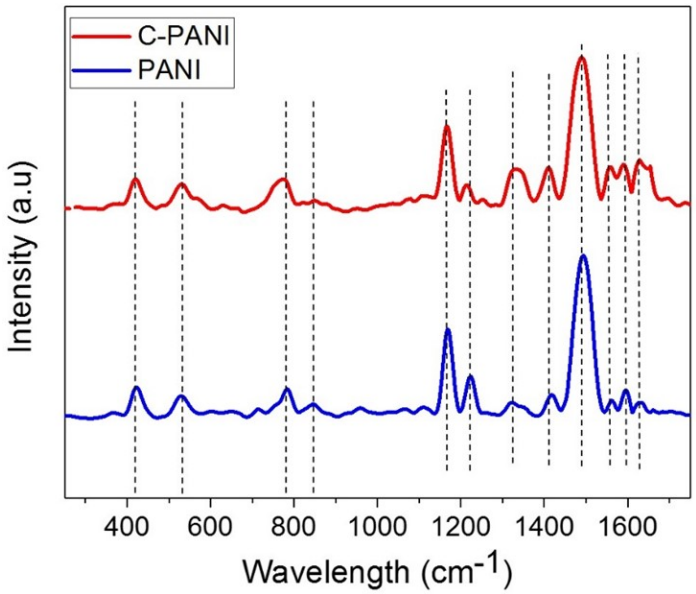

Figure 3.11. Raman spectra comparison of C-PANI vs PANI.

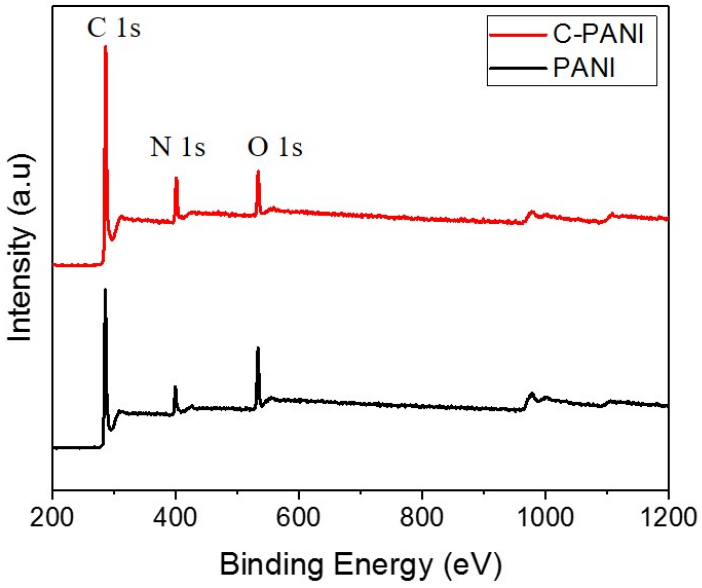

Figure 3.12. XPS survey spectrum of PANI and C-PANI.

To investigate the elemental composition change of C-PANI, XPS measurements were carried out on PANI and C- PANI. The XPS survey spectra of both samples confirmed the presence of C (284.7 eV), O (398.9 eV), and N (532.9 eV) (Figure 3.12). As can be seen in Table 2, the oxygen content of C-PANI is decreased while the carbon and nitrogen contents are increased after partial carbonization.

Elemental % / Sample	**PANI**	**C-PANI**
C	79	82
O	13.1	7.9
N	7.7	10.4

Table 3.2. Elemental analysis of PANI and C-PANI.

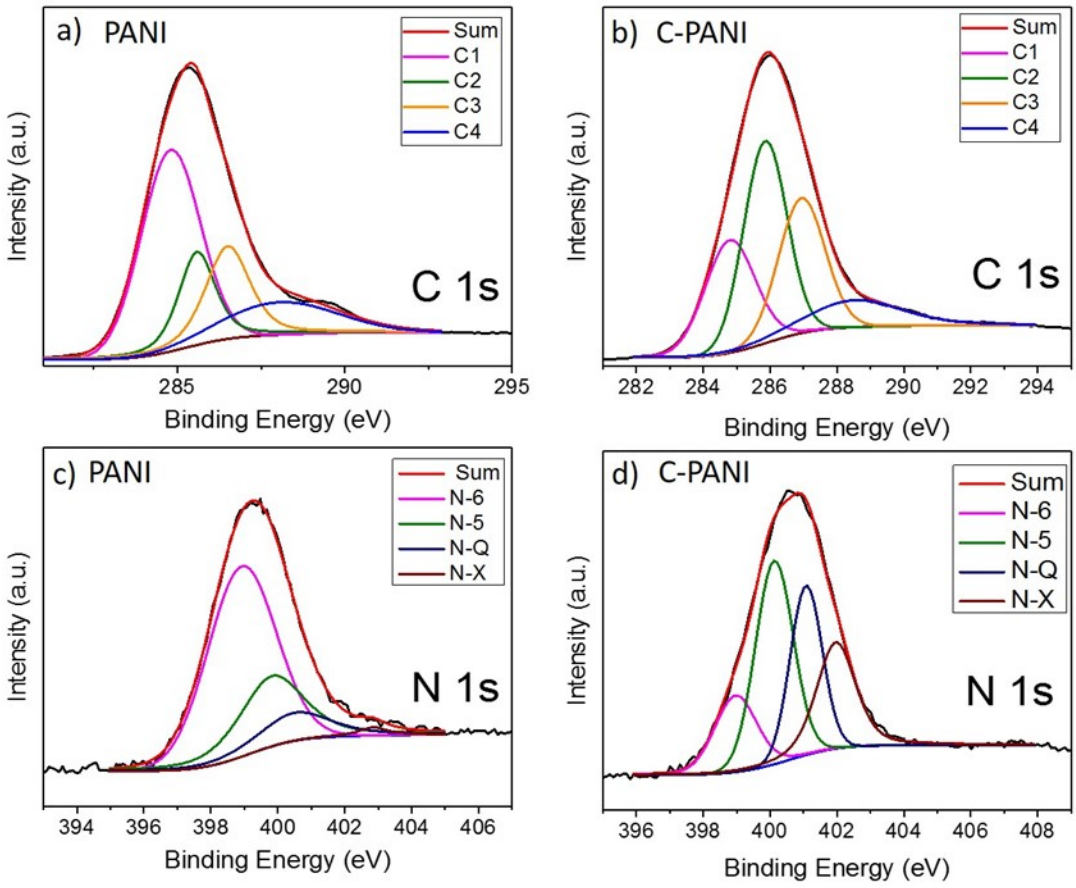

Figure 3.13. a-b) C 1s spectra of PANI and C-PANI. c-d) N 1s spectra of PANI and C-PANI.

The C 1s spectra of PANI and C-PANI (Figure 3.13a, b) show four distinct component peaks at 248.8, 285.6, 286.6, and 288.1 eV representing C-C/C=C, C-N, C-O, and C=O.[116,117] As it can be seen, the graphitic carbon content of C-PANI has increased considerably. The O 1s spectra of PANI and C-PANI consist of peaks at binding energies of 530.5 eV (for PANI) and 530.7 eV (for C-PANI) that belongs to C=O groups, 532.1 eV (for PANI) 532.1 eV (for C-PANI) responding to C-OH/C-O-C groups and 533.5 eV which is for chemisorbed water and/or oxygen (Figure SI 6).[118]

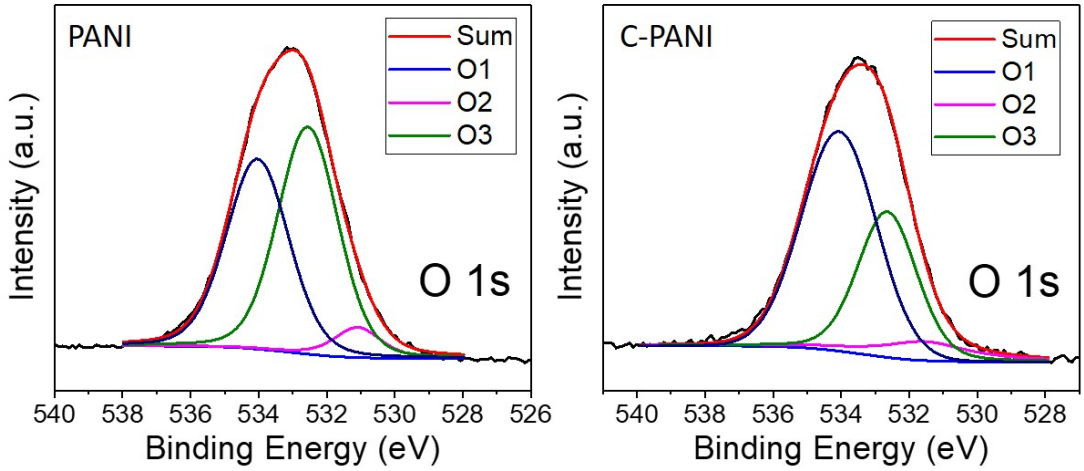

Figure 3.14. XPS O1s spectrum of a) PANI and b) C-PANI

Furthermore, the deconvolution of N1s spectra for both PANI and C-PANI revealed the presence of four distinct nitrogen configurations (Table 3.3) and both PANI and C-PANI contained pyridinic nitrogen (N-6), pyrrolic nitrogen (N-5), quaternary nitrogen (N-Q), and pyridine nitrogen oxide (N-X). It is obvious that the pyridinic nitrogen (N-6) content is decreased during carbonization while pyrrolic nitrogen (N-5), quaternary nitrogen (N-Q), and pyridinic nitrogen-oxide (N-X) content are increased. N-Q and N-X groups are reported to improve charge transfer due to their positive charge.[119]

PANI

Species	BE	%
Pyridinic Nitrogen N-6	398.9	60.6
Pyrrolic Nitrogen/Pyridone Nitrogen N-5	400.3	26
Quaternary Nitrogen N-Q	400.8	11.8

Pyridine-N-oxide N-X	402.9	1.6

C-PANI

Species	BE	%
Pyridinic Nitrogen N-6	398.9	15.8
Pyrrolic Nitrogen/Pyridone Nitrogen N-5	400.1	36.3
Quaternary Nitrogen N-Q	401.1	25.3
Pyridine-N-oxide N-X	402.9	22.6

Table 3.3. XPS N 1s survey deconvolution for PANI and C-PANI

3.4.3 $NiCo_2O_4$/C-PANI/rGO electrode characterization

Samples were deposited on both Ni foam and copper foil for SEM characterization. As can be seen in Figure 10a, the SEM image of neat nickel cobaltite powder shows hexagonal platelets with ca. 200 nm and a thickness of about 40 nm. Figure 3.15b shows $NiCo_2O_4$-only electrode fabricated by EPD. As it can be seen, a homogenous film of densely packed $NiCo_2O_4$ platelets is formed after deposition and heating under nitrogen. Figure 3.15c shows $NiCo_2O_4$/C-PANI/rGO composite with $NiCo_2O_4$ platelets dispersed homogeneously and anchored into the C-PANI/rGO network. The existence of a large number of voids formed in this hybrid film provides buffer space for volume expansion of material during cycling. They could also act as reservoirs for the electrolyte. A closer look, Figure 3.15d, shows $NiCo_2O_4$ platelets wrapped by rGO sheets and distributed in C-PANI/rGO network. This confirms the role of the rGO/C-PANI matrix in mitigating aggregation of $NiCo_2O_4$ platelets effectively and providing a conductive network.

Furthermore, the cross-sectional image of a deposited composite layer (Figure 3.15e) shows a thickness of ~ 1.2 µm for the 15-second electrophoretic deposition. The bright surface in the upper right was originally in contact with the copper foil. The electrode layer was mechanically detached from the copper substrate to get the cross-sectional view. Figure 3.15f and Figure 3.16 show the successful deposition of $NiCo_2O_4$/C-PANI/rGO composite on Ni foam, proving the versatility of EPD to be applicable on different substrates. For all electrochemical characterization, Ni foam was the chosen substrate.

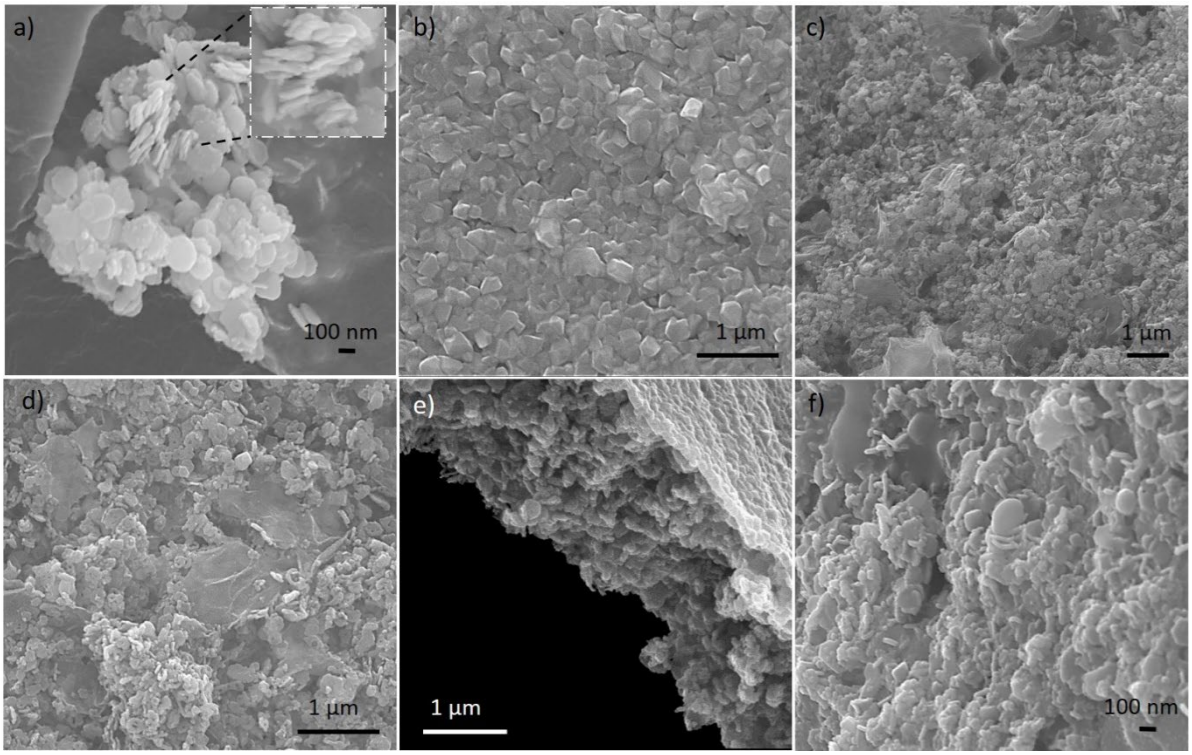

Figure 3.15. SEM images of a) top view of $NiCo_2O_4$ platelets (Inset: zoomed-in view of $NiCo_2O_4$ platelets) simply put on a carbon tape, b) $NiCo_2O_4$-only electrode on deposited on copper foil. c, d) Top-down view and e) cross-sectional view of $NiCo_2O_4$/C-PANI/rGO composite electrode deposited on copper foil. f) $NiCo_2O_4$/C-PANI/rGO composite electrode on Ni foam.

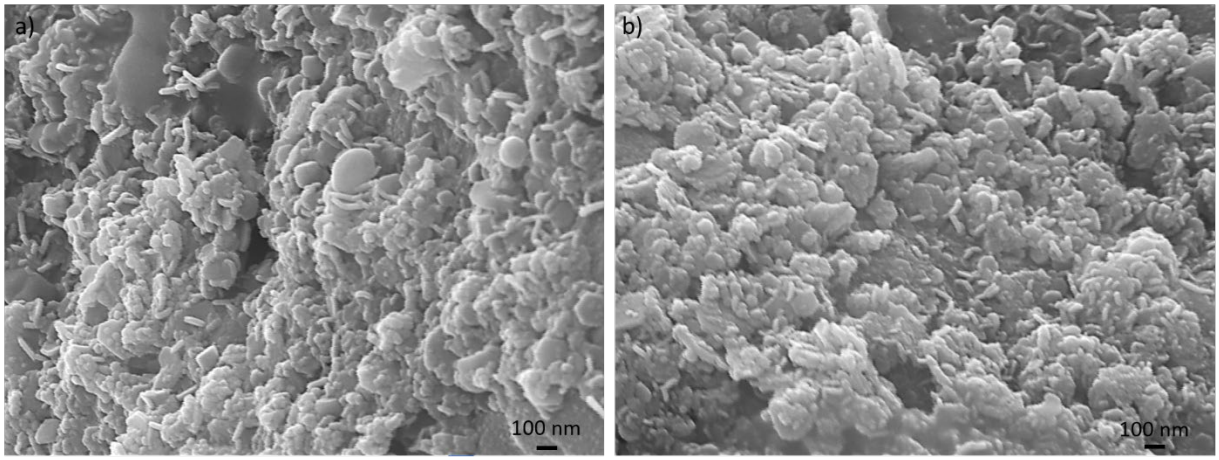

Figure 3.16. Additional top-view SEM image $NiCo_2O_4$/C-PANI/rGO composite electrode deposited on Ni foam

To confirm the co-existence of all components in the composite, Raman spectroscopy, as well as FTIR, was conducted on the as-prepared $NiCo_2O_4$/C-PANI/rGO samples. The corresponding Raman peaks of $NiCo_2O_4$/C-PANI/rGO hybrid electrode (Figure 3.16a) shows matches with Raman spectra of $NiCo_2O_4$ (532 and 685 cm^{-1}), C-PANI (414, 532, 767, 843, 1170, 1231, 1413, 1498, and 1587 cm^{-1}) and rGO (1354 and 1587 cm^{-1}). It should be noted that some of the characteristic peaks of C-PANI are merged with $NiCo_2O_4$ and rGO. The Raman peaks of the hybrid electrode also show a small shift in comparison to the Raman spectra of each separate component, which could also be due to the composite formation and change in the chemical bond length of the molecules.[120,121] Figure 3.16b shows the FTIR peaks for $NiCo_2O_4$/C-PANI/rGO composite. It can be seen that some new peaks have emerged as a result of merging of characterizing peaks of $NiCo_2O_4$/C-PANI (661 and 704 cm^{-1}), C-PANI/rGO (830, 1005, and 1393 cm^{-1}) while on the other hand characteristic peaks of C-PANI (2937 cm^{-1}) and rGO (1626 and 3380 cm^{-1}) are also observed with minor shifts in comparison to the initial FTIR spectra of the similar materials. This shift is due to a change in the bonding length of the compounds, which could be a result of composite formation.

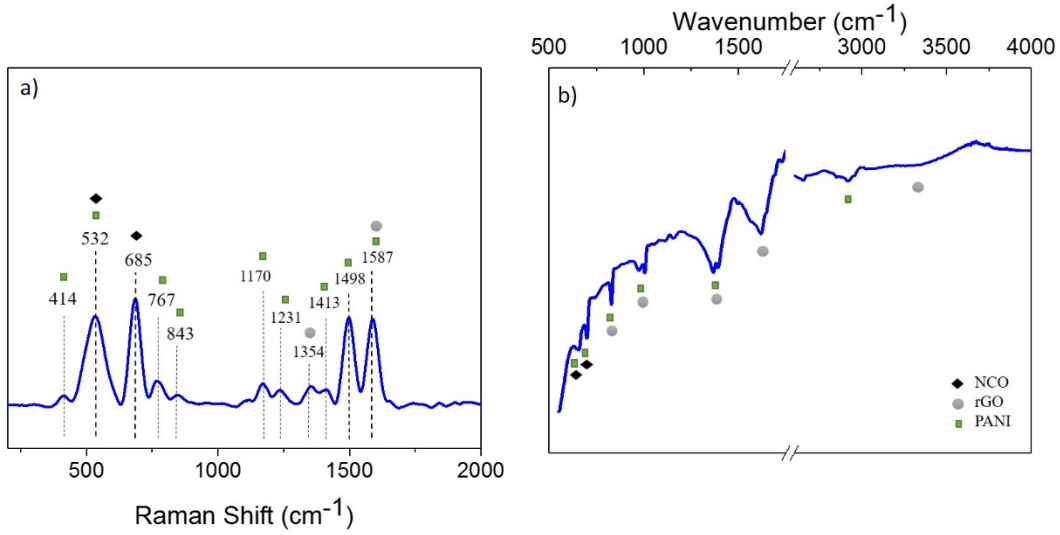

Figure 3.17. a) Raman spectra and b) FTIR spectra of $NiCo_2O_4$/C-PANI/rGO composite electrode

3.4.4 Three-electrode cell electrochemical performance

Cyclic voltammetry and galvanostatic charge/discharge techniques were employed to understand the electrochemical behavior of $NiCo_2O_4$/C-PANI/rGO electrodes. Two-component electrodes, $NiCo_2O_4$/rGO and $NiCo_2O_4$/C-PANI, and one-component electrode, $NiCo_2O_4$, were also tested to further understand the electrochemical behavior of the EPD-assembled composite. Figure 3.17a shows cyclic voltammetry scans of the four investigated electrodes. For all samples, one anodic peak and one cathodic peak are visible, which correspond to the faradic redox reaction of MO/MOOH (where M stands for Ni or Co). Bare nickel foam delivers a much smaller current in comparison to as-prepared electrodes, indicating it has negligible contribution in capacitance. The larger enclosed area in CV trace for the ternary composite, $NiCo_2O_4$/C-PANI/rGO electrode, indicates its superior charge storage over binary composites. Moreover, $NiCo_2O_4$/C-PANI/rGO CV traces in Figure 3.17b collected at different scan rates (2 ~ 250 mV s^{-1}) imply fast reaction kinetics of $NiCo_2O_4$/C-PANI/rGO. The faradic redox peaks are observable even at a scan rate of

250 mV s^{-1}. Increasing scan rate tends to shift anodic and cathodic peaks to higher and lower potentials indicating the quasi-reversible nature of redox couple.[122,123] The current measured from the CV curve can further be decomposed to diffusion-controlled (i_{diff}) and surface-controlled (capacitive) charge storage (i_{cap}). A well-known equation is often used to determine the charge storage mechanism involved in the system by establishing a relationship between current (i) and scan rate (ν):

$$i(\nu) = i_{diff} + i_{cap} = a\nu^{b} \quad (32)$$

$$\log i = \log a + b \log \nu \quad (33)$$

where a and b are constants. b can be obtained from the slope in the log ν versus log i plot. When b = 0.5, the electrochemical response is dominated by a diffusion-controlled process whereas the surface reaction-controlled process is denoted by b value close to 1.[30,75] Our result from anode peak current density shows b=0.65 for $NiCo_2O_4$/C-PANI/rGO (Figure 17d), suggesting a mixed surface-controlled and diffusion-controlled nature of the charge storage process.

Galvanostatic charge/discharge (GCD) tests were conducted to study the charge/discharge behavior of different electrodes. Figure 17c presents discharge curves for different electrodes at a current density of 10 A g^{-1} with a potential window, ranging from 0 to 0.5 V. During the discharge, the ternary composite maintains higher electric potential than other samples showing the highest power density. The $NiCo_2O_4$/C-PANI/rGO electrode also shows the smallest IR drop (deviation from 0.5 V as the initial discharge voltage), meaning it has the smallest series resistances. C-PANI/rGO network effectively decreases the ionic transport resistance by providing a porous scaffold with easy access to the electrolyte. The wider voltage plateau of $NiCo_2O_4$/C-PANI/rGO

also indicates that C-PANI/rGO network prevents agglomeration of metal oxide platelets exposing more redox-active sites to the electrolyte.

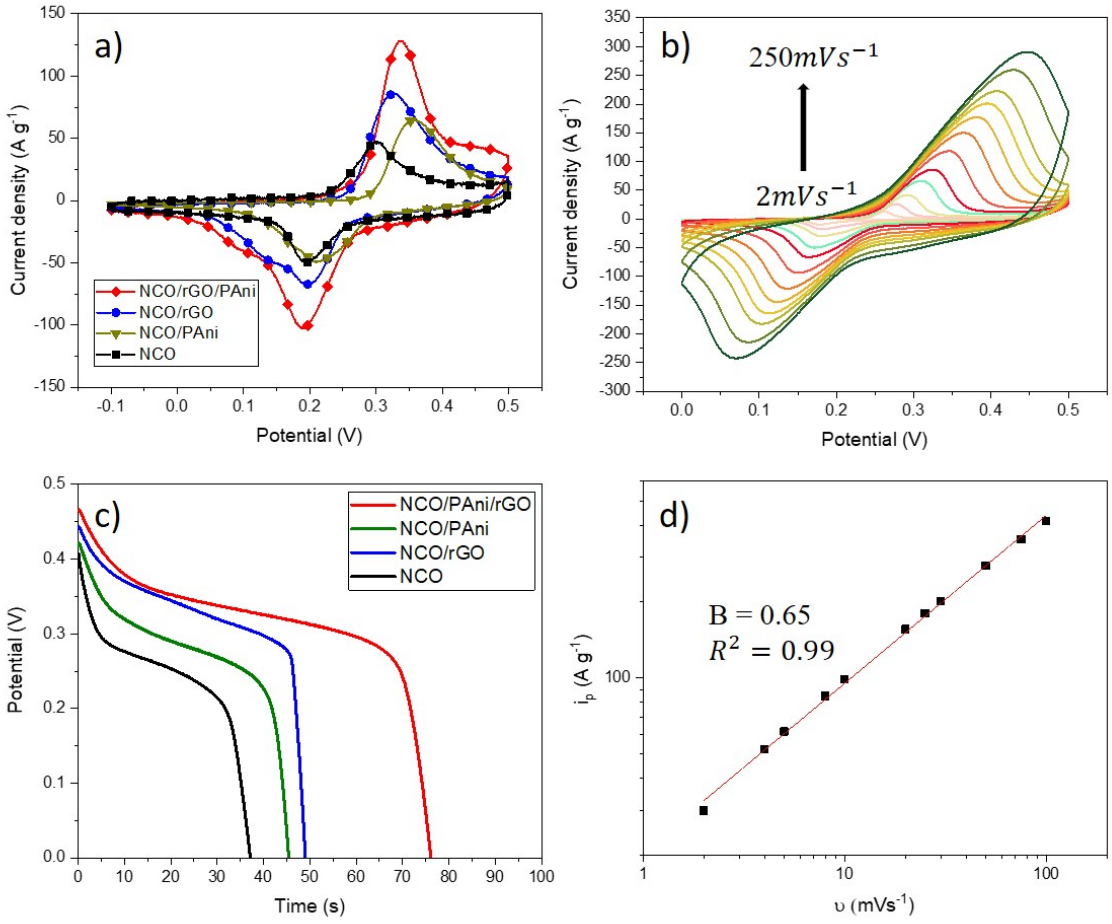

Figure 3.18. a) CV of different electrodes using a scan rate of 50 mV s^{-1}. b) $NiCo_2O_4$/C-PANI/rGO CV responses at different scan rates ranging from 2 to 250 mV s^{-1}. c) Discharge curves of different electrodes at 10 A g^{-1}. d) Peak current density vs. scan rate for the anodic peak at scan rates ranging from 2 to 100 mV s^{-1}

Moving to higher current densities, $NiCo_2O_4$/C-PANI/rGO electrode maintains remarkable performance as illustrated in Figure 3.18a. The enhanced charge transport and ion transport comes from the effective distribution of redox-active nickel cobaltite on the C-PANI/rGO conductive network. Figure 3.18b shows the specific capacitance of each as-prepared electrode ($NiCo_2O_4$,

$NiCo_2O_4$/C-PANI, $NiCo_2O_4$/rGO, and $NiCo_2O_4$/C-PANI/rGO) at different current densities. $NiCo_2O_4$ electrode showed a specific capacitance of 903 F g^{-1} at 1 A g^{-1} and could reach a current density of as high as 50 A g^{-1}. The increase in specific capacitance and working current density range for hybrid electrodes ($NiCo_2O_4$/C-PANI, $NiCo_2O_4$/rGO, and $NiCo_2O_4$/C-PANI/rGO) confirms the merit of composite formation. $NiCo_2O_4$/C-PANI/rGO electrode showed superior performance over binary composite electrodes with a significant capacitance of 1235 F g^{-1} at 60 A g^{-1} meaning most of the active sites of nickel cobaltite particles are effectively in contact with the electrolyte and undergo redox reaction even at very high current densities despite that the nickel cobaltite mass loading is less than the single component nickel cobaltite electrode. This could only be explained by the desirable structure of C-PANI/rGO, which provides a porous yet conductive matrix for the distribution of nickel cobaltite platelets.

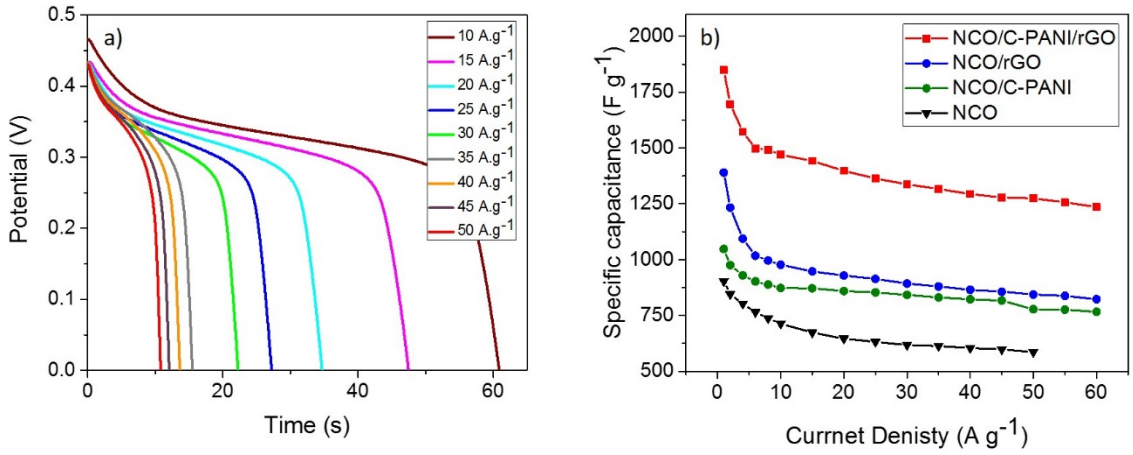

Figure 3.19. a) $NiCo_2O_4$/C-PANI/rGO discharge curves at current densities ranging from 10 to 50 A g^{-1}. b) Specific capacitance of different as-prepared electrodes at different current densities

The cycling stability of $NiCo_2O_4$ and $NiCo_2O_4$/C-PANI/rGO electrodes were also tested by employing a continuous charge/discharge cycling at 10 A g^{-1} (Figure 3.19a). For the $NiCo_2O_4$ electrode, the specific capacitance slightly increased (around 15%) during the test. $NiCo_2O_4$/C-

PANI/rGO electrode shows a more sophisticated behavior. In the end, the ternary composite maintained 80% of the initial capacitance after 3000 cycles. The limited stability of polyaniline in the base media may impact the stability of the overall electrode causing long-term capacitance loss. GCD curve of $NiCo_2O_4$/C-PANI/rGO electrode at 10 A g^{-1} after 3k showed a narrower potential plateau while IR drop change was negligible (Figure 3.19b).

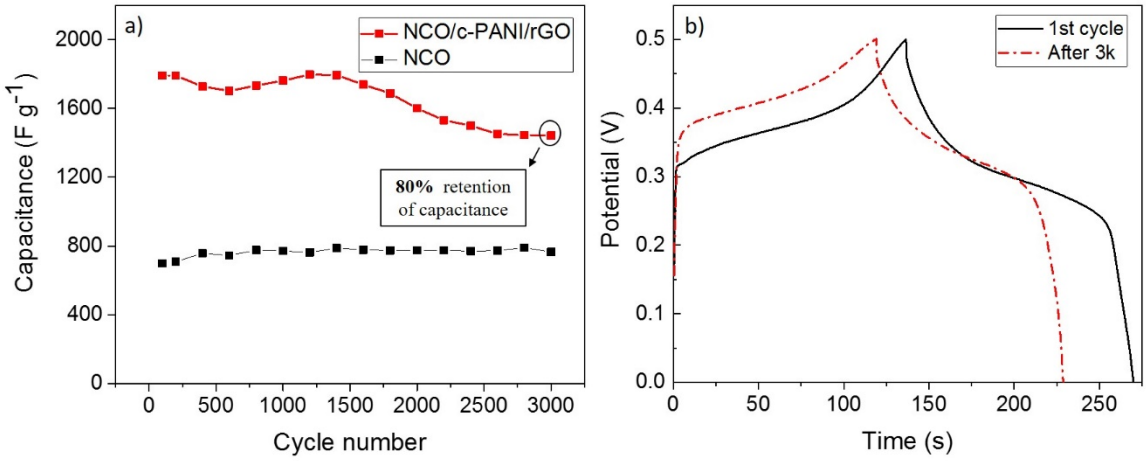

Figure 3.20. a) Cyclic stability of $NiCo_2O_4$ and $NiCo_2O_4$/C-PANI/rGO electrodes at 10 A g^{-1} for 3000^{th} cycles. b) GCD curves of $NiCo_2O_4$/C-PANI/rGO electrode after 1^{st} and 3000^{th} cycles

3.4.5 All-solid asymmetric supercapacitor performance

To investigate the practical application of $NiCo_2O_4$/C-PANI/rGO composite, an all-solid-state asymmetric supercapacitor was fabricated by incorporating $NiCo_2O_4$/C-PANI/rGO as the cathode and activated carbon (AC) as the anode. PVA/KOH (PVA, polyvinyl alcohol) film was used as the all-solid-state electrolyte. The CV curves at different potential ranges collected for this asymmetric cell suggested a stable potential window of 1.6 V (Figure 3.20).

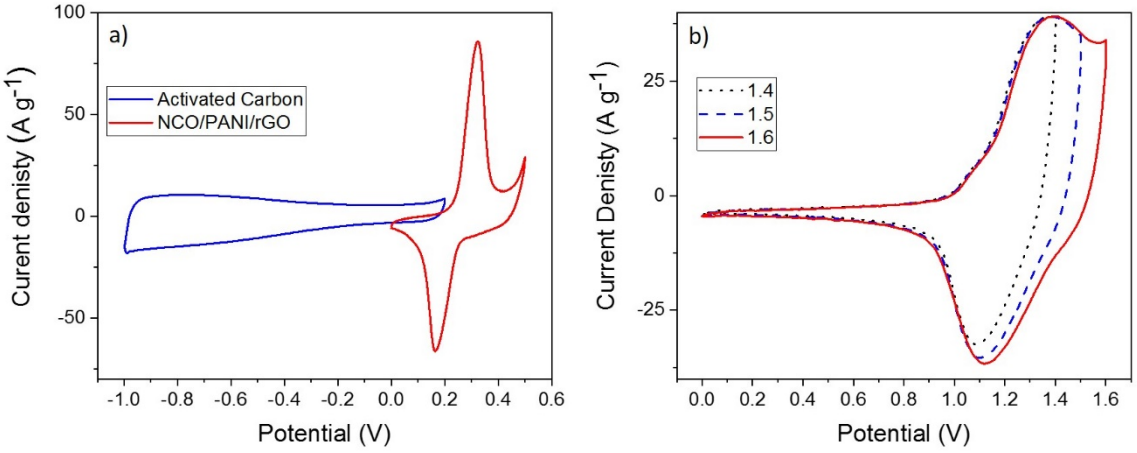

Figure 3.21. a) CV curves of AC and NCO/PANI/rGO electrodes at 20 mV s^{-1}b) CV curves of NCO/PANI/rGO//AC ASC at different potential windows at 20 mV s^{-1}

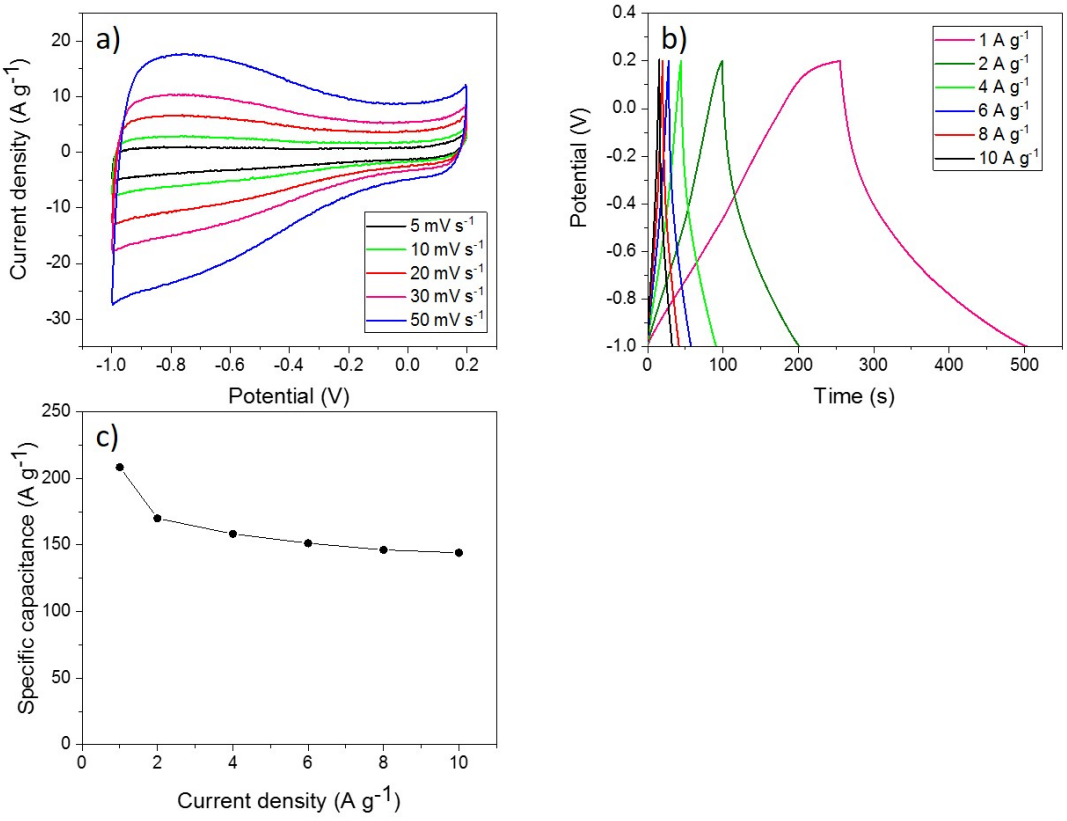

Figure 3.22. a) CV curves of AC at different scan rates b) Charge-discharge curves of AC at different current densities c) specific capacitance of AC at different current densities

Scan rates from 5 to 150 mV s^{-1} were used for CV scans. Figure 3.22b demonstrates excellent rate capability even at a scan rate as high as 150 mV s^{-1}. Charge-discharge curves in Figure 3.22c show a small IR drop within the working potential window. The specific capacitance of the overall cell at different current densities is shown in Figure 3.22d, showing acceptable performance with a specific capacitance of 262.5 F g^{-1} at 1 A g^{-1} and around 60% of the initial capacitance at 20 A g^{-1}. The durability is an essential factor for the practical application of supercapacitors. The asymmetric cell showed a durable cycling life with 78% capacitance retention after 3500 cycles at a current density of 5 A g^{-1}. The initial capacitance increase during the first 100 cycles from 216 F g^{-1} to 259 F g^{-1} could be due to the improved ion accessibility in the electrodes after repetitive cycling.[124]

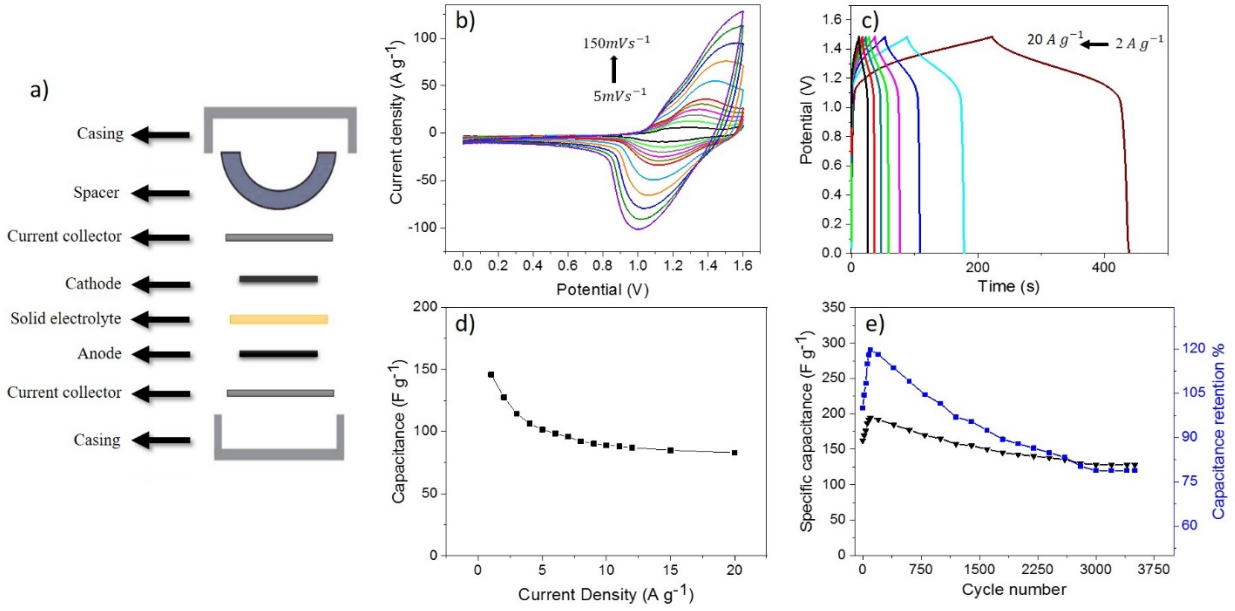

Figure 3.23. Electrochemical characterization of a $NiCo_2O_4$/C-PANI/rGO//AC asymmetric cell: a) Schematic of all-solid-state coin cell assembly, b) CV responses at different scan rates ranging from 5 to 150 mV s^{-1}, c) Charge-discharge curves at different current densities from 2 to 20 A g^{-1}, d) Corresponding specific capacitance at different current densities, e) Cyclic stability of the cell at a current density of 5 A g^{-1} for 3500 cycles.

Figure 3.23 represents the Ragone plot of reported asymmetric cells along with the current one. The EPD assembled cell reaches a maximum energy density of 45.6 Wh kg^{-1} with a power density of 610.1 W kg^{-1} while still keeping an energy density of 28.2 Wh kg^{-1} at a power density of 12.8 kW kg^{-1}. This result shows improved energy density at high power density comparing with $Ni_xCo_{3-x}O_4$ nanowire (20.7 Wh kg^{-1} at 4.1 kW kg^{-1})[125], Ni-Co oxide asymmetric device (5.7 Wh kg^{-1} at 1.90 kW kg^{-1})[126], $NiCo_2O_4$ NP (54.4 Wh kg^{-1} at 654 W kg^{-1})[127] and $NiCo_2O_4$–RGO (31 Wh kg^{-1} at a maximum power density of 15 kW kg^{-1})[87].

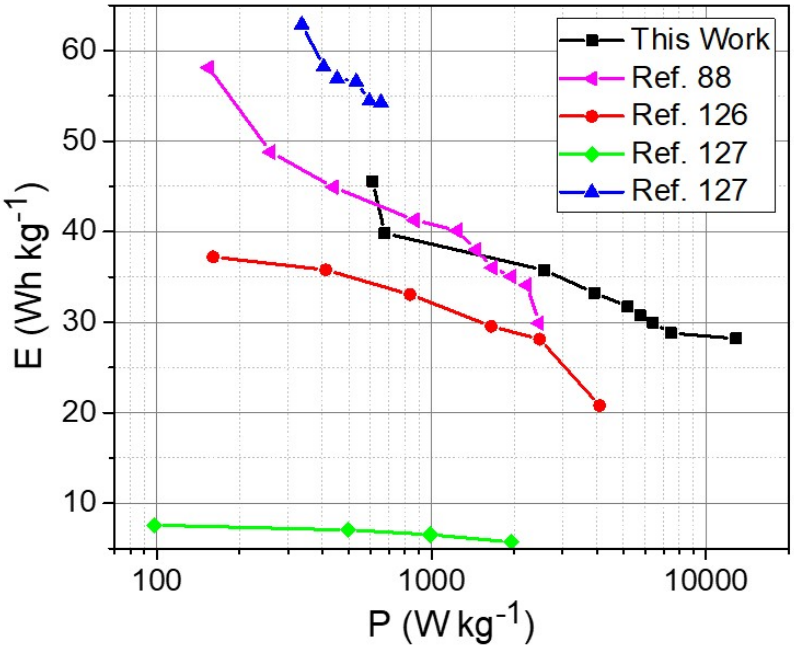

Figure 3.24. Ragone plot of the asymmetric cells. They all have activated carbon anodes.

3.6 Conclusion

$NiCo_2O_4$-based composite electrodes were fabricated on nickel foam substrates using 15-second electrophoretic deposition followed by heat treatment. The $NiCo_2O_4$ platelets were

effectively distributed on the C-PANI/rGO network that prevents $NiCo_2O_4$ agglomeration yet connects the individual platelets electrically. The composite formation resulted in better utilization of the nickel cobaltite platelets for charge storage. The as-prepared composite electrodes showed good rate capability (up to 60 A g^{-1}) as well as acceptable cycling stability (80% capacitance retention after 3000 cycles). The practical application of the composite electrode was investigated by fabrication of coin cell all-solid asymmetric supercapacitor operating at a voltage of 1.5 V using $NiCo_2O_4$/C-PANI/rGO as the cathode and activated carbon as anode and PVA/KOH gel as the solid electrolyte. The device showed a maximum energy density of 80 Wh kg^{-1} and a maximum power density of 47 Wh kg^{-1} with good cycling stability (78% after 3500 cycles). The scalable EPD route taken in this work is a facile composite formation scheme that can be applied to many different electrode component materials.

3.7 Acknowledgements

This work was supported by Auburn University start-up fund. We thank Mingyang Chi and Dr. Bruce Tatarchuk for the help with the XPS analysis. We also thank Dr. Rohit Kanungo for the help in rGO synthesis and Dr. Kim and Mr. Doohee Lee for providing access to DC power supply.

Chapter 4. Developing MOF-based nickel cobaltite with tunable structural properties for supercapacitor applications

4.1 Abstract

Highly porous $Co_3O_4/NiCo_2O_4$ nanostructures were synthesized using from zeolitic imidazolate framework-67 (ZIF-67) nanocrystals. The strategy includes the synthesis of zeolite imidazolate framework-67(ZIF-67)/Ni-Co layered doubled hydroxide (LDH) templates and subsequent transformation to $NiCo_2O_4(Co_3O_4)$ by thermal annealing. $NiCo_2O_4(Co_3O_4)$ nanostructures showed capacitance of 770 $F.g^{-1}$ at a discharge current density of 1 $A.g^{-1}$ and good stability, holding 68% of the initial capacitance after 10000 cycles of charge-discharge.

This work shows a universal process for the controlled synthesis of different complex spinel structures that can be used for various applications.

4.2 Introduction

Advance energy storage devices are required for different technological demands. From powering up hybrid/electric vehicles and portable electronic devices to storing energy from reproducible sources such as wind and sun as they are erratic and cannot be controlled. The demand for electrochemical energy storage devices is rapidly increasing for storage and delivery of electrical energy, providing greater flexibility and stability to address the increasing demand for high-performance electric devices.[5,128–131]

Batteries and capacitors are two major types of energy storage devices that are extensively used and yet both face limitations. Batteries can deliver energy at a limited rate over an extended time and are suitable for different applications ranging from powering electronics to mobility and

grid storage but they are limited by power density and lifetime due to their charge-storage mechanism, which involves phase transformation of active materials bulk during ion-diffusion. On the other hand, capacitors have high power density energy density, suitable for high-performance systems yet their energy density is too low to power systems that require high energy amounts like future electric vehicles. Supercapacitors tend to close the gap between batteries and capacitors by providing high power density, comparable to capacitors and high energy density, comparable to batteries, and are considered the next generation of electrochemical energy storage devices.[5,41,52]

Transition metal oxides are a group of materials that have been extensively studied for supercapacitor applications. The charge storage behavior of these materials heavily depends upon their structural properties and electrolyte. Spinel oxides share a common structure but exhibit very different behavior based on the transition metal(s) involved.[87,132,133] Among spinel materials, Co_3O_4[134] and $NiCo_2O_4$[63,135] exhibit battery-type behavior due to the formation of oxyhydroxides during the charge storage process. $NiCo_2O_4$ shows a much higher conductivity than Co_3O_4 and has been perceived as a promising candidate for high-performance supercapacitors with a high theoretical capacitance (2005 $F.g^{-1}$), easy preparation as well as abundant resources.[52]

The challenge with traditional battery-like materials such as spinel oxides is not only to achieve a high specific capacitance at a short timescale but also to overcome the kinetic limits that occur due to phase transformations. The electrochemical behavior of these materials depends on the particle size and structural characteristics of the electrode material and optimization of these materials on the nanoscale is a promising direction for increasing their rate performance as their battery-type behavior becomes increasingly pseudocapacitive with decreasing the crystal size as the capacity from diffusion into the inner layers is decreased gradually and the capacity from the surface active sites become more dominant with decreasing crystallite size.[30,136,137] Therefore, it is

essential to develop methods to produce high-performance electrode materials with proper structural characteristics to expose as much of the materials' surface to the electrolyte as possible.

Metal-organic frameworks (MOFs) also known as porous coordination polymers (PCPs) are a class of multipurpose materials with highly porous, crystalline structures that are a result of metal ions and organic ligands coupling through coordination bonding. MOFs offer form one-, two-, or three-dimensional structures[138–140] with unique properties such as high surface area as well as a high level of tunable porosity that has attracted considerable attention for applications such as catalysis, gas storage, and energy conversion.[141–144] Because of their structural properties, MOFs have also been studied as ideal sacrificial templates for porous carbons and metal compounds that can be used in energy storage applications. [145–147] The zeolitic imidazolate frameworks (ZIFs) are a class of MOFs that show high thermal and chemical stability.[148,149]

A novel approach to control the size and shape of MOF structures is the coordination modulation method in which an auxiliary monodentate ligand competes with the multidentate bridging ligand at metal centers that are exposed on the surface of the forming MOF crystal. The monotopic modulating ligands mimic the functionality of the multitopic MOF linkers and induce different mechanisms during self-assembly.[150,151] Modulator incorporation throughout the MOF structure further causes modulation-induced defectivity, which makes it possible to tune pore size by controlling the defectivity in MOF structures.[150,152,153] Although defective MOFs are been explored for a wide range of applications, but there have not been any studies about the effect of tuning MOF structure on the structural properties of MOF-derived metal oxide nanostructures and consequently their electrochemical behavior.

Here, we report a novel approach to synthesize highly porous $Co_3O_4/NiCo_2O_4$ nanostructures using ZIF-67 nanocrystals. This strategy involves the coordination modulation

synthesis of zeolitic imidazolate framework-67 using diethylamine as the modulating ligand to form ZIF-67 nanocrystals and later etching the sacrificial template to form ZIF-67/Ni-Co LDH and subsequent thermal annealing This study shows tuning MOF crystal size and structural properties produces ZIF-67 derived $Co_3O_4/NiCo_2O_4$ nanostructures with a capacitance as high as 770 F g^{-1} at 1A g^{-1} while maintaining 84% of initial capacitance at 20 A g^{-1} while $Co_3O_4/NiCo_2O_4$//AC asymmetric supercapacitor exhibited 38.8 Wh kg^{-1} at a power density of 10 kW kg^{-1}.

4.3 Experimental section

4.3.1 Materials: All reagents were of analytical grade and were used without further purification.

4.3.2 Synthesis of ZIF-67 regular-sized crystals: ZIF-67 crystals with a regular size were synthesized by mixing $Co(NO_3)_2 \cdot 6H_2O$ and 2-methylimidazole (Hmim) at different ratios of Co: Hmim. To synthesize ZIF-67 with a 1:4 molar ratio of Co: Hmim, 614.78 mg (2.469 mmol) of cobalt nitrate hexahydrate and 810.6 mg (9.874 mmol) of 2-methylimidazole are each dissolved in 50 mL of MeOH. The solutions are then mixed under stirring with a magnetic bar until they were completely combined. After 24 h, the purple solid is separated from the colloidal dispersion by centrifugation, washed with methanol three times, and dried at 60℃.

4.3.3 Synthesis of ZIF-67 nanocrystals: To synthesize ZIF-67 nanocrystals, 614.78 mg (2.469 mmol) of cobalt nitrate hexahydrate is dissolved in 50 mL of MeOH. A second solution is prepared by dissolving 3.242 g (39.496 mmol) of 2-methylimidazole and 3.088 g (39.496 mmol) diethylamine in 50 mL of MeOH. The solutions are then mixed under stirring with a magnetic bar until they were completely combined. After 24h, the dark blue precipitate is recovered by centrifugation, washed with MeOH three times, and drying at 60℃.

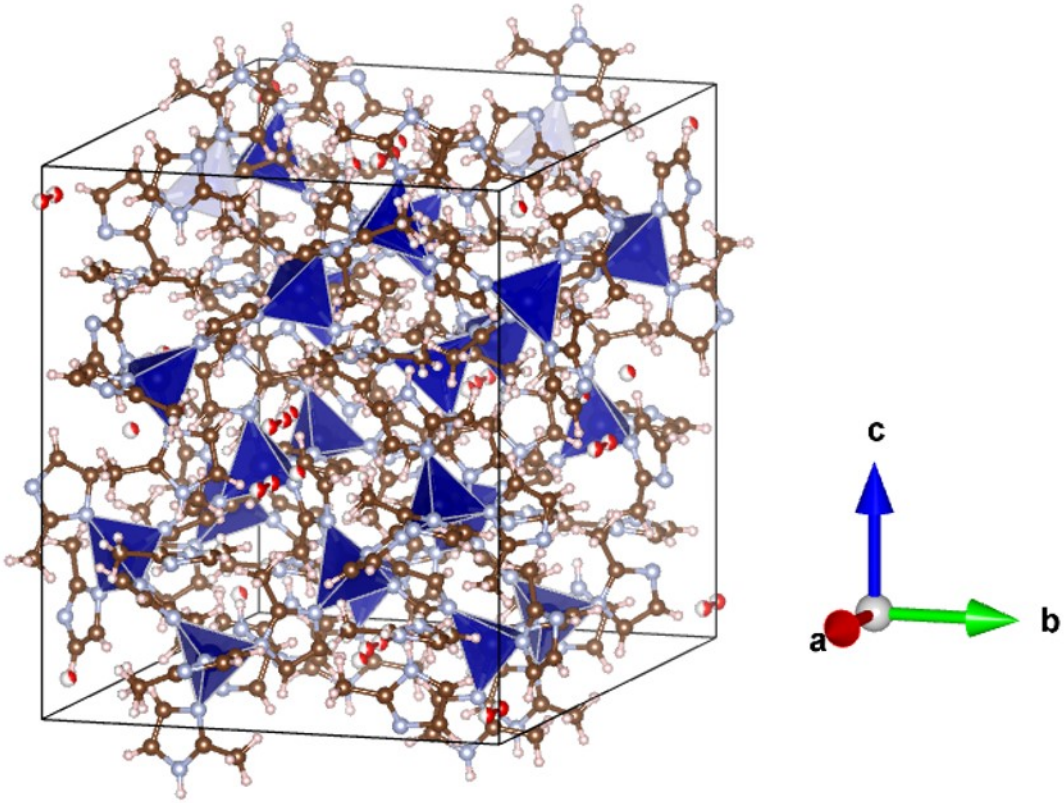

Figure 4.1. Crystal structure of ZIF-67

4.3.4 Synthesis of Co3O4/NiCo2O4: 40 mg of ZIF-67 templates was dispersed in 25 mL of ethanol containing 60 mg of $Ni(NO_3)_2 \cdot 6H_2O$ (2.4 $mg.ml^{-1}$ Ni^{2+}). After stirring for 30 min, the ZIF-67/Ni−Co LDH particles were formed and collected by centrifugation and finally dried at 60 °C for 12 h. As-obtained ZIF-67/Ni−Co LDH particles were then annealed in air at 350°C for 2 h with a ramp rate of 1 °C min^{-1} to obtain $Co_3O_4/NiCo_2O_4$.

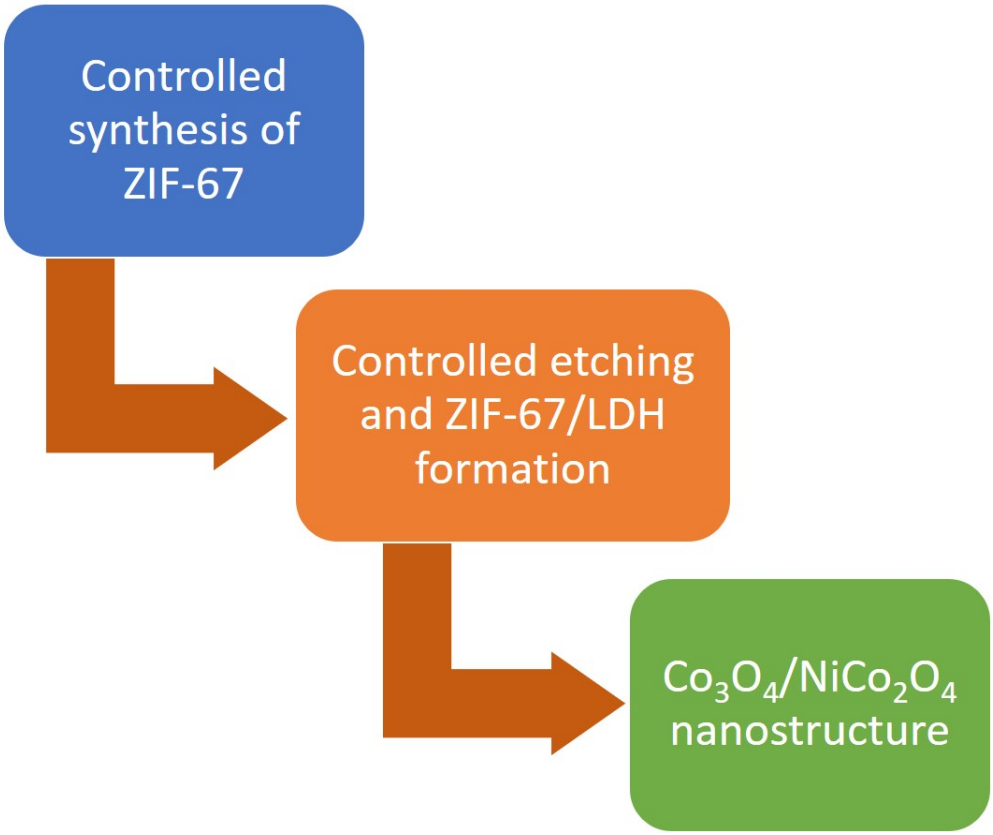

Figure 4.2. The overall process of synthesizing template-based $Co_3O_4/NiCo_2O_4$ nanostructures

4.3.5 Materials characterization: The crystallographic structure of the materials was studied using a PROTO AXRD theta-theta X-ray diffractometer operated using a Cu Kα radiation (40 kV, 30 mA). For crystal size calculations, Scherrer equation was used. This equation can be written as

$$\tau = K\frac{\lambda}{\beta\, cos\theta} \quad (34)$$

For which τ is the crystal size, K is the shape factor with a typical value of 0.9, λ is the wavelength of the X-ray source (1.5406 Å for Cu K_α), β is the broadening at the half of the maximum intensity (FWHM) in radians, and θ is the Brag angle in radians. Firstly, β was calculated using the Gaussian function for at least 5 large peaks (θ) of the pattern, and later after crystal size calculation for each of the angles, the average was reported. JEOL JSM-7000F scanning electron microscope (SEM) and Hitachi H-950 transmission electron microscope was used to observe the morphology

of the as-prepared materials. Elemental mapping was recorded using EDX spectroscopy attached to TEM. Nitrogen adsorption-desorption provided surface area and pore size distribution via Brunauer–Emmett–Teller (BET) method and Barrett–Joyner–Halendar (BJH) method using Quantachrome NOVA 2200e.

4.3.6 Electrochemical characterization: The electrochemical measurements were performed at room temperature with two- and three-electrode assemblies at room temperature using a PARSTAT 4000 potentiostat (Princeton Applied Research). The working electrodes were prepared by mixing the active material, poly(vinylidene difluoride) and carbon black (Super-P conductive) at an 80:10:10 weight ratio in NMP. The resulting slurry was coated over Ni foam and dried at 80 °C overnight in a vacuum oven. The three-electrode cell contained a Pt coil counter electrode, an Ag/AgCl reference electrode, and 6 M KOH electrolyte and the working electrode with a mass loading of ~ 4 mg.cm^{-2}. Potentiostatic EIS studies were performed using 10 mV amplitude with frequencies ranging from 1 Hz to 100 kHz. The specific capacitance (C_s) of a single electrode is calculated in two ways, from the galvanostatic discharge curves by the equation below:

$$C_s = \frac{I \times \Delta t}{(\Delta V) \times m} \quad (35)$$

Where C_s (F.g^{-1}) is the specific capacitance of the electrode, I (A) is the current, Δt (s) is the discharge time, m (g) is the deposited mass on the nickel foam, and ΔV (V) is the working potential window.

And from the CV graphs by using the following equation:

$$C_s = {}^{1}/_{\Delta V} \int_{V_2}^{V_1} j\,dV/\nu \quad (36)$$

where *C* is the specific capacitance (F g^{-1}), *j* is the cathodic current density (mA g^{-1}), V is the voltage (V), ΔV is the voltage window (V), and ν is the scan rate (mV s^{-1}).

For the ASC test, activated carbon (TF-B520, MTI) was used as the anode. The charge (Q) on both the electrodes was balanced by the equation

$$Q = C \times V \times m \quad (37)$$

where C is specific capacitance, V is the operating potential window, and m is the mass of the active electrode material. The total mass of the electrodes was 3 $mg.cm^{-2}$. The energy density (E, $J.kg^{-1}$) and power density (P, $W.kg^{-1}$) of asymmetric supercapacitors are calculated by:

$$E = \frac{1}{2} CV^2, \; P = \frac{E}{\Delta t} \quad (38)$$

where C ($F.g^{-1}$) is the specific capacitance of the asymmetric supercapacitor cell, V (V) is the working potential, and Δt (s) is the discharge time.

4.4 Results and discussion

4.4.1 Materials characterization studies and analysis

Our approach to tune the structure of the template is focused on the size-controlled synthesis of ZIF-67 and controlled etching of the structure to make ZIF-67/LDH templates and further transform them into metal oxide particles. For the first step, ZIF-67 is initially synthesized by mixing Co (II) source with different ratios of bridging ligand, 2-methylimidazole (Hmim), to investigate the effect of metal to ligand ratio on ZIF-67 size and later employing diethylamine as a modulating ligand to further understand the structural modification by modulating ligand incorporation. Once the ligand solution that contained DEA was combined with the cobalt nitrate solution, the nearly instantaneous formation of a solid was observed.

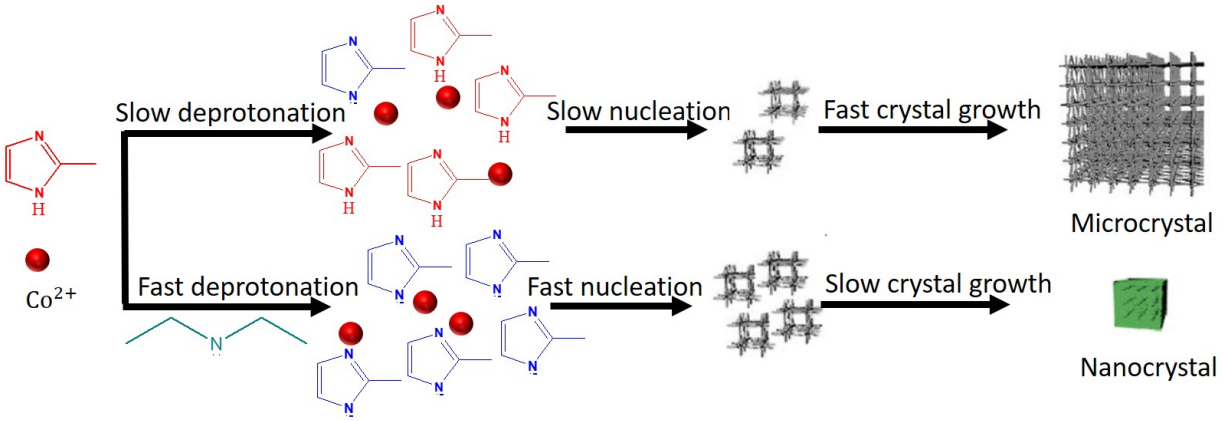

Figure 4.3. Schematic illustration of ZIF-67 formation mechanism in the absence and presence of diethylamine

Figure 4.3 shows an illustration of ZIF-67 formation mechanism in the absence and presence of diethylamine. Modulating ligands have a dual role of acting as competitive ligands at the metal centers as well as bases on the deprotonation of the bridging ligands. Therefore, it is suggested that the presence of modulating ligand increases nucleation rate and then caps the crystals at the surface via both deprotonation and coordination equilibria.[154–156]

Metal: Ligand: Modulating ligand (Molar ratio)
1:4:0
1:16:0
1:4:4
1:16:16

Table 4.1 Synthesized ZIF-67 samples

ZIF-67 samples were synthesized by four different metal: Hmim: DEA ratios listed in Table 1. XRD characterization of ZIF-67 samples in Figure 4.4a shows the pure phase ZIF-67 characteristic peaks for all the samples identical to the simulated crystal structure of the ZIF-67 crystals.[157] The crystal size of ZIF-67 particles was calculated using the Scherrer equation.[158] The

results indicated by increasing the Hmim: metal ratio the crystal size decreases from 48nm (1:4:0 sample) to 35nm (1:16:0 sample). The incorporation of DEA caused a more drastic change of crystal size, with 18nm for (1:4:4 sample) to 13nm (1:16:16 sample). SEM pictures in Figure 4.4b-e demonstrate how increasing the Hmim: metal ratio changes particle size from ~800nm to ~200 nm while adding modulating ligands results into nano-size ZIF-67 samples. It is also worth mentioning that nano-size ZIF-67 particles showed a high tendency to agglomerate, therefore we used DLS as an apparatus to measure the size distribution of nano-size ZIF-67 samples (Figure 4.5). DLS showed an average size of 75nm and 40nm for 1:4:4 and 1:16:16 samples and 300nm and 850nm for 1:16:0 and 1:4:0 samples which is consistent with SEM images. To evaluate the pore structure of ZIF-67 samples isotherm measurement was carried out using N_2 adsorption/desorption to measure the specific surface area and pore size distribution.

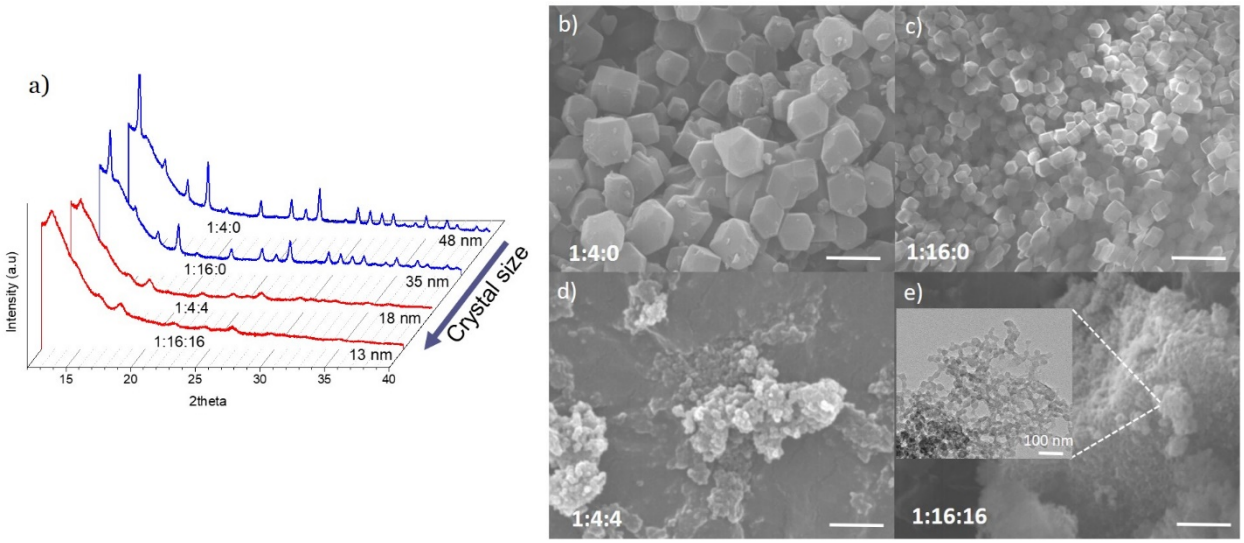

Figure 4.4. a) XRD characterization and b-d) SEM pictures of ZIF-67 samples synthesized using different metal: Ligand: Modulating ligand ratios (Inset in panel e shows the TEM image of 1:16:16 ZIF-67)

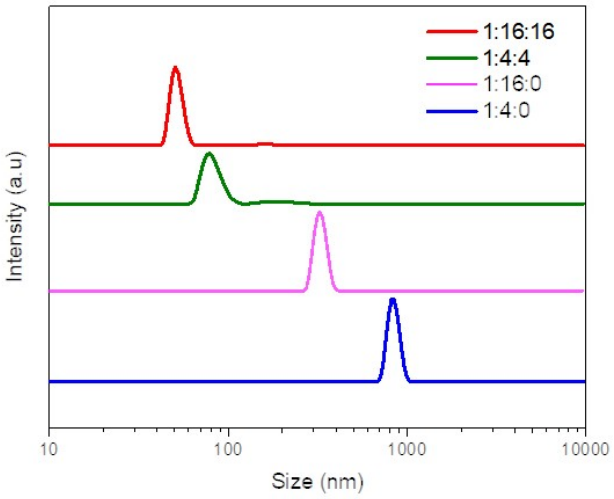

Figure 4.5. The size distribution of different ZIF-67 particles in methanol

Figure 4.6a shows N_2 adsorption/desorption isotherms of the ZIF-67 samples. As it can be seen, in the absence of modulating ligands, large ZIF-67 particles (1:4:0 and 1:16:0) show type I isotherms with microporous characteristics while nano-size ZIF-67 formed in the presence of modulating ligand demonstrate type IV isotherms with mesoporous characteristics.[159] Pore size distribution of ZIF-67 samples were calculated by BJH method[160] using desorption data and are presented in Figure 4.6b. 1:16:16 and 1:4:4 ZIF-67 samples showed much higher pore volume than the rest, 0.628and 0.464 $cm^3\ g^{-1}$ respectively, while 1:16:16 samples showed a narrower pore size distribution than the 1:4:4 sample with an average pore size of around 8nm. The pore volume for large ZIF-67 particles were 0.031 and 0.038 $cm^3\ g^{-1}$ for 1:4:0 and 1:16:0. The details of Structural characteristics of ZIF-67 samples derived from N_2 adsorption/desorption isotherms can be found in Table 4.2.

ZIF-67	SSA (m^2g^{-1})	Pore volume (cc g^{-1})	Avg. Pore size (nm)
1:4:0	1296.498	0.031	3.30
1:16:0	1457.095	0.038	3.30
1:4:4	1346.501	0.628	12.63
1:16:16	1333.656	0.464	7.95

Table 4.2. Structural characteristics of MOF templates derived from N_2 adsorption/desorption isotherms

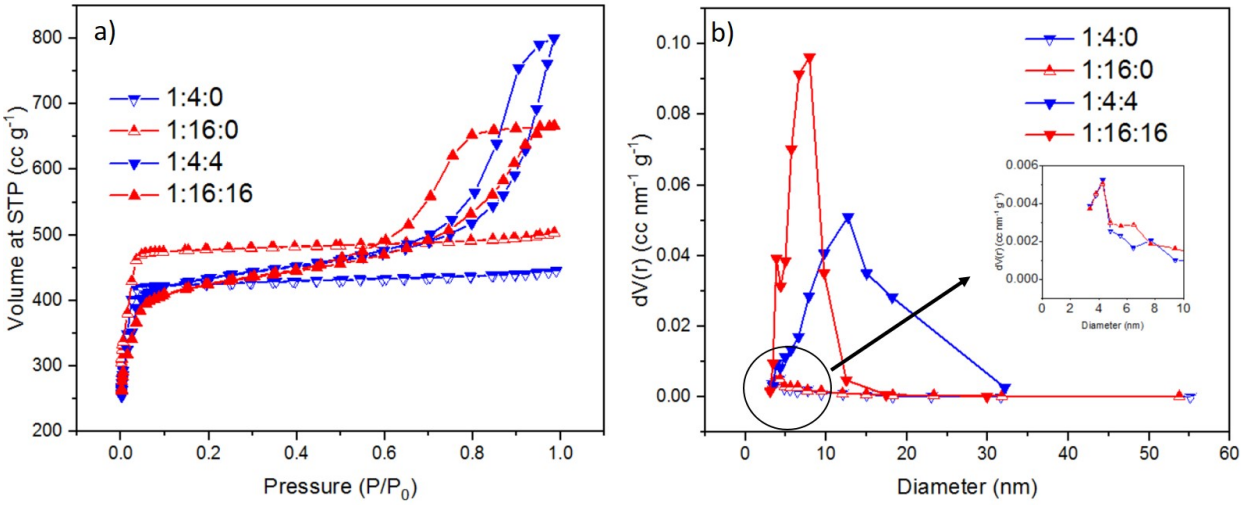

Figure 4.6. a) N2 adsorption/desorption isotherms and b) Pore size distribution of ZIF-67 templates with different sizes (Enlarged view of 1:4:0 and 1:16:0 ZIF-67 pore size distribution)

The second step for template preparation was controlled by etching of initial MOF samples to form a layered-double hydroxide structure. During the etching process, ZIF-67 serves as a sacrificial template that is gradually etched during hydrolysis of Ni^{2+} ions. The Co^{2+} ions released from the etched MOF might be partially oxidized into Co^{3+} by dissolved O_2 and NO_3^- ions in the solution. The Co^{2+} /Co^{3+} ions will eventually coprecipitate with Ni^{2+} ions and form Ni-Co LDH on the surface of the MOF structure. [161–163]

ZIF-67	Etching concentration (mg mL^{-1} Ni^{2+})	ZIF-67/LDH	Metal oxide
1:16:16	1.2	1:16:16-30	1:16:16-30 MO
1:16:16	2.4	1:16:16-60	1:16:16-60 MO
1:16:16	3.6	1:16:16-90	1:16:16-90 MO
1:16:0	2.4	1:16:0-60	1:16:0-60MO
1:16:0	3.6	1:16:0-90	xx

Table 4.3. List of studied MOF/LDH and metal oxide samples derived from ZIF-67 templates

For this matter, two ZIF-67 samples were selected, 1:16:16 as a nano-size and 1:16:0 as a regular ZIF-67. Table 2 lists the ZIF-67 templates exposed to different etching conditions and the MOF/LDH and $NiCo_2O_4$/Co_3O_4 products derived. To make ZIF-67/LDH, the initial MOF particles were dispersed in ethanol and consecutively exposed to Ni^{2+} concentrations of 1.2, 2.4, and 3.6 $mg.mL^{-1}$ (30, 60, and 90 mg in 25 mL of ethanol respectively) for 30 minutes to investigate how etching affects ZIF-67 structure.

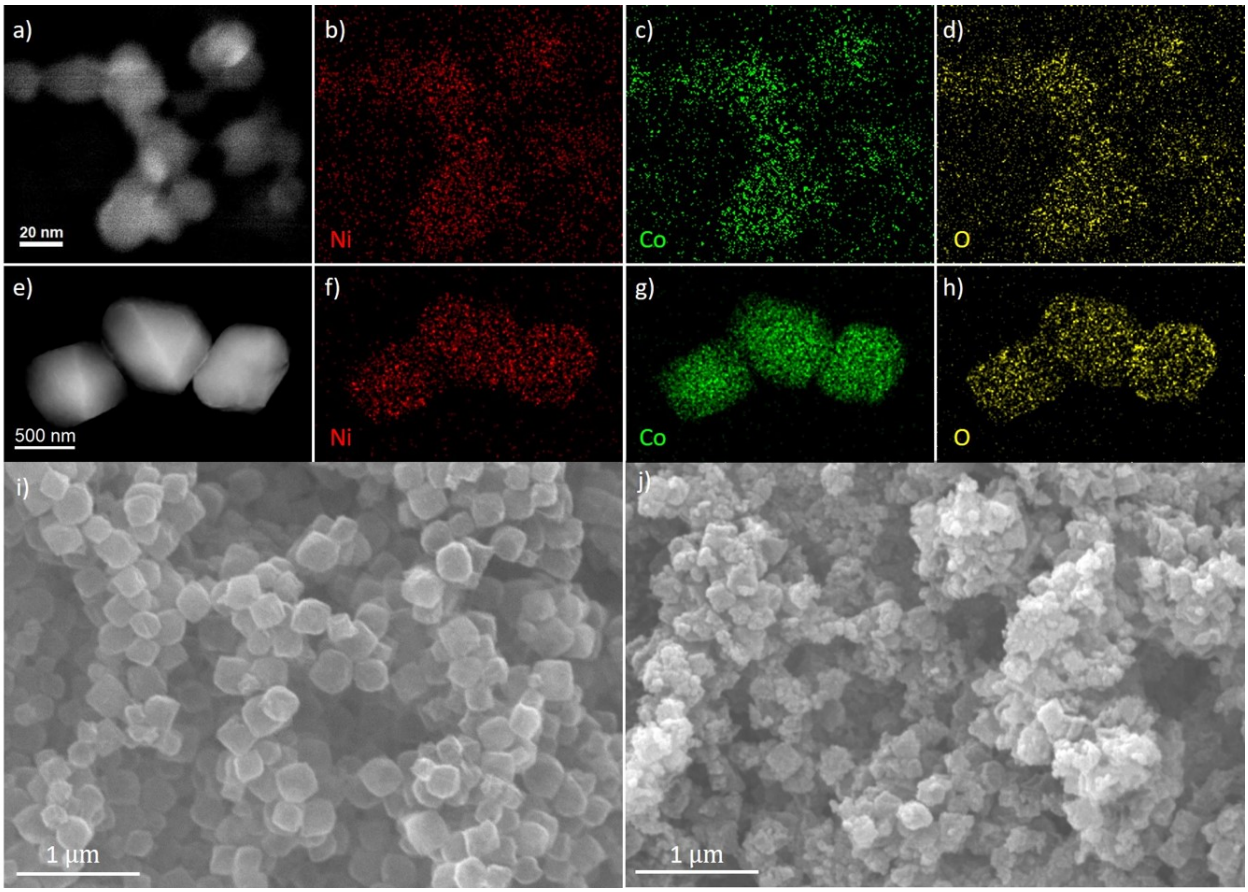

Figure 4.7. a,e) TEM images of 1:16:16-60 (a) and 1:16:0-60 (e) ZIF-67/LDH particles, c) EDS elemental mapping of ZIF-67/LDH particles showing how LDH is formed on the surface of ZIF-67 templates, i,j) SEM images of ZIF-67/LDH particles derived from (1:16:0) MOF particles exposed at different etchant concentrations(2.4 (a) and 3.6 mg mL^{-1} Ni^{+2} etchant)

Elemental mapping of ZIF-67/LDH particles derived from 1: 16:16 (Figure 4.7b-d) and 1:16:0 samples (Figure 4.7f-h) is determined by EDX mapping under TEM. As it can be seen, for the same Ni^{2+} concentration, nano-size ZIF-67 shows a uniform concentration of Ni throughout the structure while for larger ZIF-67, Ni signal is more significant near the outer surface of ZIF-67/LDH. Nickel percolation through the MOF seems to be promoted by the high porosity of nano-size ZIF-67. Increasing Ni^{2+} concentration causes excessive etching of ZIF-67 particles showing a destructive effect on the MOF structure and causes the growth of clusters of nuclei on the surface of MOF particles (Figure 4.7j).

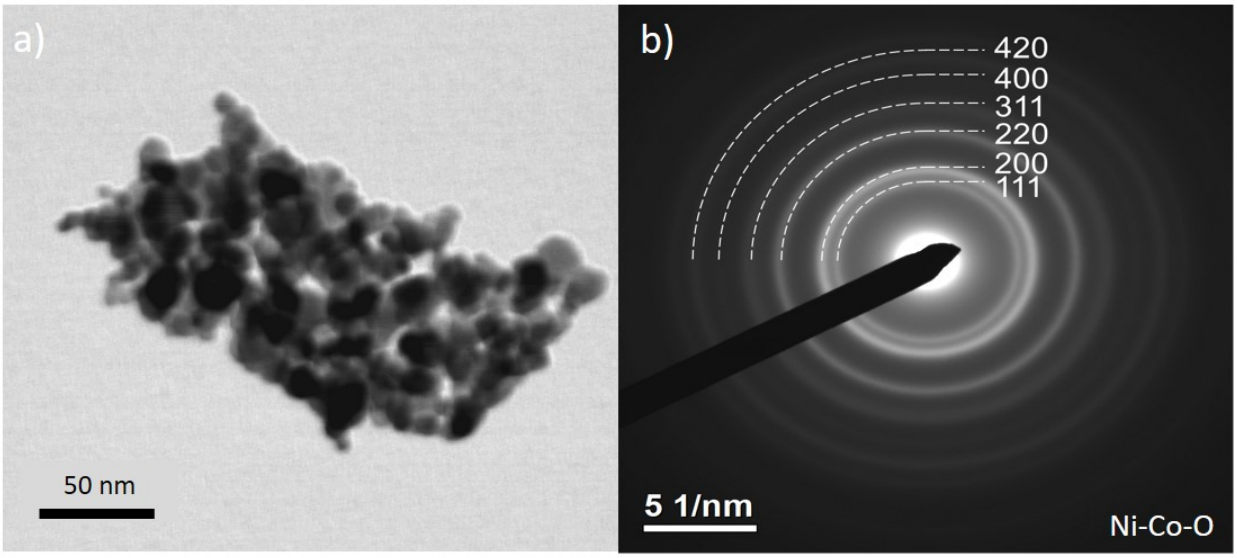

Figure 4.8. a) TEM image and b) SAED pattern analysis of 1:16:16-60 MO.

The ZIF-67/LDH composite particles were later calcinated at 400 °C for 2 h with a heating ramp of 1 °C min^{-1}. To have a better understanding of the effect of MOF structure and etching process on the final metal oxide, $Co_3O_4/NiCo_2O_4$ samples with different etching conditions and MOF template sizes were prepared as they are listed in Table 2. TEM image of $Co_3O_4/NiCo_2O_4$ derived from 1:16:16-60 ZIF-67/LDH samples in Figure 4.8a shows a strong agglomeration of $Co_3O_4/NiCo_2O_4$ particles with the SAED patterns (Figure 4.8b) confirming the formation of crystalline $Co_3O_4/NiCo_2O_4$ (JCPDS card No. 20-0781, JCPDS card No. 42-1467).

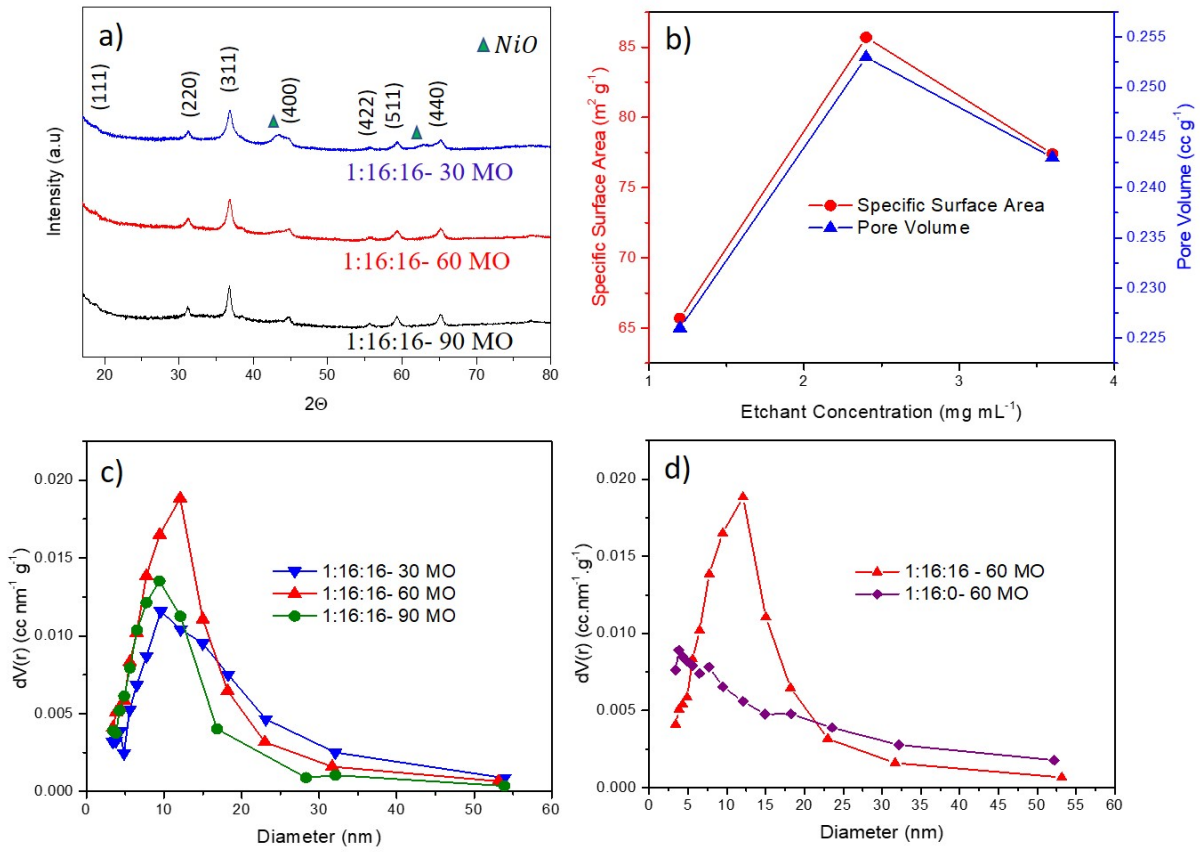

Figure 4.9. a) XRD characterization, b) Specific surface area and pore volume, and c) Pore size distribution of $Co_3O_4/NiCo_2O_4$ derived from (1:16:16) MOF template exposed to different etchant concentrations. d) Pore size distribution of metal oxides derived from different MOF templates.

Metal Oxide	SSA (m^2g^{-1})	Pore volume (cc g^{-1})	Avg. Pore size (nm)
1:16:16-30 MO	65.757	0.226	9.49
1:16:16-60 MO	88.757	0.253	12.04
1:16:16-90 MO	77.45	0.243	9.40
1:16:0-60 MO	84.67	0.210	3.20

Table 4.4. structural characteristics of Co_3O_4 /$NiCo_2O_4$ derived from N_2 adsorption/desorption isotherms

1:16:16-30 MO, 1:16:16-60 MO, and 1:16:16-90 MO were further characterized to understand the effect of etching on metal oxide structure. As it can be seen in Figure 4.9a, increasing Ni^{2+} amount promotes etching to result in the emergence of NiO peaks (JCPDS card No. 47-1049). This could explain the origin of bulky nuclei in figure 4.7j since higher Ni^{2+} concentration will facilitate nickel precipitation over Co^{2+} /Co^{3+} ions. The samples' structures were further analyzed by N_2 adsorption/desorption. As the etching of the MOF template has increased, the pore size volume and surface area of derived metal oxides have initially increased and then decreased (Figure 4.9b). This result can be explained by considering the formation of microchannels during MOF dissolution when exposed to a moderate amount of Ni^{2+} and later intensifying the etch process destroys the MOF structure, losing surface area and microchannels that were created initially. Figure 4.9c shows how the pore size distribution and relative volume of the metal oxides further change by changing the etching concentration. 1:16:16-60 MO shows higher relative pore volume as expected with an average pore size of 12 nm. The pore size distribution and relative pore volume of 1:16:16-60 MO and 1:16:0-60 MO samples is demonstrated in Figure 4.9d to further compare the effect of MOF template on final metal oxide structural characteristics. Co_3O_4/$NiCo_2O_4$ derived from 1:16:16 ZIF-67 show significantly higher relative pore volume as well as narrower pore size distribution.

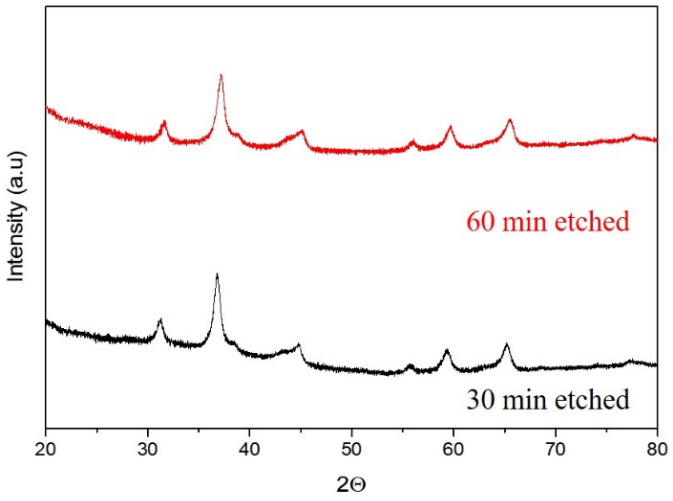

Figure 4.10. XRD characterization for $Co_3O_4/NiCo_2O_4$ derived from 1:16:16 MOF at 2.4 mg mL^{-1} Ni^{2+} for 30 and 60 minutes

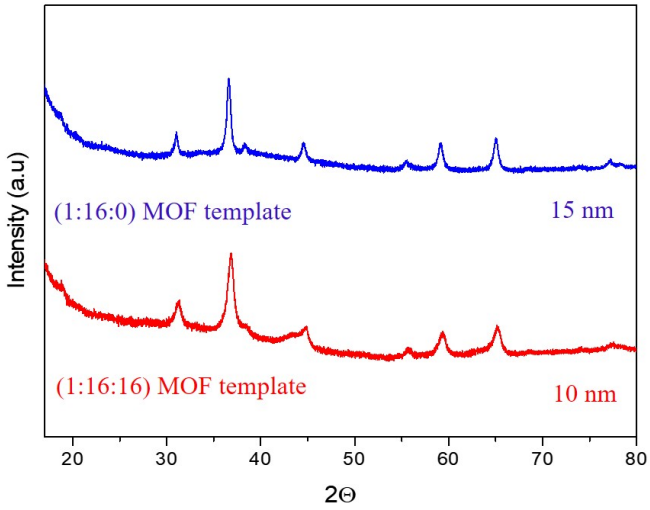

Figure 4.11. XRD characterization for $Co_3O_4/NiCo_2O_4$ derived from different MOF template sizes exposed to 2.4 mg mL^{-1} etchant concentration

In addition, we analyzed the crystal structures of metal oxides derived from 1:16:16-60 samples while exposed to Ni^{2+} for different periods (Figure 4.10) to investigate the possible emergence of NiO peaks. The XRD peaks for 1:16:16-60 MO samples exposed for 60 and 30 minutes show no change in the crystal structure of metal oxide. This suggests that the 30-minute time frame is sufficient for the complete reaction of Ni^{2+} with ZIF-67 nanocrystals. We also calculated the crystal size of $Co_3O_4/NiCo_2O_4$ derived from different MOF templates to investigate the crystal size change (Figure 4.11). The results suggest a drastic change for 1:16:0 based samples, as the metal oxide crystal is 15 nm in comparison to 35 nm crystals for the MOF template. On the other hand, for 1:16:16 based samples the change was only around 15% (13 nm for MOF while 10nm is the calculated crystal size for the metal oxide product).

4.4.2 Electrochemical characterization and supercapacitor performance

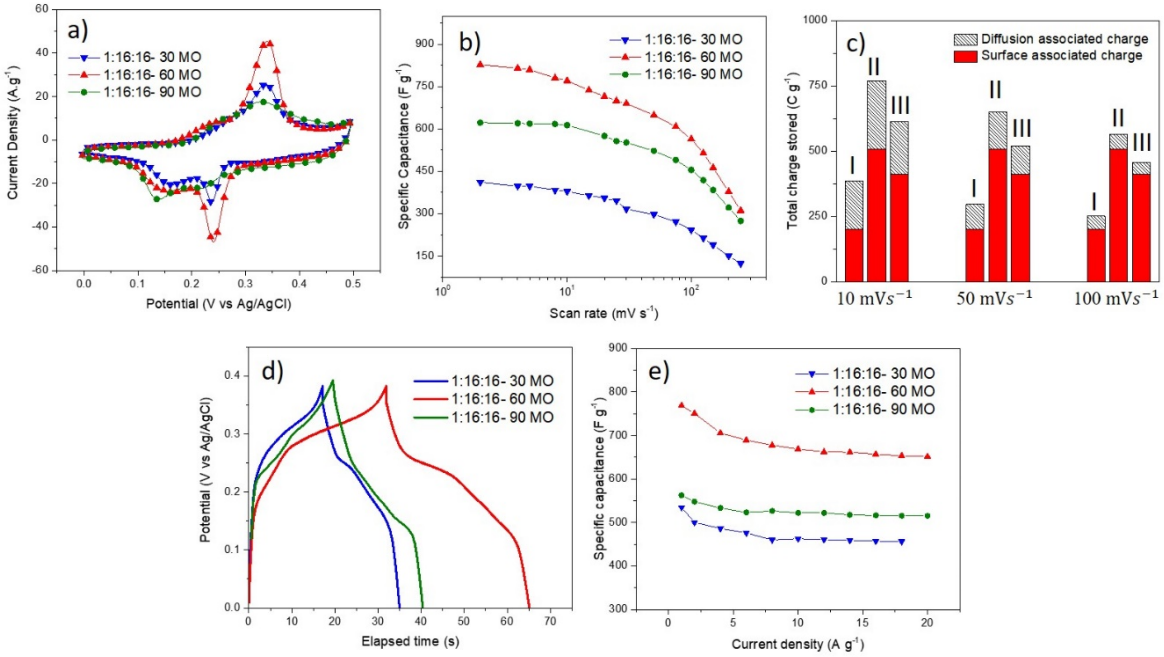

Figure 4.12. a) Cyclic voltammograms at a scan rate of 25 mV s^{-1}, b) Specific capacitance at different scan rates, c) Separation of contributions from capacitive and diffusion-controlled capacities at different sweep rates. I, II and III marks respectively correspond to 1:16:16-30 MO, 1:16:16-60 MO, and 1:16:16-90 MO, d) GCD curves at the current density of 10 A g^{-1} and e) Specific capacitance at different current densities for $Co_3O_4/NiCo_2O_4$ derived from (1:16:16) MOF template exposed to different Ni^{+2} etchant concentrations

We firstly focused on studying the effect of the etching process on the electrochemical performance of metal oxide electrodes. The electrochemical characterization of the samples was conducted in a three-electrode cell assembly with a Pt wire as the counter electrode and Ag/AgCl as the reference in 6M KOH electrolyte. The $Co_3O_4/NiCo_2O_4$ samples tested for this work had a mass loading of around 4 mg cm^{-2} which is higher than most of the reports in the literature. Figure 4.12a shows the CV comparison of 1:16:16-30 MO, 1:16:16-60 MO, and 1:16:16-90 MO samples at a scan rate of 25 mV s^{-1} with a potential window ranging from 0 to 0.5V. 1:16:16-60 CV shows stronger redox peaks in comparison to other samples as well as a larger enclosed area, indicating its superior charge storage. Moreover, CV traces collected at different scan rates (2 ~ 250 mV s^{-1})

with faradic redox peaks observable even at a scan rate of 250 mV s^{-1} (Figure 4.13a-c) imply fast reaction kinetics of the as-prepared $Co_3O_4/NiCo_2O_4$ electrodes. Increasing scan rate tends to shift anodic and cathodic peaks to higher and lower potentials indicating the quasi-reversible nature of the redox couple.[38,164,165] To further understand how the kinetic behavior of $Co_3O_4/NiCo_2O_4$ electrodes, normalized capacitance as a function of $\upsilon^{-1/2}$ was plotted. As Figure 13d shows, there are two kinetical regions (scan rates greater than 50 mV^{-1} and scan rates smaller than 50 mV s^{-1}) defining the system.

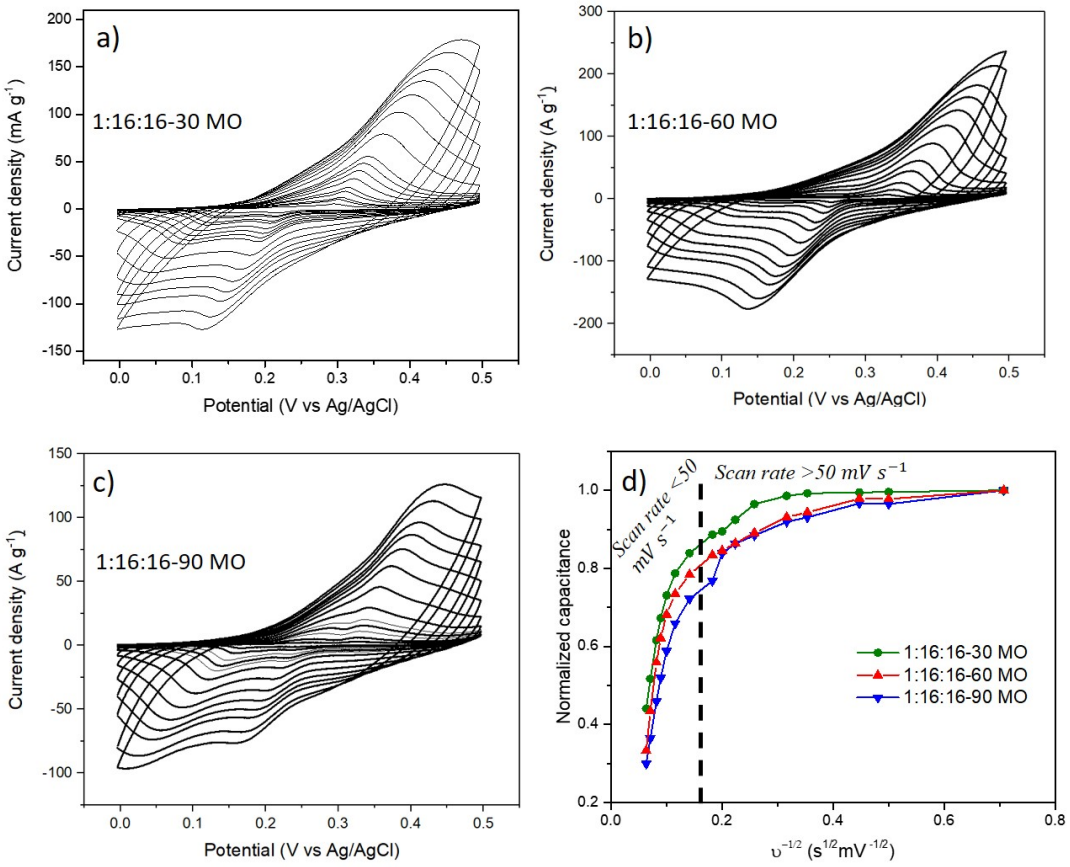

Figure 4.13. a-c) CV scan rates ranging from 2 to 250 (mV/s) for samples at different etching conditions d) Normalized capacitance vs $\boldsymbol{\upsilon^{-1/2}}$ showing two kinetical regions defining the system for Co3O4/NiCo2O4 derived from (1:16:16) MOF template exposed at different etchant concentrations

Gravimetric capacitances of the electrodes versus CV scan rate (Figure 4.12b) shows 1:16:16-60 sample exhibits a higher capacitance at scan rates from 2 mV s^{-1} to 250 mV s^{-1} while 1:16:16-90 holds a better rate capability. To have a better understanding of the structural effects on charge storage, we employed an analysis based on the work of Trasatti and co-workers to separate surface-associated charge and diffusion-associated charge.[166,167] The total charge (q_T) calculated from cyclic voltammogram was separated into two parts: surface capacitive charge (q_s) and diffusion controlled charge (q_d):

$$q_T = q_s + q_d \quad (39)$$

q_s can is assigned to double-layer capacitance and surface redox reactions with fast kinetics while q_d originates from the slower diffusion process. Therefore, a larger fraction of q_s in the total stored charge exhibits a higher rate capability. For a reasonable range of scan rates by assuming semi-infinite linear diffusion, q_d can be defined as a function of $\nu^{1/2}$ and q_s can be derived by plotting q_T against the reciprocal of the square root of scan rate ($\nu^{-1/2}$) and extrapolating ν to ∞[168], as it is indicated in the equation below (Figure 4.14):

$$q_T = q_s + c\nu^{-1/2} \quad (40)$$

Polarization effects at higher scan rates that cause deviations from the linearity of the abovementioned equation are ignored here.[166–168] Contribution of surface-controlled and diffusion-controlled charges to total charge storage are displayed in Figure 4.12c. It shows that the majority of charge storage is associated with surface-controlled reactions of the metal oxide electrodes and that this role increases as the scan rate is increased. At a scan rate of 10 mV s^{-1}, 1:16:16-60 MO shows the highest total charge stored with around 63% charge contribution from surface controlled

reactions, while 1:16:16-90 MO shows better rate capability with surface controlled reactions contribution of 70% to the toral charge stored.

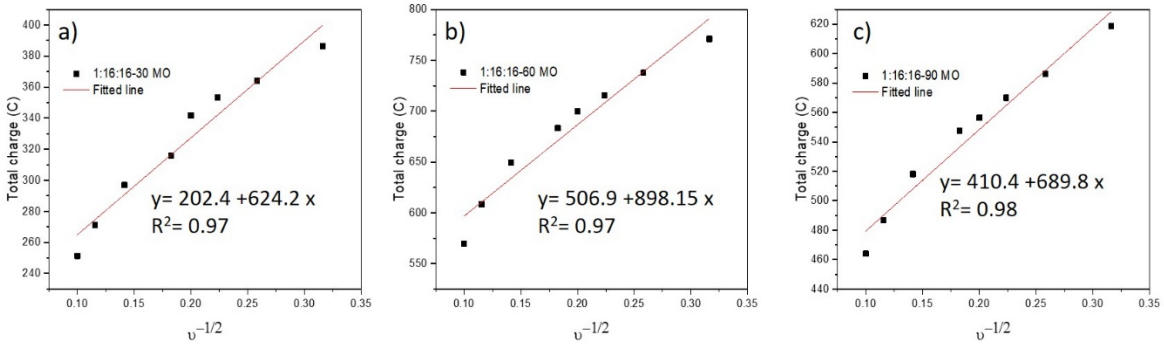

Figure 4.14. a-c) Examples of plotting the total voltammetric charge Q_T against the reciprocal of the square root of the potential sweep rate (ν) and extrapolating ν to ∞

Galvanostatic charge/discharge (GCD) tests were further conducted to study the charge/discharge behavior. Figure 4.12d presents charge/discharge curves for different electrodes at a current density of 10 A g^{-1} with a potential window from 0 to 0.4 V. The charge/discharge curves with similar duration suggest the excellent reversibility of redox reactions.[169] Gravimetric capacitance at different charge/discharge rates is presented in Figure 4.12e. The 1:16:16-60 MO electrode shows a capacitance of 770 F g^{-1} at 1A g^{-1} while maintaining 84% of initial capacitance at 20 A g^{-1} showing good rate capability.

To further study the effect of template size, 1:16:60-60 MO and 1:16:0-60 MO electrodes were compared. The etching conditions were the same for these two samples. Comparison of CV traces at 25mV s^{-1} shows stronger redox peaks for 1:16:16-60 MO as well as higher gravimetric capacitance at different scan rates (2 ~ 250 mV s^{-1}) as shown in Figures 4.15a-b. It should be mentioned that the redox peaks were observable for the samples that were being compared. (Figure 16 a-b). Figure 16c gives a better insight of the effect of particle size on the kinetic behavior of the electrodes, as both 1:16:0-60 MO and 1:16:16-60MO samples show two regions, a capacitive

region for scan rates lower than 50 mV s^{-1} and a diffusion-limited region at scan rates above 50 mV s^{-1}. We separated surface-associated and diffusion-associated charges as described previously (Figure 4.15c). 1:16:16-60 MO shows higher surface-controlled charge contribution than 1:16:0-60 MO (65% in comparison to 55% respectively at 10 mV s^{-1}), suggesting better active site accessibility with less diffusion resistance.

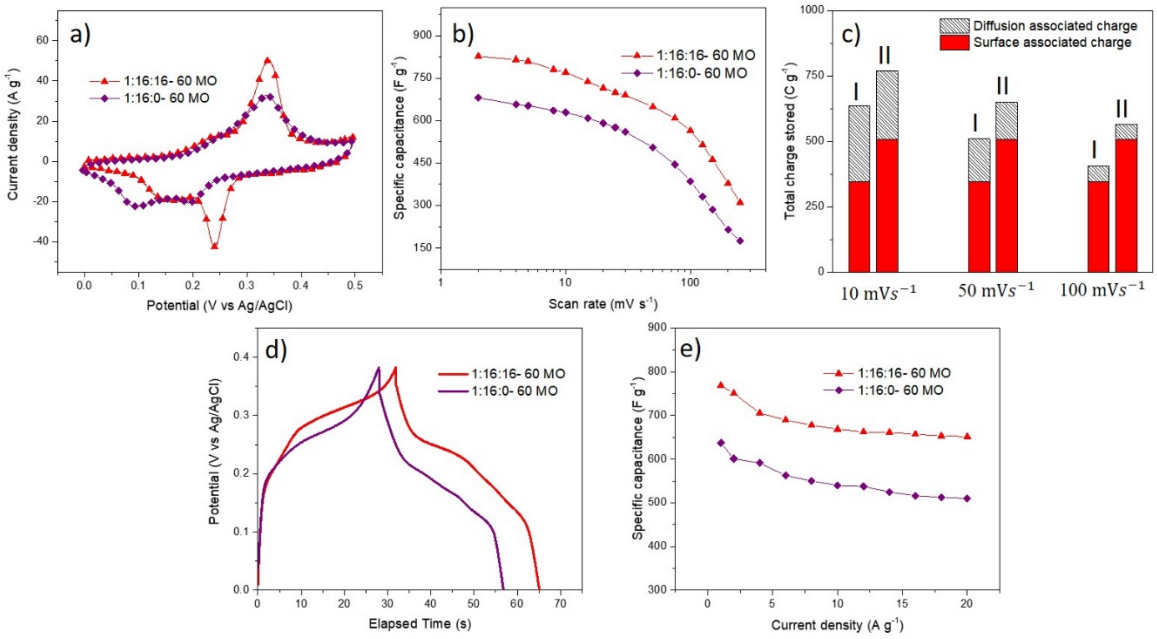

Figure 4.15. a) Cyclic voltammograms at a scan rate of 25 mV s^{-1}, b) Specific capacitance at different scan rates, c) Separation of contributions from capacitive and diffusion-controlled capacities at different sweep rates. I, II marks respectively correspond to 1:16:16-60 MO, 1:16:0-60 MO, d) GCD curves at the current density of 10 A g^{-1} and e) Specific capacitance at different current densities for $Co_3O_4/NiCo_2O_4$ derived from different MOF templates

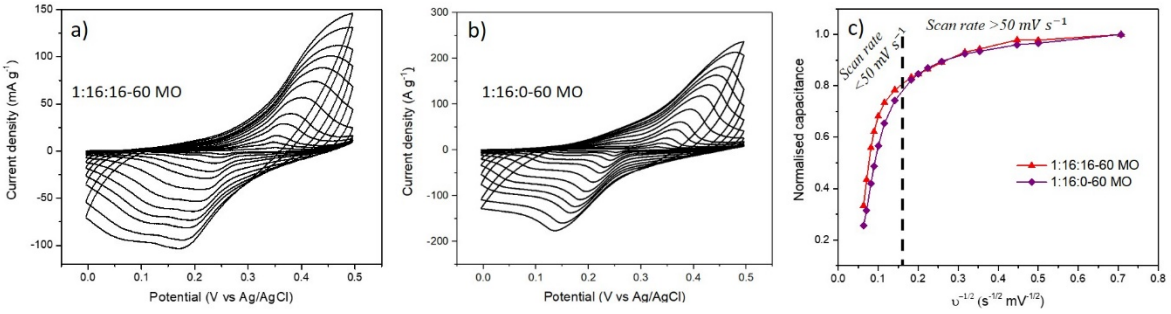

Figure 4.16. a-b) CV scan rates ranging from 2 to 250 (mV s^{-1}) for samples, c) Normalized capacitance vs $\boldsymbol{\upsilon^{-1/2}}$ showing two kinetical regions defining the system

Figure 15d presents charge/discharge curves at a rate of 10 A g^{-1} with a showing superior performance of 1:16:16-60 MO. This was supported by calculating gravimetric capacitance from galvanostatic charge/discharge tests at different current densities (Figure 15e) with 1:16:0-60 MO maintaining 78% of initial capacitance at 20 A g^{-1} which is inferior to 1:16:16-60 MO (84% capacitance retention). A related analysis is taken to investigate the relationship between peak current and scan rate according to the equation.

$i = av^b$ (41)

The value of $b = 0.5$ indicates semi-infinite linear diffusion-controlled charge storage, whereas $b = 1$ indicates capacitive-dominated charge storage. The b value can be obtained by plotting log(i) vs log(v) as shown in Figure4.17. As it can be seen, the b value changes from the values closer to 1 to the values closer to 0.5 as the scan rates

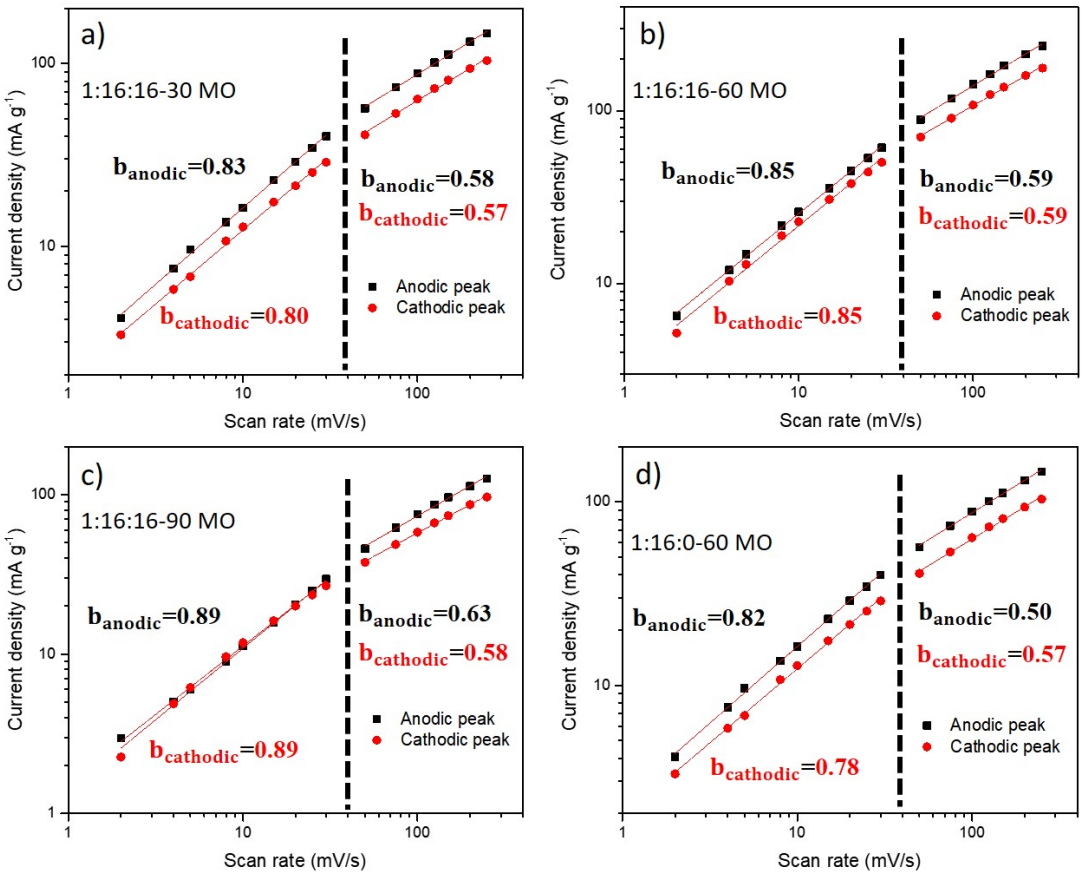

Figure 4.17. a-c) Voltammetric current dependence of peak currents to scan rates ranging from 2 to 250 (mV s-1)

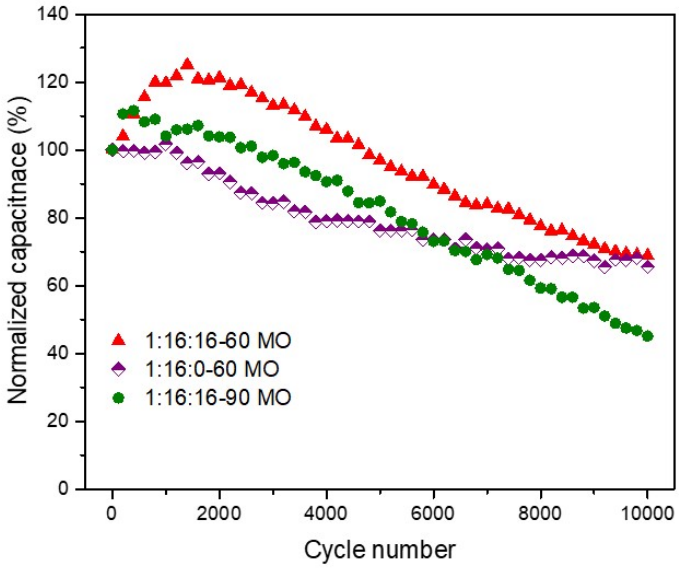

Figure 4.18. Stability test of metal oxide samples after 10k cycles showing the effect of crystal size and etching conditions on the stability of structures

The cycling stability of the electrodes was further tested by exposing them to continuous charge/discharge cycling at 10 A g^{-1} for 10,000 cycles (Figure 4.18). For this comparison, the results were normalized for each sample based on initial gravimetric capacitance to determine the capacitance retention of electrodes during the test. After 10,000 cycles, 1:16:16-90 MO electrode retains only about 45% of capacitance while 1:16:16-60 MO and 1:16:0-60 MO electrodes show similar results by keeping about 68% and 65% of their capacitance, respectively. This result shows the negative effect of excess etching on the electrochemical stability of metal oxide structure. Furthermore, the 1:16:16-60 MO sample showed an initial increase in capacitance over the first 2000 cycles that could be due to the activation of new redox-active sites.

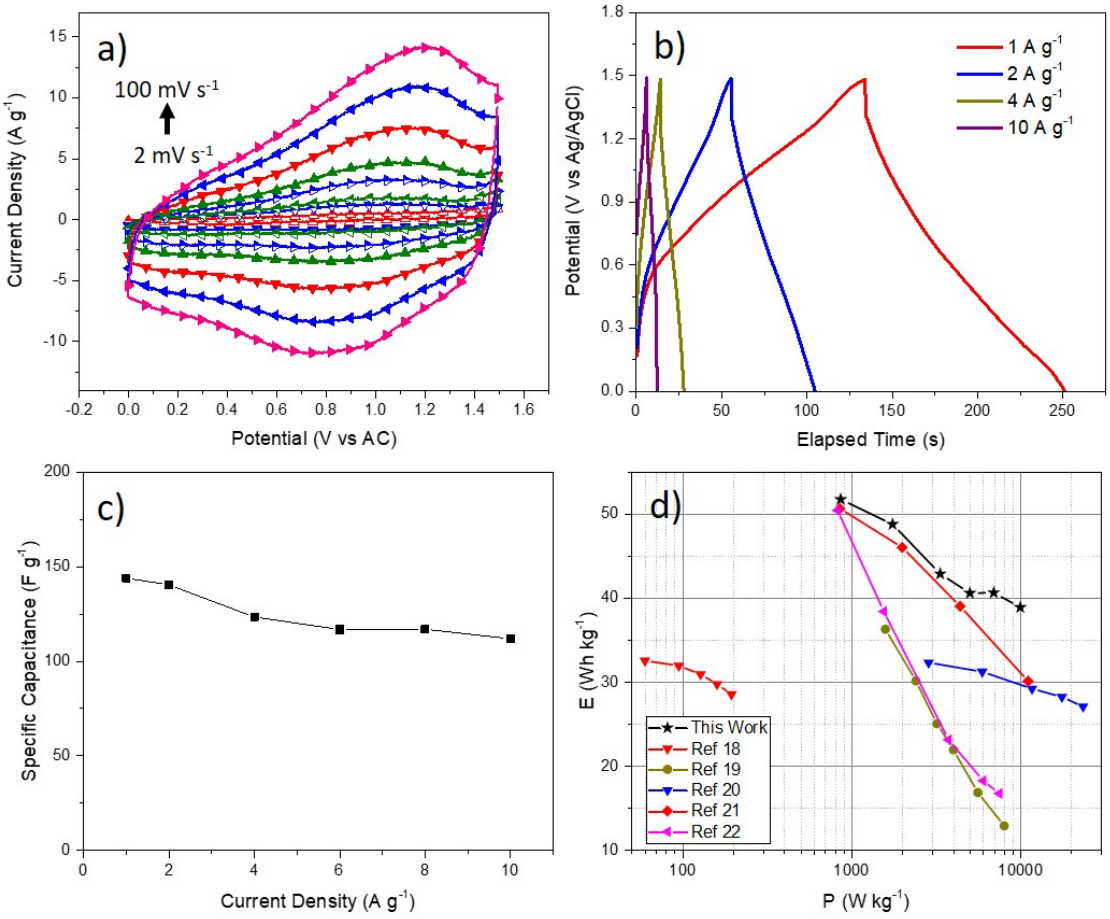

Figure 4.19. Co_3O_4/ $NiCo_2O_4$ // AC asymmetric cell a) CV at different scan rates, b) GCD Specific capacitance at different current densities c) Specific capacitance at different discharge rates d) Ragone plot showing specific energy vs specific power of the cell at different working conditions

To assess the feasibility of using such template-based metal oxide structures in energy storage devices, we assembled an asymmetric cell using 1:16:16-60 MO as a cathode and a commercial activated carbon as an anode material. As presented in Figure 19a, the CV curves of assembled Co_3O_4/$NiCo_2O_4$//AC cell (2 ~ 100 mV s^{-1}) indicate the excellent capacitive behavior of the asymmetric supercapacitor with a stable potential window between 0 and 1.5 V. Charge/discharge curves at different current densities were illustrated in Figure 19b with a symmetric shape indicating good coulombic efficiency and excellent reversibility of

$Co_3O_4/NiCo_2O_4$//AC asymmetric supercapacitor. The gravimetric capacitance of the asymmetric supercapacitor at different discharge rates was calculated and presented in Figure 19c with a gravimetric capacitance of 144 F g^{-1} at 1 A g^{-1} and 111 F g^{-1} at 10 A g^{-1} showing excellent rate capability (77% of initial capacitance). Figure 19d represents the Ragone plot of reported ZIF-67 based asymmetric cells along with the current one. Our assembled cell reaches a maximum energy density of 51.7 Wh kg^{-1} with a power density of 857 W kg^{-1} while keeping an energy density of 38.8 Wh kg^{-1} at a power density of 10 kW kg^{-1}. This result shows improved energy density at high power density comparing with Co_3O_4@$NiCo_2O_4$ on carbon fiber (30.53 Wh kg^{-1} at 200.9 W kg^{-1})[170], Co_3O_4//carbon (36 Wh kg^{-1} at 1.6 kW kg^{-1})[171] , CC@$NiCo_2O_4$ (31.9 Wh kg^{-1} at 2.9 kW kg^{-1})[172], Co–Co_3O_4@ZIF-$NiCo_2O_4$ (30.2 Wh kg^{-1} at 11.1 kW kg^{-1})[173], Graphene/$Ni_xCo_{-x}O_4$ (23.3 Wh kg^{-1} at 3.75 kW kg^{-1}).[174]

4.5 Conclusion

In this work, ZIF-67 was used as a template to synthesize $Co_3O_3/NiCo_2O_4$ highly porous metal oxide structures. The ZIF-67 structure was initially etched by $Ni(NO_3)_2$ in ethanol to form ZIF-67/Ni-Co LDH and consecutively calcinated in the air to form $Co_3O_3/NiCo_2O_4$. We designed a series of experiments to identify the effect of ZIF-67 structural properties and etching on the electrochemical characteristics of the metal oxides. ZIF-67 nanocrystals with high surface area and superior porosity were synthesized using diethylamine as coordination modulating ligand. We further demonstrated that the etching conditions play an important role in the formation of ZIF-67/Ni-Co LDH to provide channels with enhanced transportation and accessibility of the electrolyte ions while maintaining the ZIF-67 structure. The 1:16:16-60 MO $Co_3O_3/NiCo_2O_4$ showed the highest capacitance with 770 F g^{-1} at 1A g^{-1} while maintaining 84% of initial capacitance at 20 A g^{-1}. The assembled $Co_3O_4/NiCo_2O_4$//AC asymmetric cell showed a gravimetric

capacitance of 144 F g^{-1} at 1 A g^{-1} and 111 F g^{-1} at 10 A g^{-1} with a power density of 10 kW $kg^{-1}$and energy density of 38.8 Wh kg^{-1}.

For future studies, the focus should be on the composite formation of template-based $Co_3O_3/NiCo_2O_4$ structures to prevent agglomeration as well as providing structural support. Overall, this method can be utilized to form many different complex metal oxide structures.

Chapter 5. Self-assembly of template-based $NiCo_2O_4$ composite structures

5.1 Abstract

$NiCo_2O_4(Co_3O_4)$/rGO composites were synthesized via electrostatic self-assembly assembly using surface modification of MOF-based $NiCo_2O_4(Co_3O_4)$ structures and the electrochemical performance of composite structure for high-performance supercapacitor applications is investigated. The $NiCo_2O_4(Co_3O_4)$@rGO electrodes derived from the self-assembly showed capacitance of 969 F g^{-1} at a discharge current density of 1 A g^{-1} while maintaining 690 F g^{-1} (67% of initial capacitance) at 30 A g^{-1} discharge rate as well as remarkable stability, holding 95% of the initial capacitance after 10000 cycles of charge-discharge at 10 A g^{-1} discharge rate.

5.2 Introduction

The ever-growing demand for developing energy storage devices with higher performance and better efficiency has attracted a lot of attention for developing electrochemical capacitors (supercapacitors) as one of the most significant energy storage devices that tend to bridge the gap between EDLC capacitors and batteries by providing considerable energy density, high power density, fast charge-discharge rate, and long cycle life. Transition metal oxides such as MnO_2[175], Co_3O_4[134], NiO[176], and V_2O_5[177] have been investigated intensively as electrode materials for electrochemical capacitors due to their multiple oxidation states that provide high specific capacitance. Two of the biggest drawbacks metal oxides face for supercapacitor applications are first, their low electrical conductivity that hinders their rate capability, and secondly, their structural degradation and low cycle stability. It is suggested that doping other transition metal

atoms into the metal oxide structures could improve the electrical conductivity and increase redox activity as well. Therefore, mixed transition metal oxides with two cation species have been studied in recent years. Bimetallic oxide structures offer higher capacitance due to redox coupling of two metal oxides and relatively higher electrical conductivity owing to the lower electron transfer activation energy between cations.[178,179] $NiCo_2O_4$, a bimetallic spinel oxide structure, with high electrical conductivity and redox activity in comparison to NiO and Co_3O_4, shows great potential for supercapacitor applications.

It has been suggested that to improve the performance of metal oxide-based electrochemical capacitors, the ion-accessibility of their active sites, electrical conductivity, and mechanical stability should be improved. Metal-organic-frameworks (MOFs) a class of inorganic-organic crystalline structures is well known for their high surface area and interconnected pores and ordered structure. The ability to tune the pore size and structural properties of MOFs have made them a promising template for the preparation of nanostructures such as porous carbon[180,181], metals[182], metal oxides[183,184], metal sulfides[185]. The resulting metal oxides derived from MOFs inherit the high surface area and porosity that makes them favorable for energy storage applications. Besides, MOFs ordered structure allows the controllable synthesis of metal oxide structures.

To overcome the electrical conductivity issue, metal oxide structures can be mixed with conductive structures such as graphene sheets, carbon nanotubes, and conductive polymers to form composite structures. The composite formation could also provide mechanical support that boosts the structural integrity during charge/discharge of metal oxide structures and therefore enhance their cycle stability. There have been different studies on the composite formation of metal oxide

structures [108,186–188] but neither focused on the effect of composite formation strategy and its effect on composite morphology and electrochemical performance.

In our previous work, we tended to control the structural properties of the MOF template by coordination modulation and how it is possible to tune the metal oxide nanostructure through tailoring the sacrificial template. That work showed promising results on using highly porous MOF nanocrystals for the template-based synthesis of $NiCo_3O_4$(Co_3O_4) nanostructures but nevertheless, the metal oxide nanostructure suffered from intense agglomeration and started to lose considerable charge storage capacitance after long cycles. Here, the focus of our study is exploiting different strategies to develop MOF-based metal oxide composite structures and investigate how these composites' electrochemical performance is affected. $NiCo_2O_4$(Co_3O_4) was synthesized from ZIF-67 templates using the coordination modulation method developed previously and later $NiCo_2O_4$(Co_3O_4)/GO was fabricated via an electrostatic self-assembly method. as-prepared $NiCo_2O_4$(Co_3O_4) nanostructures were modified with 3-aminopropyltriethoxysilane (APTES) to obtain a positively charged surface. We aim to better understand how rGO provides support for the metal oxide particles and improves the electrical conductivity of the composite structure.

5.3 Experimental section

5.3.1 $NiCo_2O_4$(Co_3O_4)/rGO composite: ZIF-67 was synthesized through modulation ligand was converted to MO through calcination, 100 mg was dispersed in a mixture of 40 mL ethanol and 10 mL DI water and sonicated for 30 minutes. Next, 0.3 mL of ammonium hydroxide was added, and

the solution was sonicated for 30 minutes again. After sonication, 0.1 mL of APTES was added and the solution stirred at room temperature for 24 hours. After stirring was completed, the solution was then washed and centrifuged 3 times with ethanol and DI water and dried at 60°C overnight. Once dry, it was then dispersed in 20 mL of DI water and sonicated for 30 minutes before adding 3.5 mg/mL GO solution. GO was added to the MO dispersion with a mass ratio of 1 to 5 and the suspension was left to stir for 2 hours to form $NiCo_2O_4(Co_3O_4)$/GO. At last, GO was reduced to rGO by adding N_2H_4 to the dispersion and to form $NiCo_2O_4(Co_3O_4)$/rGO.

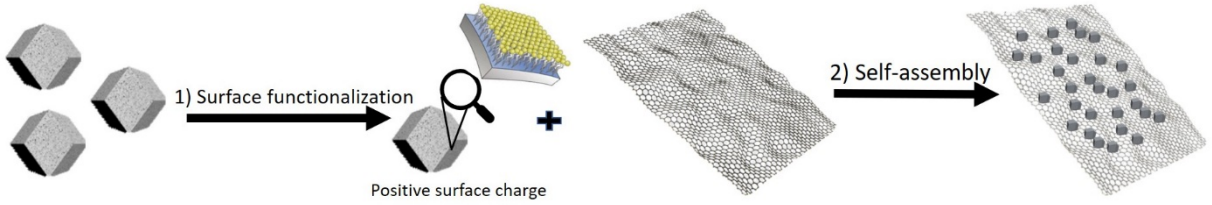

Figure 5.1. Schematic illustration of $NiCo_2O_4(Co_3O_4)$/rGO composite formation process

5.3.2 Materials characterization: The crystal structures were characterized by a PROTO AXRD theta-theta X-ray diffractometer operated using a Cu Kα radiation (40 kV, 30 mA). Raman spectra were collected by a 514 nm line air-cooled 20 mW argon ion laser using a Renishaw inVia Raman microscope system. The composite structure and morphology were further studied using a JEOL JSM-7000F scanning electron microscope (SEM)**.** Nitrogen adsorption-desorption provided surface area and pore size distribution via Brunauer–Emmett–Teller (BET) method and Barrett–Joyner–Halendar (BJH) method using Quantachrome NOVA 2200e.

5.3.3 Electrochemical characterization: The electrochemical measurements were performed using PARSTAT 4000 potentiostat (Princeton Applied Research) at room temperature with a three-electrode setup using prepared composites as working electrodes, Pt coil as the counter

electrode, Ag/AgCl reference electrode in 6 M KOH electrolyte. To fabricate the working electrodes, active material, poly(vinylidene difluoride) and carbon black (Super-P conductive) were mixed with an 80:10:10 weight ratio in NMP. The resulting slurry was coated over Ni foam and dried at 80 °C overnight in a vacuum oven. The working electrode mass loading was kept ~ 4 mg cm^{-2}. Potentiostatic EIS studies were performed using 10 mV amplitude with frequencies ranging from 1 Hz to 100 kHz. The specific capacitance (C_s) of a single electrode is calculated in two ways, from the galvanostatic discharge curves by the equation below:

$$C_s = \frac{I \times \Delta t}{(\Delta V) \times m} \quad (42)$$

Where C_s ($F.g^{-1}$) is the specific capacitance of the electrode, I (A) is the current, Δt (s) is the discharge time, m (g) is the deposited mass on the nickel foam, and ΔV (V) is the working potential window.

And from the CV graphs by using the following equation:

$$C_s = {}^{1}/_{\Delta V} \int_{V_2}^{V_1} j dV/\nu \quad (43)$$

where *C* is the specific capacitance (F g^{-1}), *j* is the cathodic current density (mA g^{-1}), V is the voltage (V), ΔV is the voltage window (V), and ν is the scan rate (mV s^{-1}).

5.4 Results and discussion

5.4.1 Materials characterization and analysis

The structural modulation of nickel cobaltite structures was investigated previously while it was observed that although metal-organic frameworks serve as a favorable template, the highly

porous nanostructures suffered from heavy agglomeration. To overcome this issue, we introduced a self-assembly process to make $NiCo_2O_4(Co_3O_4)$/rGO (Figure 5.1). The as-prepared $NiCo_2O_4(Co_3O_4)$ are dispersed in ethanol mixed with APTES which is an aminosilane frequently used in the process of silanization. This process is to functionalize the surface with alkoxysilane molecules that are commonly for covalent attaching of organic films to metal oxides.[189] Figure 5.2 shows the surface functionalization of $NiCo_2O_4(Co_3O_4)$ particles as the first step of hybrid structure self-assembly.

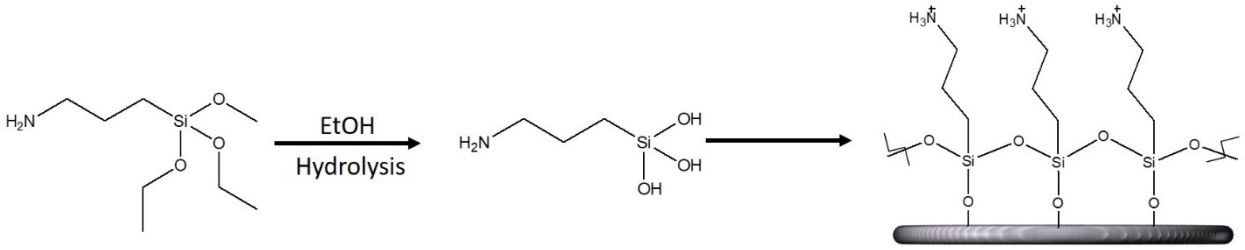

Figure 5.2. Surface functionalization of $NiCo_2O_4(Co_3O_4)$ particles

Once the metal oxides were functionalized, graphene oxide (dispersion in DI water, 3 mg ml^{-1}) is added to the mixture and a sufficient time was allowed until the assembly process was complete. The structure of the new composite was studied using SEM and Raman spectroscopy. SEM images of $NiCo_2O_4(Co_3O_4)$/GO structures are presented in Figure 5.3. As it can be seen, metal oxide nanocrystals are attached to graphene oxide sheets, forming a layered "sandwich-like" structure. Further characterization by TEM is needed to better understand the morphology of the composite.

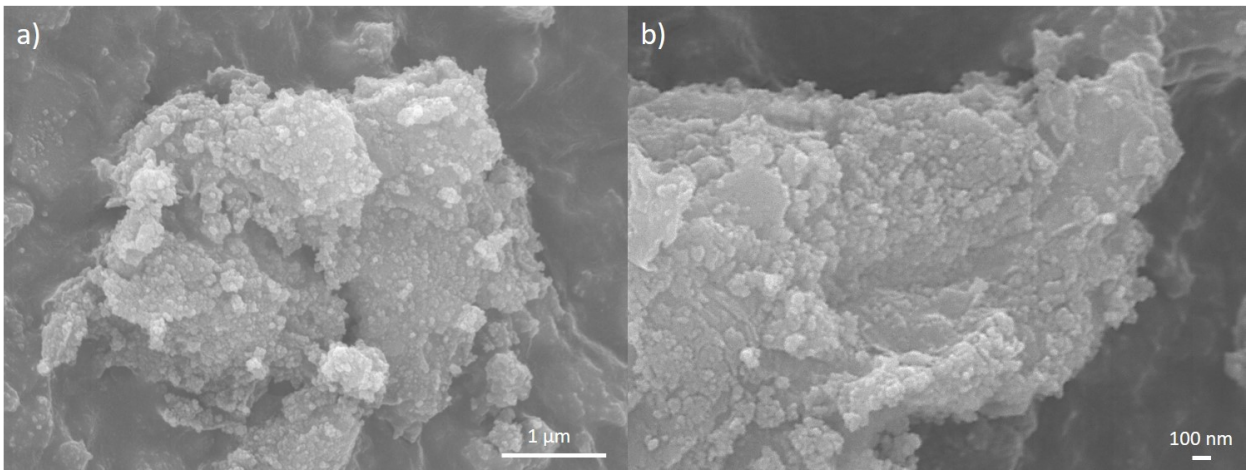

Figure 5.3. SEM images of NiCo2O4(Co3O4)/rGO composite showing a “sandwich” structure

The graphene oxide sheets were later reduced to rGO using N_2H_4 and consecutively $NiCo_2O_4(Co_3O_4)$/rGO was formed. To confirm the successful formation of $NiCo_2O_4(Co_3O_4)$/GO and further reduction to $NiCo_2O_4(Co_3O_4)$/rGO, we used Raman spectroscopy. Figure 5.4a confirms the hybrid structure formation as the Raman characteristic peaks of $NiCo_2O_4$ (532 and 685 cm^{-1}) and graphene (1354 and 1587 cm^{-1}). The I_D/I_G before reduction for GO is around 0.8 while after the reaction with N_2H_4 the ratio changes to 1.05, confirming the successful reduction of GO to rGO. It is also worth mentioning that the peak intensities of graphene compound in the Raman spectra of the composite reduces drastically in comparison to the metal oxide peaks which is due to the GO significant weight loss due to the combination of evaporation of water and removal of labile oxygen functional groups.[108,190]

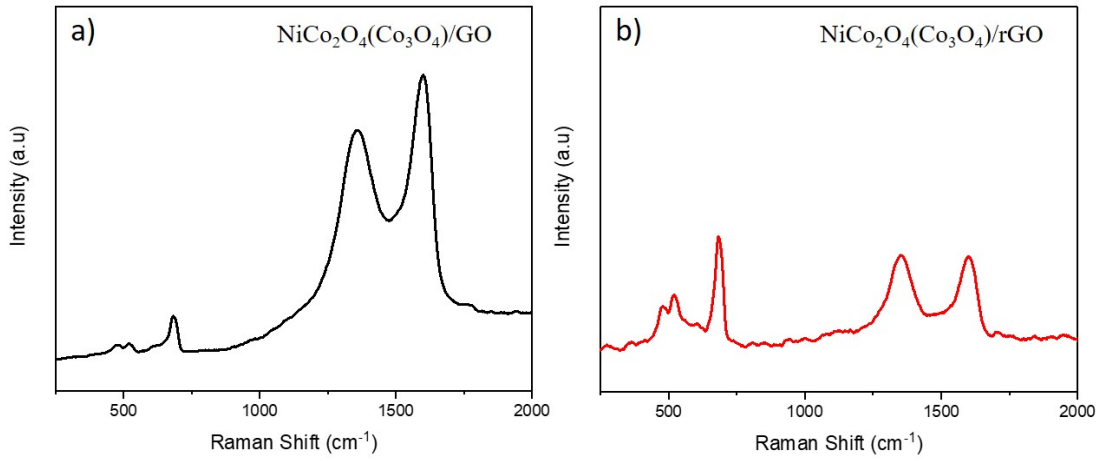

Figure 5.4. Raman spectra of a) NiCo2O4(Co3O4)/GO and b) NiCo2O4(Co3O4)/rGO showing successful chemical reduction of GO in the composite structure

5.4.2 Electrochemical analysis and supercapacitor performance

To understand the effect of composite formation, we conducted various electrochemical tests conducted in a three-electrode cell assembly with a Pt wire as the counter electrode and Ag/AgCl as the reference in KOH electrolyte. The prepared samples tested for this work had a mass loading of around 3.5 mg cm $^{-2}$. Figure 5.5a shows the CV comparison of the composite and metal oxide structures at a 25 mV s^{-1} scan rate. The larger enclosed area under the cyclic voltammogram of the composite shows a higher capacitance.

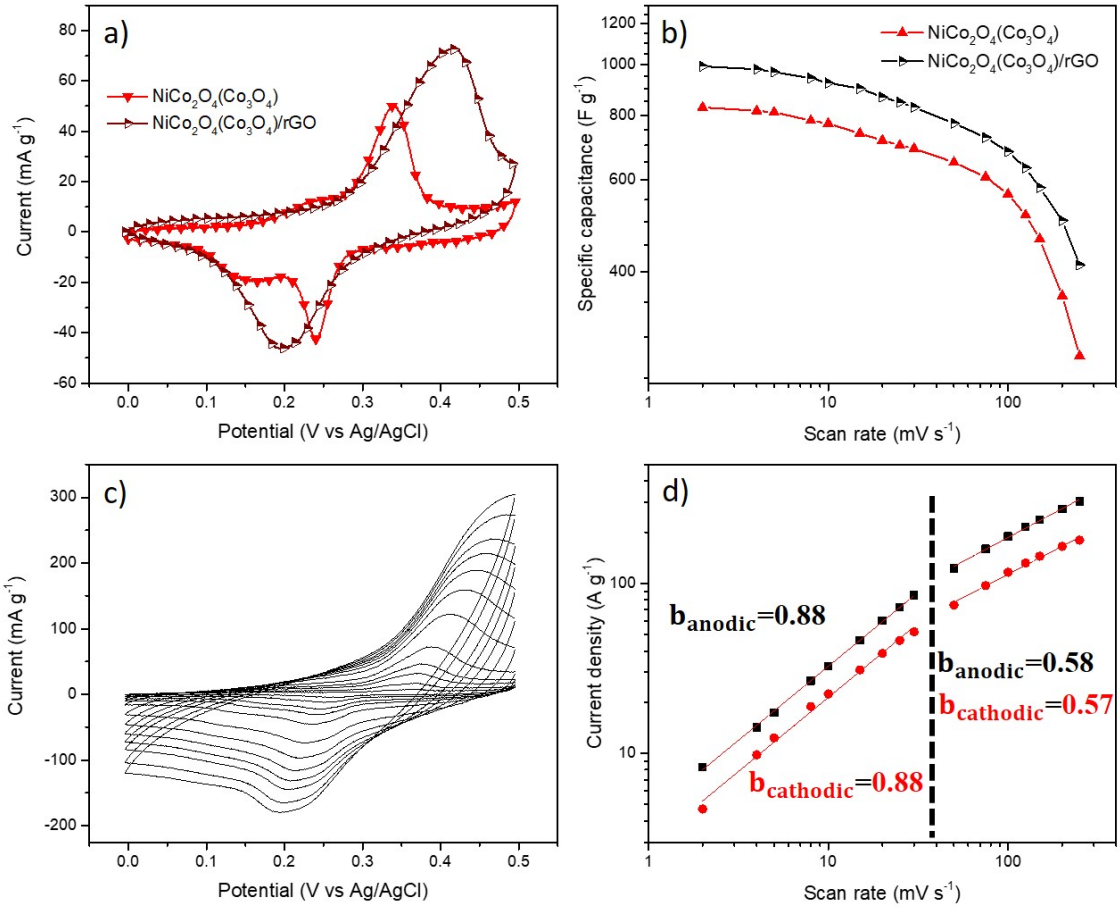

Figure 5.5.) Cyclic voltammograms at a scan rate of 25 mV s^{-1}, and b) Specific capacitance at different scan rates and for $NiCo_2O_4(Co_3O_4)$/rGO and $NiCo_2O_4(Co_3O_4)$, c) Cyclic voltammograms and, d) Voltammetric current dependence of peak currents to scan rates ranging from 2 to 250 mV s^{-1} for $NiCo_2O_4(Co_3O_4)$/rGO

The cyclic voltammograms were further collected at different scan rates (2 ~ 250 mV s^{-1}) shows superior capacitance of $NiCo_2O_4(Co_3O_4)$/rGO (20% more at 2 mV s^{-1} and 50% more at 250 mV s^{-1}) and was further examined to study the kinetics behavior of $NiCo_2O_4(Co_3O_4)$/rGO electrodes. The redox peaks shift to higher potentials (anodic peaks) and lower potentials (cathodic peaks) as the scan rate is increased, due to the polarization of the electrode surface at higher scan rates.

Furthermore, Figure 5.5.b shows the voltammetric current dependence of peak currents to scan rates and b value calculations for anodic and cathodic peaks revealed that although $NiCo_2O_4(Co_3O_4)$/rGO composite exhibits slightly faster redox reactions, by having greater anodic and cathodic b values (~0.88 for both) in comparison to the metal oxide (~0.85 for both) the general electrochemical kinetic characteristics of the composite is similar to the metal oxide as they both show the redox activity is diffusion-limited as the scan rate is increased to ≥ 50 mV s^{-1}. This could imply that the major contribution of the rGO scaffold is to prevent agglomeration and provide better accessibility of electrolyte ions to reach the surface of the metal oxides.

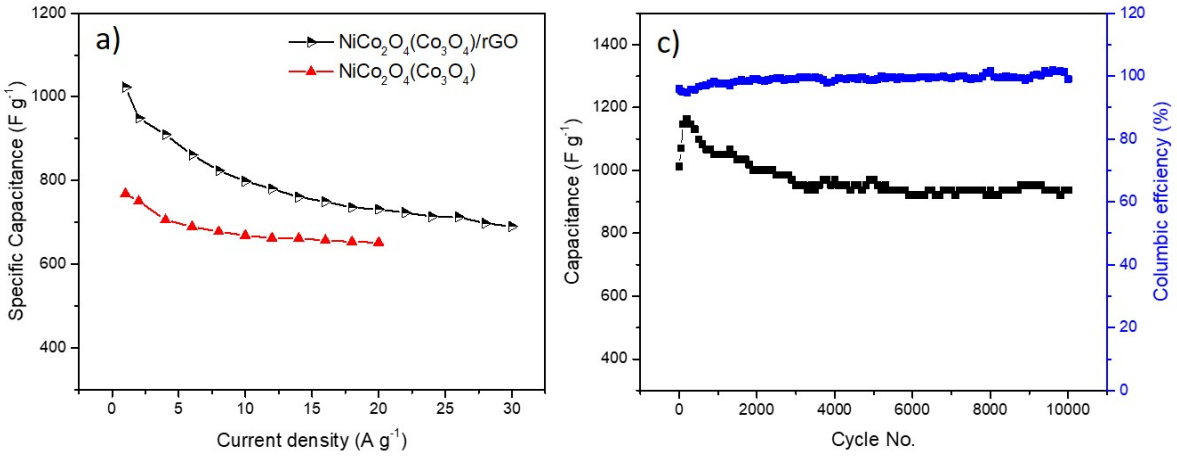

Figure 5.6. a) Normalized capacitance via Galvanostatic charge-discharge at different discharge rates of $NiCo_2O_4(Co_3O_4)$/rGO and $NiCo_2O_4(Co_3O_4)$ electrodes, b) Cyclic stability and columbic efficiency of the composite electrode at 10 A g^{-1} after 10k cycles

To understand better how our designed electrodes would perform for high-performance energy storage purposes, Galvanostatic Charge-Discharge (GCDC) tests were performed at different current densities and $NiCo_2O_4(Co_3O_4)$/rGO composite showed much improved performance, with a capacitance of 1023 F g^{-1} at 1 A g^{-1} (33% higher than in comparison to the metal oxide) and performed effectively at current densities as high as 30 A g^{-1} (50% higher

operatable current density in comparison to metal oxide electrode that could only reach 20 A g^{-1}) maintaining 67% of initial capacitance. This confirms the positive role of rGO sheets in preventing aggregation of metal oxide nanoparticles as well as enhancing charge transport properties. Additionally, the $NiCo_2O_4$(Co_3O_4)/rGO composite showed exceptional stability by maintaining 93% of the initial capacitance after 10k cycles at a charge/discharge rate of 10 A g^{-1}, while we previously reported 68% of capacitance retention at similar conditions for $NiCo_2O_4$(Co_3O_4) electrodes. It should also be noted that the composite electrode showed a columbic efficiency of almost 100% during the test that indicates the reversibility of the redox reactions during the charge/discharge process.

5.4 Conclusion

In this chapter, a straightforward composite assembly technique was investigated using a facile colloidal self-assembly technique. This methodology is expandable to form a composite structure of other spinel oxides as their surfaces could be easily functionalized using APTES. The $NiCo_2O_4$(Co_3O_4)/rGO in our research showed a 50% higher rate capability in comparison to our previously investigated $NiCo_2O_4$(Co_3O_4) nanocrystals, and it was able to maintain about 93% of the initial capacitance during the high-rate charge-discharge process (10 A g^{-1}). Although our methodology offers a solution to prevent the severe aggregation of metal oxide nanocrystals, it is important to investigate other assembly techniques to understand the role of composite structure on the kinetics and overall performance of the electrodes.

Chapter 6. Remaining Challenges and future outlook

Spinel oxides show promising characteristics with a robust crystalline structure and three-dimensional diffusion pathways. Although they offer high specific energy, it is important to improve their performance, in terms of capacitance, rate capability, and cycle stability, which needs to be further improved and a proper balance needs to be considered. It is very important to explore the extrinsic pseudocapacitive properties, and hybrid electrode formation of spinel oxides to tackle their intrinsic hindrances of charge transport and mass transport and be applicable for real-device applications.

Battery-like materials do not usually exhibit high rate behavior as they undergo crystallographic phase transformations during electrochemical cycling with a wide voltage hysteresis between the charge and discharge steps. To bring out extrinsic pseudocapacitance properties of these materials it is vital to increase the surface area through nanostructuring as it shortens the ion-diffusion pathways and in some cases, it might suppress the phase transformation. Among battery-like spinel oxides, nickel cobaltite shows great promise since it maintains high capacitance even at high discharge rates, as discussed extensively in previous chapters. The battery-type behavior is due to the formation of oxyhydroxides as shown below:

$$M_3O_2 + OH^- + H_2O \leftrightarrow 3MOOH + e^- \quad (44) \quad (M= Co, Ni)$$

While for cobalt, the electrochemically formed oxyhydroxide participates in a second reversible redox reaction

$$CoOOH + H^+ + e^- \leftrightarrow MO_2 \quad (45)$$

Thus, the electrochemical signature of these materials combines pseudocapacitive (eqn (45)) and battery-type (eqn (44)) contributions.[41,52,191]

Based on the earlier discussion, nickel cobaltite exhibits both capacitive and battery-type behavior due to the phase changes in the cycling process, and the nanoscale preparation is expected to shift its electrochemical characteristics toward pseudocapacitive behavior. little research has been carried out to study their kinetics but it is expected by exploiting design strategies that produce structures with very high surface areas and sophisticated electrode architectures whose function it is to expose as much of the material's surface to the electrolyte as possible, the pseudocapacitive behavior becomes more apparent. Besides, to move forward towards device applications, it is important to set material/electrode metrics for this type of high-energy density materials as it can be misleading when low weight loadings or thin films are used and charge-discharge experiments are carried out over tens of minutes.

In order to find the truth about nickel cobaltite hybrid structures and investigate the feasibility of exploiting them in next-generation high-performance energy storage devices, the following subjects need to be further studied:

i) In-situ characterization experiments conducted by Raman spectroscopy, XRD, or Electron microscopy need to be conducted to further understand the phase transition of metal oxide structure during charge-discharge process for this type of sophisticated electrodes.

ii) Investigating the dual role of Ni in the charge storage process. as it was discussed nickel shows battery-type behavior by forming an oxyhydroxide, while it acts as a dopant in Co_3O_4 crystal structure and improves the conductivity and charge-transport properties.

iii) The hybrid structure formation has a great effect on the final electrochemical performance and different metal oxide/graphene orientations need to be studied in more detail The understanding and controlling of metal oxide-carbon structure interfaces in mesostructured hybrid materials can be a game changer in terms of improving the charge-transport properties and rate capability of nickel cobaltite hybrid structures even at high mass loading of electrodes.

Appendix: Summary table of methods and control factors

Chapter 3: Electrophoretic deposition of NCO/PANI/rGO hybrid structure

In this study, we focused on optimizing the deposition mass ratio of the composite electrode by tuning the compounds' mass ratio in EPD suspension. The deposition time, deposition potential, and suspension concentrations were kept constant. Due to the semi-stable nature of EPD suspension, it is important to use suspension concentrations in the range of 2-3 mg mL^{-1}as exceeding above this region will not be stable (sedimentation of particles will take place too fast). The electrophoretic deposition potential of 30 V would give us homogenous deposited films with no detectable cracks or mechanical faults. Electrophoretic deposition time was kept between 15-20 seconds to form thin films with a thickness ranging from 1.2 to 2 μm. Fabricating films with higher thickness results in low mechanical stability of the films after thermal treatment and a much increased ohmic resistance in the electrode during electrochemical characterization.

Below, a list of different composite electrodes prepared using different compounds mass ratios in EPD suspension and their respective calculated capacitance during the GCDC process at 1 A g^{-1} is presented.

Sample	NCO:PANI:rGO ratio	Deposition mass (mg cm^{-3})	Specific capacitance(1 A g^{-1}) F g^{-1}
NCO/PANI/rGO 1	10:1:1	0.7	1830
NCO/PANI/rGO 2	5:1:1	0.5	1321
NCO/PANI/rGO 3	20:1:1	0.7	1010
NCO/PANI 1	10:1:0	0.7	964
NCO/PANI 2	5:1:0	0.6	1083
NCO/PANI 3	20:1:0	0.6	930
NCO/rGO 1	10:0:1	0.5	1212
NCO/rGO 2	5:0:1	0.6	1410
NCO/rGO 3	20:0:1	0.6	1081

Table A1. Composite electrodes with different mass ratios using EPD and their respective specific capacitance

Based on the suggested mass ratios of metal oxide and conductive compounds in the literature, and the electrochemical performance findings presented above, we decided to pursue an ideal 10:1:1 ratio as the final deposition mass ratio.

Chapter 4: MOF-based $NiCo_2O_4/Co_3O_4$ porous metal oxides

In this chapter, we controlled the metal oxide composite microstructure by tuning the sacrificial template. Our goal was to control the template properties by firstly controlling the starting MOF crystal size by modulating ligand (ML) and secondly forming nickel-containing double layered hydroxide (LDH) on the MOF surface by etching.

Initially, MOF structures with different size and structure were prepared using different Metal:Ligand: Modulating ligand ratios as presented below:

Metal: Ligand: Modulating ligand (Molar ratio)
1:4:0
1:16:0
1:4:4
1:16:16

Table A2. Synthesized ZIF-67 samples

ZIF-67	SSA (m^2g^{-1})	Pore volume (cc g^{-1})	Avg. Pore size (nm)
1:4:0	1296.498	0.031	3.30
1:16:0	1457.095	0.038	3.30
1:4:4	1346.501	0.464	12.63
1:16:16	1333.656	0. 628	7.95

Table A3. Structural characteristics of MOF templates from N_2 adsorption/desorption isotherms

Based on the structural properties of the MOF structures, 1:16:16 ZIF-67 nanocrystal was chosen due to its higher pore volume (in comparison to MOF microcrystals) and narrower pore size distribution (in comparison to 1:4:4 ZIF-67 nanocrystal presented in Figure 4.6.b). For a comparative study of crystal size effect on final electrochemical performance, 1:16:0 ZIF-67 microcrystals were used.

In the second step, MOF crystals were etched at different etchant concentrations and later calcinated to synthesize $NiCo_2O_4/Co_3O_4$ porous metal oxides. As-prepared samples are presented below.

ZIF-67	Etching concentration (mg mL^{-1} Ni^{2+})	ZIF-67/LDH	Sample code
1:16:16	1.2	1:16:16-30	1:16:16-30 MO
1:16:16	2.4	1:16:16-60	1:16:16-60 MO
1:16:16	3.6	1:16:16-90	1:16:16-90 MO
1:16:0	2.4	1:16:0-60	1:16:0-60MO

Table A4. List of studied MOF/LDH and metal oxide samples derived from ZIF-67 templates for electrochemical studies

Metal Oxide	SSA (m^2g^{-1})	Pore volume (cc g^{-1})	Avg. Pore size (nm)
1:16:16-30 MO	65.757	0.226	9.49
1:16:16-60 MO	88.757	0.253	12.04
1:16:16-90 MO	77.45	0.243	9.40
1:16:0-60 MO	84.67	0.210	3.20

Table A5. Structural characteristics of Co_3O_4 /$NiCo_2O_4$ from N_2 adsorption/desorption isotherms

Metal oxide nanostructures with efficient etching during MOF/LDH formation would give us the highest pore volume and specific surface area (SSA).

We further studied the electrochemical performance of our metal oxides by considering the effect of size and etching concentration, as two separate control factors. The 1:16:16-60 MO electrode showed the best performance due to nano-sized crystals (vs. 1:16:0-60 MO presented in Figure 4.15) and due to desirable pore structure coming from optimal etching treatment (Figure 4.9 and 4.12).

Chapter 5: Self-assembly of $NiCo_2O_4$/Co_3O_4 composite structures

Through this chapter, the composite assembly process was systematically optimized by changing the mass ratio of functionalized $NiCo_2O_4/Co_3O_4$ and GO in the dispersion. The table below shows the procedure to select the favorable mass ratio.

Sample	Mass ratio (MO:GO)	Observation
$NiCo_2O_4/Co_3O_4$-rGO 1	1:2	The prepared sample showed a two-phase composition under Raman microscope consisting of a composite phase and an rGO phase showing excess unreacted rGO
$NiCo_2O_4/Co_3O_4$-rGO 2	1:4	Only composite phase was detected under Raman microscope
$NiCo_2O_4/Co_3O_4$-rGO 3	1:8	No graphene peak was detectable after chemical reduction

Table A6. List of self-assembled composite structures prepared for structural characterization using Raman spectroscopy

The figure presented below shows how graphene peaks intensity changes at two different MO: GO mass ratios.

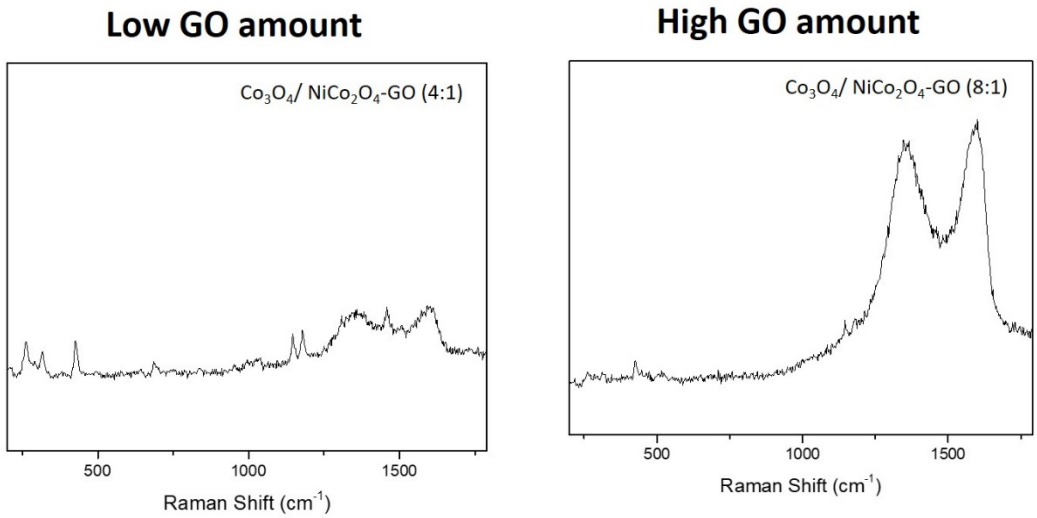

Figure A1. A comparison of Raman spectra for composite structures consisting using different GO amount

As a final comparison, a Ragone plot comparing the specific energy and specific power of final the electrodes prepared at chapters 3,4, and 5 are presented below . Starting from the random backbone structure of $NiCo_2O_4$/PANI/rGO electrophoretic deposition electrode (blue triangle, Chapter 3), we improved the oxide component functionality by designing MOF-derived oxide composite (red circle, Chapter 4) still utilizing $NiCo_2O_4$ redox cycles at the electrode surface. Finally, we improved the electrode once more by dispersing the newly developed MOF-derived oxide composite crystals on the rGO support through simple electrostatic force-based self-assembly (green star, Chapter 5).

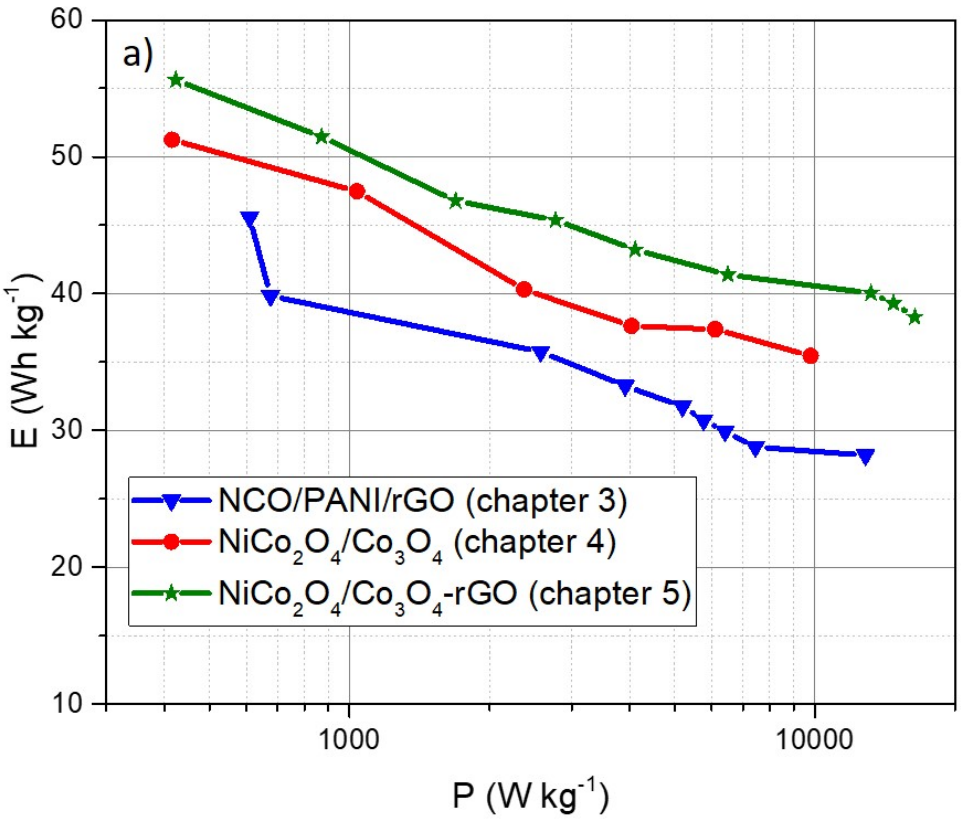

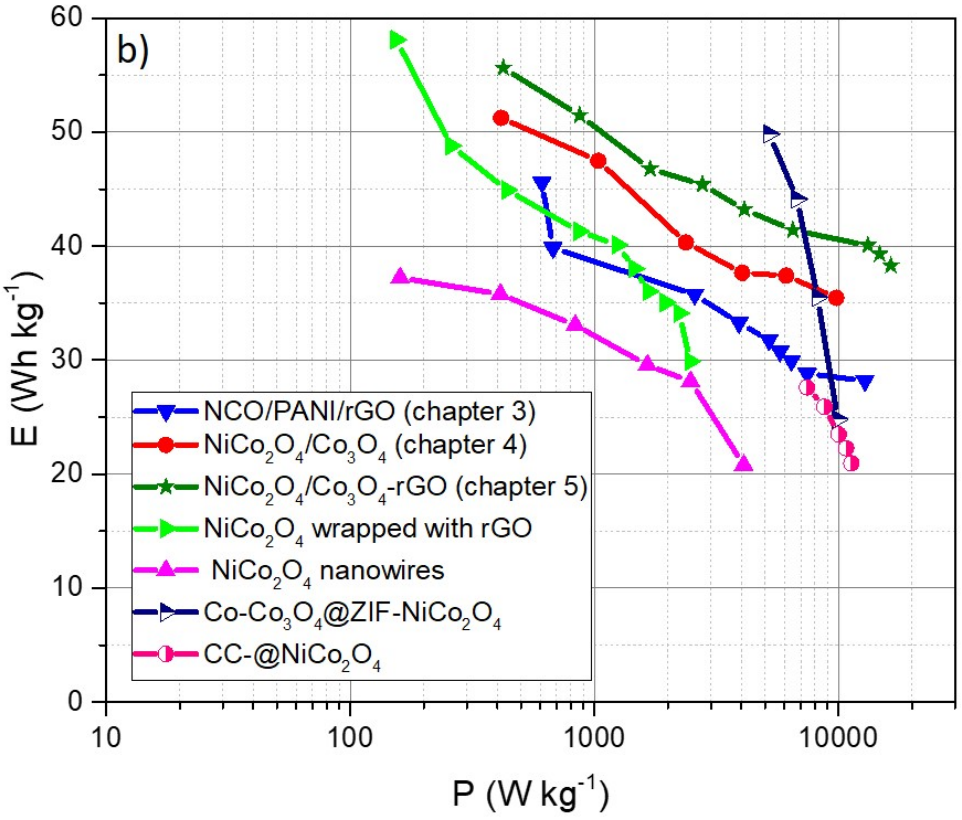

Figure A2. Ragone plots showcasing the specific energy and specific power of a) different electrodes fabricated throughout our studies and b) comparison with similar literature

References

(1) Yang, Z.; Zhang, J.; Kintner-Meyer, M. C. W.; Lu, X.; Choi, D.; Lemmon, J. P.; Liu, J. Electrochemical Energy Storage for Green Grid. *Chem. Rev.* **2011**, *111* (5), 3577–3613.

(2) Kim, H.; Hong, J.; Park, K.-Y.; Kim, H.; Kim, S.-W.; Kang, K. Aqueous Rechargeable Li and Na Ion Batteries. *Chem. Rev.* **2014**, *114* (23), 11788–11827.

(3) Pike Research. **2010**, *2015*.

(4) Merlet, C.; Rotenberg, B.; Madden, P. A.; Taberna, P. L.; Simon, P.; Gogotsi, Y.; Salanne, M. On the Molecular Origin of Supercapacitance in Nanoporous Carbon Electrodes. *Nat. Mater.* **2012**, *11* (4), 306–310.

(5) Simon, P.; Gogotsi, Y. Materials for Electrochemical Capacitors. *Nature Materials*. Nature Publishing Group November 16, 2008, pp 845–854.

(6) Ragone, D. Review of Battery Systems for Electrically Powered Vehicles. **1968**.

(7) Hall, P. J.; Mirzaeian, M.; Fletcher, S. I.; Sillars, F. B.; Rennie, A. J. R.; Shitta-Bey, G. O.; Wilson, G.; Cruden, A.; Carter, R. Energy Storage in Electrochemical Capacitors: Designing Functional Materials to Improve Performance. *Energy Environ. Sci.* **2010**, *3* (9), 1238–1251.

(8) Conway, B. E. Transition from "supercapacitor" to "Battery" Behavior in Electrochemical Energy Storage. In *Proceedings of the International Power Sources Symposium*; Publ by IEEE, 1991; Vol. 138, pp 319–327.

(9) Conway, B. *Electrochemical Supercapacitors: Scientific Fundamentals and Technological Applications*; Kluwer Academic/Plenum Press: New York, 2013.

(10) Raymundo-Piñero, E.; Kierzek, K.; Machnikowski, J.; Béguin, F. Relationship between the Nanoporous Texture of Activated Carbons and Their Capacitance Properties in Different Electrolytes. *Carbon N. Y.* **2006**, *44* (12), 2498–2507.

(11) Senokos, E.; Reguero, V.; Palma, J.; Vilatela, J. J.; Marcilla, R. Macroscopic Fibres of CNTs as Electrodes for Multifunctional Electric Double Layer Capacitors: From Quantum Capacitance to Device Performance. *Nanoscale* **2016**, *8* (6), 3620–3628.

(12) Yang, X.; Cheng, C.; Wang, Y.; Qiu, L.; Li, D. Liquid-Mediated Dense Integration of Graphene Materials for Compact Capacitive Energy Storage. *Science (80-.).* **2013**, *341* (6145), 534–537.

(13) Chmiola, J.; Yushin, G.; Gogotsi, Y.; Portet, C.; Simon, P.; Taberna, P. L. Anomalous Increase in Carbon Capacitance at Pore Sizes Less than 1 Nanometer. *Science (80-.).* **2006**, *313* (5794), 1760–1763.

(14) Ji, H.; Zhao, X.; Qiao, Z.; Jung, J.; Zhu, Y.; Lu, Y.; Zhang, L. L.; MacDonald, A. H.; Ruoff, R. S. Capacitance of Carbon-Based Electrical Double-Layer Capacitors. *Nat. Commun.* **2014**, *5* (1), 1–7.

(15) Engelsmann, K.; Lorenz, W. J.; Schmidt, E. Underpotential Deposition of Lead on Polycrystalline and Single-Crystal Gold Surfaces. Part I. Thermodynamics. *J. Electroanal. Chem.* **1980**, *114* (1), 1–10.

(16) Conway, B. E. Two-Dimensional and Quasi-Two-Dimensional Isotherms for Li Intercalation and Upd Processes at Surfaces. *Electrochim. Acta* **1993**, *38* (9), 1249–1258.

(17) Yang, M. H.; Jeong, J. M.; Huh, Y. S.; Choi, B. G. High-Performance Supercapacitor Based on Three-Dimensional MoS2/Graphene Aerogel Composites. *Compos. Sci. Technol.* **2015**, *121*, 123–128.

(18) Zeng, H. M.; Zhao, Y.; Hao, Y. J.; Lai, Q. Y.; Huang, J. H.; Ji, X. Y. Preparation and Capacitive Properties of Sheet V6O13 for Electrochemical Supercapacitor. *J. Alloys Compd.* **2009**, *477* (1–2), 800–804.

(19) Lukatskaya, M. R.; Mashtalir, O.; Ren, C. E.; Dall'Agnese, Y.; Rozier, P.; Taberna, P. L.; Naguib, M.; Simon, P.; Barsoum, M. W.; Gogotsi, Y. Cation Intercalation and High Volumetric Capacitance of Two-Dimensional Titanium Carbide. *Science.* **2013**, *341* (6153), 1502–1505.

(20) Winter, M.; Brodd, R. J. What Are Batteries, Fuel Cells, and Supercapacitors? *Chem. Rev.* **2004**, *104* (10), 4245–4270.

(21) Zhu, Y.; Murali, S.; Stoller, M. D.; Ganesh, K. J.; Cai, W.; Ferreira, P. J.; Pirkle, A.; Wallace, R. M.; Cychosz, K. A.; Thommes, M.; Su, D.; Stach, E. A.; Ruoff, R. S. Carbon-Based Supercapacitors Produced by Activation of Graphene. *Science.* **2011**, *332* (6037), 1537–1541.

(22) Toupin, M.; Brousse, T.; Bélanger, D. Charge Storage Mechanism of MnO_2 Electrode Used in Aqueous Electrochemical Capacitor. *Chem. Mater.* **2004**, *16* (16), 3184–3190.

(23) Blanc, F.; Leskes, M.; Grey, C. P. *In Situ* Solid-State NMR Spectroscopy of Electrochemical Cells: Batteries, Supercapacitors, and Fuel Cells. *Acc. Chem. Res.* **2013**, *46* (9), 1952–1963.

(24) Yang, Y.; Huang, J.; Zeng, J.; Xiong, J.; Zhao, J. Direct Electrophoretic Deposition of Binder-Free Co_3O_4 /Graphene Sandwich-Like Hybrid Electrode as Remarkable Lithium Ion Battery Anode. *ACS Appl. Mater. Interfaces* **2017**, *9* (38), 32801–32811.

(25) Angerstein-Kozlowska, H.; Electroanalytical, B. C.-J. of; 1979, U. Evaluation of Rate Constants and Reversibility Parameters for Surface Reactions by the Potential-Sweep Method. *J. Electroanal. Chem.* **1979**, *95* (1), 1–28.

(26) Sugimoto, W.; Iwata, H.; Yokoshima, K.; Murakami, Y.; Takasu, Y. Proton and Electron Conductivity in Hydrous Ruthenium Oxides Evaluated by Electrochemical Impedance Spectroscopy: The Origin of Large Capacitance. *J. Phys. Chem. B* **2005**, *109* (15), 7330–7338.

(27) Chuanyun Wan , Liyang Yuan, H. S. Effects of Electrode Mass-Loading on the Electrochemical Properties of Porous MnO2 for Electrochemical Supercapacitor. *Int. J. Electrochem. Sci.* **2014**, No. 9, 4024–4038.

(28) Wang, Y.-G.; Li, H.-Q.; Xia, Y.-Y. Ordered Whiskerlike Polyaniline Grown on the Surface of Mesoporous Carbon and Its Electrochemical Capacitance Performance. *Adv. Mater.* **2006**, *18* (19), 2619–2623.

(29) Ghidiu, M.; Lukatskaya, M. R.; Zhao, M. Q.; Gogotsi, Y.; Barsoum, M. W. Conductive Two-Dimensional Titanium Carbide 'clay'with High Volumetric Capacitance. *Nature* **2015**, *516* (7529), 78–81.

(30) Wang, J.; Polleux, J.; Lim, J.; Dunn, B. Pseudocapacitive Contributions to Electrochemical Energy Storage in TiO 2 (Anatase) Nanoparticles. *J. Phys. Chem. C* **2007**, *111* (40), 14925–14931.

(31) Come, J.; Taberna, P.-L.; Hamelet, S.; Masquelier, C.; Simon, P. Electrochemical Kinetic Study of LiFePO4 Using Cavity Microelectrode. *J. Electrochem. Soc.* **2011**, *158* (10), A1090.

(32) Liu, J.; Wang, J.; Xu, C.; Jiang, H.; Li, C.; Zhang, L.; Lin, J.; Shen, Z. X. Advanced Energy Storage Devices: Basic Principles, Analytical Methods, and Rational Materials Design. *Adv. Sci.* **2018**, *5* (1), 1700322.

(33) Liu, T. -C.; Pell, W. G.; Conway, B. E.; Roberson, S. L. Behavior of Molybdenum Nitrides as Materials for Electrochemical Capacitors Comparison with Ruthenium Oxide. *J. Electrochem. Soc.* **1998**, *145* (6), 1882–1888.

(34) MacArthur, D. M. The Proton Diffusion Coefficient for the Nickel Hydroxide Electrode. *J. Electrochem. Soc.* **1970**, *117* (6), 729.

(35) Ardizzone, S.; Fregonara, G.; Trasatti, S. "Inner" and "Outer" Active Surface of RuO2 Electrodes. *Electrochim. Acta* **1990**, *35* (1), 263–267.

(36) Liu, C.; Gillette, E. I.; Chen, X.; Pearse, A. J.; Kozen, A. C.; Schroeder, M. A.; Gregorczyk, K. E.; Lee, S. B.; Rubloff, G. W. An All-in-One Nanopore Battery Array. *Nat. Nanotechnol.* **2014**, *9* (12), 1031–1039.

(37) Yan, W.; Kim, J. Y.; Xing, W.; Donavan, K. C.; Ayvazian, T.; Penner, R. M. Lithographically Patterned Gold/Manganese Dioxide Core/Shell Nanowires for High Capacity, High Rate, and High Cyclability Hybrid Electrical Energy Storage. *Chem. Mater.* **2012**, *24* (12), 2382–2390.

(38) Bard, A.; Faulkner, L.; Leddy, J.; Zoski, C. *Electrochemical Methods: Fundamentals and Applications*, 2nd ed.; Wiley, 1980.

(39) Nilson, R. H.; Brumbach, M. T.; Bunker, B. C. Modeling the Electrochemical Impedance Spectra of Electroactive Pseudocapacitor Materials. *J. Electrochem. Soc.* **2011**, *158* (6), A678.

(40) Ogoshi, T.; Yoshikoshi, K.; Sueto, R.; Nishihara, H.; Yamagishi, T. Porous Carbon Fibers Containing Pores with Sizes Controlled at the Ångstrom Level by the Cavity Size of Pillar[6]Arene. *Angew. Chemie Int. Ed.* **2015**, *54* (22), 6466–6469.

(41) Wang, Y.; Song, Y.; Xia, Y. Electrochemical Capacitors: Mechanism, Materials, Systems, Characterization and Applications. *Chem. Soc. Rev.* **2016**, *45* (21), 5925–5950.

(42) Zhou, H.; Zhu, S.; Hibino, M.; Honma, I. Electrochemical Capacitance of Self-Ordered Mesoporous Carbon. *J. Power Sources* **2003**, *122* (2), 219–223.

(43) Liu, H.-J.; Wang, J.; Wang, C.-X.; Xia, Y.-Y. Ordered Hierarchical Mesoporous/Microporous Carbon Derived from Mesoporous Titanium-Carbide/Carbon Composites and Its Electrochemical Performance in Supercapacitor. *Adv. Energy Mater.* **2011**, *1* (6), 1101–1108.

(44) Xia, J.; Chen, F.; Li, J.; Tao, N. Measurement of the Quantum Capacitance of Graphene. *Nat. Nanotechnol.* **2009**, *4* (8), 505–509.

(45) Zhu, Y.; Murali, S.; Cai, W.; Li, X.; Suk, J. W.; Potts, J. R.; Ruoff, R. S. Graphene and Graphene Oxide: Synthesis, Properties, and Applications. *Adv. Mater.* **2010**, *22* (35), 3906–3924.

(46) Liu, C.; Yu, Z.; Neff, D.; Zhamu, A.; Jang, B. Z. Graphene-Based Supercapacitor with an Ultrahigh Energy Density. *Nano Lett.* **2010**, *10* (12), 4863–4868.

(47) Xu, Y.; Lin, Z.; Zhong, X.; Huang, X.; Weiss, N. O.; Huang, Y.; Duan, X. Holey Graphene Frameworks for Highly Efficient Capacitive Energy Storage. *Nat. Commun.* **2014**, *5* (1), 1–8.

(48) Kulkarni, S. B.; Patil, U. M.; Shackery, I.; Sohn, J. S.; Lee, S.; Park, B.; Jun, S. High-Performance Supercapacitor Electrode Based on a Polyaniline Nanofibers/3D Graphene Framework as an Efficient Charge Transporter. *J. Mater. Chem. A* **2014**, *2* (14), 4989–4998.

(49) Trasatti, S.; Buzzanca, G. Ruthenium Dioxide: A New Interesting Electrode Material. Solid State Structure and Electrochemical Behaviour. *J. Electroanal. Chem.* **1971**, *29* (2), A1–A5.

(50) Brousse, T.; Toupin, M.; Dugas, R.; Athouël, L.; Crosnier, O.; Bélanger, D. Crystalline MnO2 as Possible Alternatives to Amorphous Compounds in Electrochemical Supercapacitors. *J. Electrochem. Soc.* **2006**, *153* (12), A2171.

(51) Zheng, J. P.; Cygan, P. J.; Jow, T. R.; Jow', T. R.; Cygan, P. J.; Jow, T. R. Hydrous Ruthenium Oxide as an Electrode Material for Electrochemical Capacitors. *J. Electrochem. Soc.* **1995**, *142* (8), 2699–2703.

(52) Augustyn, V.; Simon, P.; Dunn, B. Pseudocapacitive Oxide Materials for High-Rate Electrochemical Energy Storage. *Energy Environ. Sci.* **2014**, *7* (5), 1597–1614.

(53) Shi, Y.; Peng, L.; Ding, Y.; Zhao, Y.; Yu, G. Nanostructured Conductive Polymers for Advanced Energy Storage. *Chem. Soc. Rev.* **2015**, *44* (19), 6684–6696.

(54) Sathiya, M.; Prakash, A. S.; Ramesha, K.; Tarascon, J.; Shukla, A. K. V_2O_5-Anchored Carbon Nanotubes for Enhanced Electrochemical Energy Storage. *J. Am. Chem. Soc.* **2011**, *133* (40), 16291–16299.

(55) Brezesinski, T.; Wang, J.; Senter, R.; Brezesinski, K.; Dunn, B.; Tolbert, S. H. On the Correlation between Mechanical Flexibility, Nanoscale Structure, and Charge Storage in Periodic Mesoporous CeO_2 Thin Films. *ACS Nano* **2010**, *4* (2), 967–977.

(56) Okubo, M.; Hosono, E.; Kim, J.; Enomoto, M.; Kojima, N.; Kudo, T.; Zhou, H.; Honma, I. Nanosize Effect on High-Rate Li-Ion Intercalation in LiCoO 2 Electrode. *J. Am. Chem. Soc.* **2007**, *129* (23), 7444–7452.

(57) Lee, J. W.; Hall, A. S.; Kim, J.-D.; Mallouk, T. E. A Facile and Template-Free Hydrothermal Synthesis of Mn 3 O 4 Nanorods on Graphene Sheets for Supercapacitor Electrodes with Long Cycle Stability. *Chem. Mater.* **2012**, *24* (6), 1158–1164.

(58) Wang, S.-Y.; Ho, K.-C.; Kuo, S.-L.; Wu, N.-L. Investigation on Capacitance Mechanisms of Fe3O4 Electrochemical Capacitors. *J. Electrochem. Soc.* **2006**, *153* (1), A75–A80.

(59) Xia, X. H.; Tu, J. P.; Wang, X. L.; Gu, C. D.; Zhao, X. B. Mesoporous Co3O4 Monolayer Hollow-Sphere Array as Electrochemical Pseudocapacitor Material. *Chem. Commun.* **2011**, *47* (20), 5786–5788.

(60) Kuo, S.; sources, N. W.-J. of power; 2006, undefined. Electrochemical Characterization on MnFe2O4/Carbon Black Composite Aqueous Supercapacitors. *Elsevier*.

(61) Yu, L.; Zhang, G.; Yuan, C.; Lou, X. W. Hierarchical NiCo 2 O 4@ MnO 2 Core–Shell Heterostructured Nanowire Arrays on Ni Foam as High-Performance Supercapacitor Electrodes. *Chem. Commun.* **2013**, *49* (2), 137–139.

(62) Yeager, M. P.; Du, W.; Wang, Q.; Deskins, N. A.; Sullivan, M.; Bishop, B.; Su, D.; Xu, W.; Senanayake, S. D.; Si, R.; Hanson, J.; Teng, X. Pseudocapacitive Hausmannite Nanoparticles with (101) Facets: Synthesis, Characterization, and Charge-Transfer Mechanism. *ChemSusChem* **2013**, *6* (10), 1983–1992.

(63) Yuan, C.; Li, J.; Hou, L.; Lin, J.; Pang, G.; Zhang, L.; Lian, L.; Zhang, X. Template-Engaged Synthesis of Uniform Mesoporous Hollow NiCo 2 O 4 Sub-Microspheres towards High-Performance Electrochemical Capacitors. *RSC Adv.* **2013**, *3* (40), 18573–18578.

(64) Hu, L.; Wu, L.; Liao, M.; Hu, X.; Fang, X. Electrical Transport Properties of Large, Individual NiCo2O4 Nanoplates. *Adv. Funct. Mater.* **2012**, *22* (5), 998–1004.

(65) Li, Y.; Hasin, P.; Wu, Y. NixCo3−xO4 Nanowire Arrays for Electrocatalytic Oxygen Evolution. *Adv. Mater.* **2010**, *22* (17), 1926–1929.

(66) Dubal, D. P.; Gomez-Romero, P.; Sankapal, B. R.; Holze, R. Nickel Cobaltite as an Emerging Material for Supercapacitors: An Overview. *Nano Energy* **2015**, *11*, 377–399.

(67) Wu, Z. S.; Zhou, G.; Yin, L. C.; Ren, W.; Li, F.; Cheng, H. M. Graphene/Metal Oxide Composite Electrode Materials for Energy Storage. *Nano Energy*. 2012, pp 107–131.

(68) Wang, H.; Robinson, J. T.; Diankov, G.; Dai, H. Nanocrystal Growth on Graphene with Various Degrees of Oxidation. *J. Am. Chem. Soc.* **2010**, *132* (10), 3270–3271.

(69) Wu, Z.-S.; Ren, W.; Wen, L.; Gao, L.; Zhao, J.; Chen, Z.; Zhou, G.; Li, F.; Cheng, H.-M. Graphene Anchored with Co 3 O 4 Nanoparticles as Anode of Lithium Ion Batteries with Enhanced Reversible Capacity and Cyclic Performance. *ACS Nano* **2010**, *4* (6), 3187–3194.

(70) Zhou, G.; Wang, D.-W.; Li, F.; Zhang, L.; Li, N.; Wu, Z.-S.; Wen, L.; Lu, G. Q. (Max); Cheng, H.-M. Graphene-Wrapped Fe 3 O 4 Anode Material with Improved Reversible Capacity and Cyclic Stability for Lithium Ion Batteries. *Chem. Mater.* **2010**, *22* (18), 5306–5313.

(71) Yang, S.; Feng, X.; Ivanovici, S.; Müllen, K. Fabrication of Graphene-Encapsulated Oxide Nanoparticles: Towards High-Performance Anode Materials for Lithium Storage. *Angew. Chemie Int. Ed.* **2010**, *49* (45), 8408–8411.

(72) Wang, Y.; Xia, Y. Recent Progress in Supercapacitors: From Materials Design to System Construction. *Adv. Mater.* **2013**, *25* (37), 5336–5342.

(73) Brousse, T.; Toupin, M.; Dugas, R.; Athouël, L.; Crosnier, O.; Bélanger, D. Crystalline MnO 2 as Possible Alternatives to Amorphous Compounds in Electrochemical Supercapacitors. *J. Electrochem. Soc.* **2006**, *153* (12), A2171.

(74) Zheng, J. P.; Jow', T. R.; Cygan, P. J. Hydrous Ruthenium Oxide as an Electrode Material for Electrochemical Capacitors. *J. Electrochem. Soc.* **1995**, *142* (8), 2699–2703.

(75) Augustyn, V.; Come, J.; Lowe, M. A.; Woung Kim, J.; Taberna, P.-L.; Tolbert, S. H.; Abruña, H. D.; Simon, P.; Dunn, B.; High, al. High-Rate Electrochemical Energy Storage through Li+ Intercalation Pseudocapacitance. *Nat. Mater.* **2013**, *12* (6).

(76) Wang, H.; Gao, Q.; Jiang, L. Facile Approach to Prepare Nickel Cobaltite Nanowire Materials for Supercapacitors. *Small* **2011**, *7* (17), 2454–2459.

(77) Chen, H.; Jiang, J.; Zhang, L.; Wan, H.; Qi, T.; Xia, D. Highly Conductive NiCo2S4 Urchin-like Nanostructures for High-Rate Pseudocapacitors. *Nanoscale* **2013**, *5* (19), 8879–8883.

(78) Wang, H.-W.; Hu, Z.-A.; Chang, Y.-Q.; Chen, Y.-L.; Wu, H.-Y.; Zhang, Z.-Y.; Yang, Y.-Y. Design and Synthesis of NiCo2O4–Reduced Graphene Oxide Composites for High Performance Supercapacitors. *J. Mater. Chem.* **2011**, *21* (28), 10504.

(79) Xia, X. H.; Tu, J. P.; Wang, X. L.; Gu, C. D.; Zhao, X. B. Mesoporous Co3O4 Monolayer Hollow-Sphere Array as Electrochemical Pseudocapacitor Material. *Chem. Commun.* **2011**, *47* (20), 5786–5788.

(80) Padmanathan, N.; Selladurai, S. Mesoporous MnCo2O4 Spinel Oxide Nanostructure Synthesized by Solvothermal Technique for Supercapacitor. *Ionics (Kiel).* **2014**, *20* (4), 479–487.

(81) Dubal, D. P.; Gomez-Romero, P.; Sankapal, B. R.; Holze, R. Nickel Cobaltite as an Emerging Material for Supercapacitors: An Overview. *Nano Energy* **2015**, *11* (1), 377–399.

(82) Liu, X.; Shi, S.; Xiong, Q.; Li, L.; Zhang, Y.; Tang, H.; Gu, C.; Wang, X.; Tu, J. Hierarchical NiCo2O4@NiCo2O4 Core/Shell Nanoflake Arrays as High-Performance Supercapacitor Materials. *ACS Appl. Mater. Interfaces* **2013**, *5* (17), 8790–8795.

(83) Zhu, Y.; Wu, Z.; Jing, M.; Hou, H.; Yang, Y.; Zhang, Y.; Yang, X.; Song, W.; Jia, X.; Ji, X. Porous NiCo2O4 Spheres Tuned through Carbon Quantum Dots Utilised as Advanced

Materials for an Asymmetric Supercapacitor. *J. Mater. Chem. A* **2015**, *3* (2), 866–877.

(84) Li, X.; Sun, W.; Wang, L.; Qi, Y.; Guo, T.; Zhao, X.; Yan, X. Three-Dimensional Hierarchical Self-Supported NiCo 2 O 4 /Carbon Nanotube Core-Shell Networks as High Performance Supercapacitor Electrodes. *RSC Adv.* **2015**, *5* (11), 7976–7985.

(85) Huang, L.; Chen, D.; Ding, Y.; Feng, S.; Wang, Z. L.; Liu, M. Nickel-Cobalt Hydroxide Nanosheets Coated on NiCo2O4 Nanowires Grown on Carbon Fiber Paper for High-Performance Pseudocapacitors. *Nano Lett.* **2013**, *13* (7), 3135–3139.

(86) Chien, H. C.; Cheng, W. Y.; Wang, Y. H.; Lu, S. Y. Ultrahigh Specific Capacitances for Supercapacitors Achieved by Nickel Cobaltite/Carbon Aerogel Composites. *Adv. Funct. Mater.* **2012**, *22* (23), 5038–5043.

(87) Li, Q.; Lu, C.; Chen, C.; Xie, L.; Liu, Y.; Li, Y.; Kong, Q.; Wang, H. Layered NiCo2O4/Reduced Graphene Oxide Composite as an Advanced Electrode for Supercapacitor. *Energy Storage Mater.* **2017**, *8*, 59–67.

(88) Ma, L.; Shen, X.; Zhou, H.; Ji, Z.; Chen, K.; Zhu, G. High Performance Supercapacitor Electrode Materials Based on Porous NiCo2O4 Hexagonal Nanoplates/Reduced Graphene Oxide Composites. *Chem. Eng. J.* **2015**, *262*, 980–988.

(89) *Electrophoretic Deposition of Nanomaterials*; Dickerson, J. H., Boccaccini, A. R., Eds.; Nanostructure Science and Technology; Springer New York: New York, NY, 2012.

(90) Yang, Y.; Li, J.; Chen, D.; Zhao, J. A Facile Electrophoretic Deposition Route to the Fe $_3$ O $_4$ /CNTs/RGO Composite Electrode as a Binder-Free Anode for Lithium Ion Battery. *ACS Appl. Mater. Interfaces* **2016**, *8* (40), 26730–26739.

(91) Besra, L.; Liu, M. A Review on Fundamentals and Applications of Electrophoretic Deposition (EPD). *Progress in Materials Science*. 2007, pp 1–61.

(92) Diba, M.; Fam, D. W. H.; Boccaccini, A. R.; Shaffer, M. S. P. Electrophoretic Deposition of Graphene-Related Materials: A Review of the Fundamentals. *Progress in Materials Science*. 2016, pp 83–117.

(93) Chi, B.; Li, J.; Yang, X.; Lin, H.; Wang, N. Electrophoretic Deposition of ZnCo2O4 Spinel and Its Electrocatalytic Properties for Oxygen Evolution Reaction. *Electrochim. Acta* **2005**, *50* (10), 2059–2064.

(94) Kanamura, K.; Goto, A.; Rho, Y. H.; Umegaki, T. Electrophoretic Fabrication of LiCoO2 Positive Electrodes for Rechargeable Lithium Batteries. In *Journal of Power Sources*; Elsevier, 2001; Vol. 97–98, pp 294–297.

(95) Moore, J. J.; Kang, J. H.; Wen, J. Z. Fabrication and Characterization of Single Walled Nanotube Supercapacitor Electrodes with Uniform Pores Using Electrophoretic Deposition. *Mater. Chem. Phys.* **2012**, *134* (1), 68–73.

(96) Aghazadeh, M.; Ganjali, M. R. Samarium-Doped Fe3O4 Nanoparticles with Improved Magnetic and Supercapacitive Performance: A Novel Preparation Strategy and Characterization. *J. Mater. Sci.* **2018**, *53* (1), 295–308.

(97) Bree, G.; Geaney, H.; Ryan, K. M. Electrophoretic Deposition of Tin Sulfide Nanocubes as High-Performance Lithium-Ion Battery Anodes. *ChemElectroChem* **2019**, *6* (12), 3049–3056.

(98) Das, D.; Mitra, A.; Jena, S.; Majumder, S. B.; Basu, R. N. Electrophoretically Deposited ZnFe2O4-Carbon Black Porous Film as a Superior Negative Electrode for Lithium-Ion Battery. *ACS Sustain. Chem. Eng.* **2018**, *6* (12), 17000–17010.

(99) Yang, C. C.; Hsu, S. T.; Chien, W. C. All Solid-State Electric Double-Layer Capacitors Based on Alkaline Polyvinyl Alcohol Polymer Electrolytes. *J. Power Sources* **2005**, *152* (1–2), 303–310.

(100) Zhong, J. H.; Wang, A. L.; Li, G. R.; Wang, J. W.; Ou, Y. N.; Tong, Y. X. Co 3O 4/Ni(OH) 2 Composite Mesoporous Nanosheet Networks as a Promising Electrode for Supercapacitor Applications. *J. Mater. Chem.* **2012**, *22* (12), 5656–5665.

(101) Liu, Z. Q.; Xiao, K.; Xu, Q. Z.; Li, N.; Su, Y. Z.; Wang, H. J.; Chen, S. Fabrication of Hierarchical Flower-like Super-Structures Consisting of Porous NiCo<inf>2</Inf>O<inf>4</Inf> Nanosheets and Their Electrochemical and Magnetic Properties. *RSC Adv.* **2013**, *3* (13), 4372–4380.

(102) Marco, J. F.; Gancedo, J. R.; Gracia, M.; Gautier, J. L.; Ríos, E.; Berry, F. J. Characterization of the Nickel Cobaltite, NiCo2O4, Prepared by Several Methods: An XRD, XANES, EXAFS, and XPS Study. *J. Solid State Chem.* **2000**, *153* (1), 74–81.

(103) Roginskaya, Y. E.; Morozova, O. V.; Lubnin, E. N.; Ulitina, Y. E.; Lopukhova, G. V.; Trasatti, S. Characterization of Bulk and Surface Composition of $Co_x Ni_{1-x} O_y$ Mixed Oxides for Electrocatalysis. *Langmuir* **1997**, *13* (17), 4621–4627.

(104) Jiménez, V. M.; Fernández, A.; Espinós, J. P.; González-Elipe, A. R. The State of the Oxygen at the Surface of Polycrystalline Cobalt Oxide. *J. Electron Spectros. Relat. Phenomena* **1995**, *71* (1), 61–71.

(105) Stobinski, L.; Lesiak, B.; Malolepszy, A.; Mazurkiewicz, M.; Mierzwa, B.; Zemek, J.; Jiricek, P.; Bieloshapka, I. Graphene Oxide and Reduced Graphene Oxide Studied by the XRD, TEM and Electron Spectroscopy Methods. *J. Electron Spectros. Relat. Phenomena* **2014**, *195*, 145–154.

(106) Ji, Z.; Zhu, G.; Shen, X.; Zhou, H.; Wu, C.; Wang, M. Reduced Graphene Oxide Supported FePt Alloy Nanoparticles with High Electrocatalytic Performance for Methanol Oxidation. *New J. Chem.* **2012**, *36* (9), 1774.

(107) Thomsen, C.; Reich, S. Double Resonant Raman Scattering in Graphite. *Phys. Rev. Lett.* **2000**, *85* (24), 5214–5217.

(108) Stankovich, S.; Dikin, D. A.; Piner, R. D.; Kohlhaas, K. A.; Kleinhammes, A.; Jia, Y.; Wu, Y.; Nguyen, S. B. T.; Ruoff, R. S. Synthesis of Graphene-Based Nanosheets via Chemical Reduction of Exfoliated Graphite Oxide. *Carbon N. Y.* **2007**, *45* (7), 1558–1565.

(109) Liu, J.; Lin, Z.; Liu, T.; Yin, Z.; Zhou, X.; Chen, S.; Xie, L.; Boey, F.; Zhang, H.; Huang, W. Multilayer Stacked Low-Temperature-Reduced Graphene Oxide Films: Preparation, Characterization, and Application in Polymer Memory Devices. *Small* **2010**, *6* (14), 1536–

1542.

(110) Zhang, L. The Electrocatalytic Oxidation of Ascorbic Acid on Polyaniline Film Synthesized in the Presence of β-Naphthalenesulfonic Acid. *Electrochim. Acta* **2007**, *52* (24), 6969–6975.

(111) Li, G.-R.; Feng, Z.-P.; Zhong, J.-H.; Wang, Z.-L.; Tong, Y.-X. Electrochemical Synthesis of Polyaniline Nanobelts with Predominant Electrochemical Performances. *Macromolecules* **2010**, *43* (5), 2178–2183.

(112) Rozlívková, Z.; Trchová, M.; Exnerová, M.; Stejskal, J. The Carbonization of Granular Polyaniline to Produce Nitrogen-Containing Carbon. *Synth. Met.* **2011**, *161* (11–12), 1122–1129.

(113) Mažeikiene, R.; Tomkute, V.; Kuodis, Z.; Niaura, G.; Malinauskas, A. Raman Spectroelectrochemical Study of Polyaniline and Sulfonated Polyaniline in Solutions of Different PH. *Vib. Spectrosc.* **2007**, *44* (2), 201–208.

(114) Mažeikienė, R.; Niaura, G.; Malinauskas, A. Raman Spectroelectrochemical Study of Polyaniline at UV, Blue, and Green Laser Line Excitation in Solutions of Different PH. *Synth. Met.* **2018**, *243*, 97–106.

(115) Su, Y.; Zhitomirsky, I. Cataphoretic Assembly of Cationic Dyes and Deposition of Carbon Nanotube and Graphene Films. *J. Colloid Interface Sci.* **2013**, *399*, 46–53.

(116) Peng, H.; Ma, G.; Sun, K.; Mu, J.; Zhou, X.; Lei, Z. A Novel Fabrication of Nitrogen-Containing Carbon Nanospheres with High Rate Capability as Electrode Materials for Supercapacitors. *RSC Adv.* **2015**, *5* (16), 12034–12042.

(117) Liu, H.; Xu, B.; Jia, M.; Zhang, M.; Cao, B.; Zhao, X.; Wang, Y. Polyaniline Nanofiber/Large Mesoporous Carbon Composites as Electrode Materials for Supercapacitors. *Appl. Surf. Sci.* **2015**, *332*, 40–46.

(118) Xu, B.; Zheng, D.; Jia, M.; Cao, G.; Yang, Y. Nitrogen-Doped Porous Carbon Simply Prepared by Pyrolyzing a Nitrogen-Containing Organic Salt for Supercapacitors. *Electrochim. Acta* **2013**, *98*, 176–182.

(119) Hulicova-Jurcakova, D.; Seredych, M.; Lu, G. Q.; Bandosz, T. J. Combined Effect of Nitrogen- and Oxygen-Containing Functional Groups of Microporous Activated Carbon on Its Electrochemical Performance in Supercapacitors. *Adv. Funct. Mater.* **2009**, *19* (3), 438–447.

(120) Yang, J.; Yu, C.; Liang, S.; Li, S.; Huang, H.; Han, X.; Zhao, C.; Song, X.; Hao, C.; Ajayan, P. M.; Qiu, J. Bridging of Ultrathin $NiCo_2O_4$ Nanosheets and Graphene with Polyaniline: A Theoretical and Experimental Study. *Chem. Mater.* **2016**, *28* (16), 5855–5863.

(121) Feng, J.-X.; Ding, L.-X.; Ye, S.-H.; He, X.-J.; Xu, H.; Tong, Y.-X.; Li, G.-R. $Co(OH)_2$@PANI Hybrid Nanosheets with 3D Networks as High-Performance Electrocatalysts for Hydrogen Evolution Reaction. *Adv. Mater.* **2015**, *27* (44), 7051–7057.

(122) Qing, X.; Liu, S.; Huang, K.; Lv, K.; Yang, Y.; Lu, Z.; Fang, D.; Liang, X. Facile

Synthesis of Co3O4 Nanoflowers Grown on Ni Foam with Superior Electrochemical Performance. *Electrochim. Acta* **2011**, *56* (14), 4985–4991.

(123) Li, Y.; Tan, B.; Wu, Y. Freestanding Mesoporous Quasi-Single-Crystalline Co3O 4 Nanowire Arrays. *J. Am. Chem. Soc.* **2006**, *128* (44), 14258–14259.

(124) Zhou, K.; Zhou, W.; Liu, X.; Sang, Y.; Ji, S.; Li, W.; Lu, J.; Li, L.; Niu, W.; Liu, H.; Chen, S. Ultrathin MoO3 Nanocrystalsself-Assembled on Graphene Nanosheets via Oxygen Bonding as Supercapacitor Electrodes of High Capacitance and Long Cycle Life. *Nano Energy* **2015**, *12*, 510–520.

(125) Wang, X.; Yan, C.; Sumboja, A.; Lee, P. S. High Performance Porous Nickel Cobalt Oxide Nanowires for Asymmetric Supercapacitor. *Nano Energy* **2014**, *3*, 119–126.

(126) Tang, C.; Tang, Z.; Gong, H. Hierarchically Porous Ni-Co Oxide for High Reversibility Asymmetric Full-Cell Supercapacitors. *J. Electrochem. Soc.* **2012**, *159* (5).

(127) Yedluri, A. K.; Kim, H. J. Enhanced Electrochemical Performance of Nanoplate Nickel Cobaltite (NiCo 2 O 4) Supercapacitor Applications. *RSC Adv.* **2019**, *9* (2), 1115–1122.

(128) Aricò, A. S.; Bruce, P.; Scrosati, B.; Tarascon, J. M.; Van Schalkwijk, W. Nanostructured Materials for Advanced Energy Conversion and Storage Devices. *Nature Materials*. Nature Publishing Group May 2005, pp 366–377.

(129) Whittingham, M. S. Materials Challenges Facing Electrical Energy Storage. *MRS Bull.* **2008**, *33* (4), 411–419.

(130) Zhang, Q.; Uchaker, E.; Candelaria, S. L.; Cao, G. Nanomaterials for Energy Conversion and Storage. *Chem. Soc. Rev.* **2013**, *42* (7), 3127–3171.

(131) Simon, P.; Gogotsi, Y. Perspectives for Electrochemical Capacitors and Related Devices. *Nature Materials*. Nature Research August 3, 2020, pp 1–13.

(132) He, X.; Li, R.; Liu, J.; Liu, Q.; chen, R. R.; Song, D.; Wang, J. Hierarchical FeCo2O4@NiCo Layered Double Hydroxide Core/Shell Nanowires for High Performance Flexible All-Solid-State Asymmetric Supercapacitors. *Chem. Eng. J.* **2018**, *334*, 1573–1583.

(133) Lin, J.; Liang, H.; Jia, H.; Chen, S.; Cai, Y.; Qi, J.; Cao, J.; Fei, W.; Feng, J. Hierarchical CuCo2O4@NiMoO4 Core-Shell Hybrid Arrays as a Battery-like Electrode for Supercapacitors. *Inorg. Chem. Front.* **2017**, *4* (9), 1575–1581.

(134) Meher, S. K.; Rao, G. R. Ultralayered Co3O4 for High-Performance Supercapacitor Applications. *J. Phys. Chem. C* **2011**, *115* (31), 15646–15654.

(135) Rashti, A.; Wang, B.; Hassani, E.; Feyzbar-Khalkhali-Nejad, F.; Zhang, X.; Oh, T.-S. Electrophoretic Deposition of Nickel Cobaltite/Polyaniline/RGO Composite Electrode for High-Performance All-Solid-State Asymmetric Supercapacitors. *Energy & Fuels* **2020**, *34* (5), 6448–6461.

(136) Zhu, K.; Wang, Q.; Kim, J. H.; Pesaran, A. A.; Frank, A. J. Pseudocapacitive Lithium-Ion Storage in Oriented Anatase TiO 2 Nanotube Arrays. *J. Phys. Chem. C* **2012**, *116* (22),

11895–11899.

(137) Okubo, M.; Hosono, E.; Kim, J.; Enomoto, M.; Kojima, N.; Kudo, T.; Zhou, H.; Honma, I. Nanosize Effect on High-Rate Li-Ion Intercalation in LiCoO2 Electrode. *J. Am. Chem. Soc.* **2007**, *129* (23), 7444–7452.

(138) Hasegawa, S.; Horike, S.; Matsuda, R.; Furukawa, S.; Mochizuki, K.; Kinoshita, Y.; Kitagawa, S. Three-Dimensional Porous Coordination Polymer Functionalized with Amide Groups Based on Tridentate Ligand: Selective Sorption and Catalysis. *J. Am. Chem. Soc.* **2007**, *129* (9), 2607–2614.

(139) Eddaoudi, M.; Kim, J.; Rosi, N.; Vodak, D.; Wachter, J.; O'Keeffe, M.; Yaghi, O. M. Systematic Design of Pore Size and Functionality in Isoreticular MOFs and Their Application in Methane Storage. *Science (80-.).* **2002**, *295* (5554), 469–472.

(140) Furukawa, H.; Cordova, K. E.; O'Keeffe, M.; Yaghi, O. M. The Chemistry and Applications of Metal-Organic Frameworks. *Science*. American Association for the Advancement of Science August 30, 2013.

(141) Halter, D. P.; Klein, R. A.; Boreen, M. A.; Trump, B. A.; Brown, C. M.; Long, J. R. Self-Adjusting Binding Pockets Enhance H2and CH4adsorption in a Uranium-Based Metal-Organic Framework. *Chem. Sci.* **2020**, *11* (26), 6709–6716.

(142) Lee, J.; Farha, O. K.; Roberts, J.; Scheidt, K. A.; Nguyen, S. T.; Hupp, J. T. Metal-Organic Framework Materials as Catalysts. *Chem. Soc. Rev.* **2009**, *38* (5), 1450–1459.

(143) Ahmed, A.; Seth, S.; Purewal, J.; Wong-Foy, A. G.; Veenstra, M.; Matzger, A. J.; Siegel, D. J. Exceptional Hydrogen Storage Achieved by Screening Nearly Half a Million Metal-Organic Frameworks. *Nat. Commun.* **2019**, *10* (1), 1–9.

(144) Kornienko, N.; Zhao, Y.; Kley, C. S.; Zhu, C.; Kim, D.; Lin, S.; Chang, C. J.; Yaghi, O. M.; Yang, P. Metal-Organic Frameworks for Electrocatalytic Reduction of Carbon Dioxide. *J. Am. Chem. Soc.* **2015**, *137* (44), 14129–14135.

(145) Salunkhe, R. R.; Kaneti, Y. V.; Kim, J.; Kim, J. H.; Yamauchi, Y. Nanoarchitectures for Metal-Organic Framework-Derived Nanoporous Carbons toward Supercapacitor Applications. *Acc. Chem. Res.* **2016**, *49* (12), 2796–2806.

(146) Li, Y.; Xu, Y.; Yang, W.; Shen, W.; Xue, H.; Pang, H. MOF-Derived Metal Oxide Composites for Advanced Electrochemical Energy Storage. *Small* **2018**, *14* (25), 1704435.

(147) Liu, Y.; Xu, X.; Shao, Z.; Jiang, S. P. Metal-Organic Frameworks Derived Porous Carbon, Metal Oxides and Metal Sulfides-Based Compounds for Supercapacitors Application. *Energy Storage Mater.* **2020**, *26*, 1–22.

(148) Lu, G.; Li, S.; Guo, Z.; Farha, O. K.; Hauser, B. G.; Qi, X.; Wang, Y.; Wang, X.; Han, S.; Liu, X.; Duchene, J. S.; Zhang, H.; Zhang, Q.; Chen, X.; Ma, J.; Loo, S. C. J.; Wei, W. D.; Yang, Y.; Hupp, J. T.; Huo, F. Imparting Functionality to a Metal-Organic Framework Material by Controlled Nanoparticle Encapsulation. *Nat. Chem.* **2012**, *4* (4), 310–316.

(149) Park, K. S.; Ni, Z.; Côté, A. P.; Choi, J. Y.; Huang, R.; Uribe-Romo, F. J.; Chae, H. K.; O'Keeffe, M.; Yaghi, O. M. Exceptional Chemical and Thermal Stability of Zeolitic

Imidazolate Frameworks. *Proc. Natl. Acad. Sci. U. S. A.* **2006**, *103* (27), 10186–10191.

(150) Forgan, R. S. Modulated Self-Assembly of Metal-Organic Frameworks. *Chemical Science*. Royal Society of Chemistry May 14, 2020, pp 4546–4562.

(151) Marshall, C. R.; Staudhammer, S. A.; Brozek, C. K. Size Control over Metal-Organic Framework Porous Nanocrystals. *Chemical Science*. Royal Society of Chemistry October 24, 2019, pp 9396–9408.

(152) Park, J.; Wang, Z. U.; Sun, L. B.; Chen, Y. P.; Zhou, H. C. Introduction of Functionalized Mesopores to Metal-Organic Frameworks via Metal-Ligand-Fragment Coassembly. *J. Am. Chem. Soc.* **2012**, *134* (49), 20110–20116.

(153) Shearer, G. C.; Chavan, S.; Bordiga, S.; Svelle, S.; Olsbye, U.; Lillerud, K. P. Defect Engineering: Tuning the Porosity and Composition of the Metal-Organic Framework UiO-66 via Modulated Synthesis. *Chem. Mater.* **2016**, *28* (11), 3749–3761.

(154) Cravillon, J.; Nayuk, R.; Springer, S.; Feldhoff, A.; Huber, K.; Wiebcke, M. Controlling Zeolitic Imidazolate Framework Nano- and Microcrystal Formation: Insight into Crystal Growth by Time-Resolved in Situ Static Light Scattering. *Chem. Mater.* **2011**, *23* (8), 2130–2141.

(155) McGuire, C. V.; Forgan, R. S. The Surface Chemistry of Metal-Organic Frameworks. *Chem. Commun.* **2015**, *51* (25), 5199–5217.

(156) Guo, H.; Zhu, Y.; Wang, S.; Su, S.; Zhou, L.; Zhang, H. Combining Coordination Modulation with Acid-Base Adjustment for the Control over Size of Metal-Organic Frameworks. *Chem. Mater.* **2012**, *24* (3), 444–450.

(157) Banerjee, R.; Phan, A.; Wang, B.; Knobler, C.; Furukawa, H.; O'Keeffe, M.; Yaghi, O. M. High-Throughput Synthesis of Zeolitic Imidazolate Frameworks and Application to CO2 Capture. *Science (80-.).* **2008**, *319* (5865), 939–943.

(158) Zsigmondy, R.; Scherrer, P. Bestimmung Der Inneren Struktur Und Der Größe von Kolloidteilchen Mittels Röntgenstrahlen. In *Kolloidchemie Ein Lehrbuch*; Springer Berlin Heidelberg, 1912; pp 387–409.

(159) Kruk, M.; Jaroniec, M. Gas Adsorption Characterization of Ordered Organic-Inorganic Nanocomposite Materials. *Chemistry of Materials*. American Chemical Society 2001, pp 3169–3183.

(160) Barrett, E. P.; Joyner, L. G.; Halenda, P. P. The Determination of Pore Volume and Area Distributions in Porous Substances. I. Computations from Nitrogen Isotherms. *J. Am. Chem. Soc.* **1951**, *73* (1), 373–380.

(161) Hu, H.; Guan, B.; Xia, B.; Lou, X. W. Designed Formation of Co3O4/NiCo2O4 Double-Shelled Nanocages with Enhanced Pseudocapacitive and Electrocatalytic Properties. *J. Am. Chem. Soc.* **2015**, *137* (16), 5590–5595.

(162) Fan, G.; Li, F.; Evans, D. G.; Duan, X. Catalytic Applications of Layered Double Hydroxides: Recent Advances and Perspectives. *Chemical Society Reviews*. Royal Society of Chemistry October 21, 2014, pp 7040–7066.

(163) Jiang, Z.; Li, Z.; Qin, Z.; Sun, H.; Jiao, X.; Chen, D. LDH Nanocages Synthesized with MOF Templates and Their High Performance as Supercapacitors. *Nanoscale* **2013**, *5* (23), 11770–11775.

(164) Wang, J. *Analytical Electrochemistry*; John Wiley & Sons, 2006.

(165) Savéant, J.-M. *Elements of Molecular and Biomolecular Electrochemistry*; John Wiley & Sons, Inc.: Hoboken, NJ, USA, 2006.

(166) Baronetto, D.; Krstajić, N.; Trasatti, S. Reply to "Note on a Method to Interrelate Inner and Outer Electrode Areas" by H. Vogt. *Electrochim. Acta* **1994**, *39* (16), 2359–2362.

(167) Ardizzone, S.; Fregonara, G.; Trasatti, S. "Inner" and "Outer" Active Surface of RuO2 Electrodes. *Electrochim. Acta* **1990**, *35* (1), 263–267.

(168) Chen, Z.; Augustyn, V.; Jia, X.; Xiao, Q.; Dunn, B.; Lu, Y. High-Performance Sodium-Ion Pseudocapacitors Based on Hierarchically Porous Nanowire Composites. *ACS Nano* **2012**, *6* (5), 4319–4327.

(169) Yu, L.; Zhang, L.; Wu, H. Bin; Lou, X. W. D. Formation of Ni x Co 3− x S 4 Hollow Nanoprisms with Enhanced Pseudocapacitive Properties . *Angew. Chemie* **2014**, *126* (14), 3785–3788.

(170) Wu, X.; Han, Z.; Zheng, X.; Yao, S.; Yang, X.; Zhai, T. Core-Shell Structured Co3O4@NiCo2O4 Electrodes Grown on Flexible Carbon Fibers with Superior Electrochemical Properties. *Nano Energy* **2017**, *31*, 410–417.

(171) Salunkhe, R. R.; Tang, J.; Kamachi, Y.; Nakato, T.; Kim, J. H.; Yamauchi, Y. Asymmetric Supercapacitors Using 3D Nanoporous Carbon and Cobalt Oxide Electrodes Synthesized from a Single Metal-Organic Framework. *ACS Nano* **2015**, *9* (6), 6288–6296.

(172) Guan, C.; Liu, X.; Ren, W.; Li, X.; Cheng, C.; Wang, J. Rational Design of Metal-Organic Framework Derived Hollow NiCo2O4 Arrays for Flexible Supercapacitor and Electrocatalysis. *Adv. Energy Mater.* **2017**, *7* (12).

(173) Yu, D.; Wu, B.; Ge, L.; Wu, L.; Wang, H.; Xu, T. Decorating Nanoporous ZIF-67-Derived NiCo2O4 Shells on a Co3O4 Nanowire Array Core for Battery-Type Electrodes with Enhanced Energy Storage Performance. *J. Mater. Chem. A* **2016**, *4* (28), 10878–10884.

(174) Jayakumar, A.; Antony, R. P.; Wang, R.; Lee, J. M. MOF-Derived Hollow Cage NixCo3−xO4 and Their Synergy with Graphene for Outstanding Supercapacitors. *Small* **2017**, *13* (11).

(175) Lu, X.; Zhai, T.; Zhang, X.; Shen, Y.; Yuan, L.; Hu, B.; Gong, L.; Chen, J.; Gao, Y.; Zhou, J.; Tong, Y.; Wang, Z. L. WO 3-X@Au@MnO 2 Core-Shell Nanowires on Carbon Fabric for High-Performance Flexible Supercapacitors. *Adv. Mater.* **2012**, *24* (7), 938–944.

(176) Wang, B.; Chen, J. S.; Wang, Z.; Madhavi, S.; Lou, X. W. Green Synthesis of Nio Nanobelts with Exceptional Pseudo-Capacitive Properties. *Adv. Energy Mater.* **2012**, *2* (10), 1188–1192.

(177) Saravanakumar, B.; Purushothaman, K. K.; Muralidharan, G. Interconnected V 2O 5 Nanoporous Network for High-Performance Supercapacitors. *ACS Appl. Mater. Interfaces* **2012**, *4* (9), 4484–4490.

(178) Jiang, J.; Li, Y.; Liu, J.; Huang, X.; Yuan, C.; Lou, X. W. Recent Advances in Metal Oxide-Based Electrode Architecture Design for Electrochemical Energy Storage. *Advanced Materials*. John Wiley & Sons, Ltd October 2, 2012, pp 5166–5180.

(179) Yuan, C.; Wu, H. Bin; Xie, Y.; Lou, X. W. Mixed Transition-Metal Oxides: Design, Synthesis, and Energy-Related Applications. *Angewandte Chemie - International Edition*. John Wiley & Sons, Ltd February 3, 2014, pp 1488–1504.

(180) Chaikittisilp, W.; Hu, M.; Wang, H.; Huang, H. S.; Fujita, T.; Wu, K. C. W.; Chen, L. C.; Yamauchi, Y.; Ariga, K. Nanoporous Carbons through Direct Carbonization of a Zeolitic Imidazolate Framework for Supercapacitor Electrodes. *Chem. Commun.* **2012**, *48* (58), 7259–7261.

(181) Hu, J.; Wang, H.; Gao, Q.; Guo, H. Porous Carbons Prepared by Using Metal-Organic Framework as the Precursor for Supercapacitors. *Carbon N. Y.* **2010**, *48* (12), 3599–3606.

(182) Akhbari, K.; Morsali, A. Silver Nanofibers from the Nanorods of One-Dimensional Organometallic Coordination Polymers. *CrystEngComm* **2010**, *12* (11), 3394–3396.

(183) Ma, T. Y.; Dai, S.; Jaroniec, M.; Qiao, S. Z. Metal-Organic Framework Derived Hybrid Co3O4-Carbon Porous Nanowire Arrays as Reversible Oxygen Evolution Electrodes. *J. Am. Chem. Soc.* **2014**, *136* (39), 13925–13931.

(184) Jung, S.; Cho, W.; Lee, H. J.; Oh, M. Self-Template-Directed Formation of Coordination-Polymer Hexagonal Tubes and Rings, and Their Calcination to ZnO Rings. *Angew. Chemie* **2009**, *121* (8), 1487–1490.

(185) Stavila, V.; Whitmire, K. H.; Rusakova, I. Synthesis of Bi2S3 Nanostructures from Bismuth(III) Thiourea and Thiosemicarbazide Complexes. *Chem. Mater.* **2009**, *21* (22), 5456–5465.

(186) Abouali, S.; Akbari Garakani, M.; Xu, Z. L.; Kim, J. K. NiCo2O4/CNT Nanocomposites as Bi-Functional Electrodes for Li Ion Batteries and Supercapacitors. *Carbon N. Y.* **2016**, *102*, 262–272.

(187) Wu, P.; Cheng, S.; Yao, M.; Yang, L.; Zhu, Y.; Liu, P.; Xing, O.; Zhou, J.; Wang, M.; Luo, H.; Liu, M. A Low-Cost, Self-Standing NiCo2O4@CNT/CNT Multilayer Electrode for Flexible Asymmetric Solid-State Supercapacitors. *Adv. Funct. Mater.* **2017**, *27* (34), 1702160.

(188) Sathish, M.; Mitani, S.; Tomai, T.; Honma, I. MnO2 Assisted Oxidative Polymerization of Aniline on Graphene Sheets: Superior Nanocomposite Electrodes for Electrochemical Supercapacitors. *J. Mater. Chem.* **2011**, *21* (40), 16216–16222.

(189) Liu, Y.; Li, Y.; Li, X. M.; He, T. Kinetics of (3-Aminopropyl)Triethoxylsilane (Aptes) Silanization of Superparamagnetic Iron Oxide Nanoparticles. *Langmuir* **2013**, *29* (49), 15275–15282.

(190) Park, S.; An, J.; Potts, J. R.; Velamakanni, A.; Murali, S.; Ruoff, R. S. Hydrazine-Reduction of Graphite- and Graphene Oxide. *Carbon N. Y.* **2011**, *49* (9), 3019–3023.

(191) Brousse, T.; Bélanger, D.; Long, J. W. To Be or Not To Be Pseudocapacitive? *J. Electrochem. Soc.* **2015**, *162* (5), A5185–A5189.